UNIVERSITÀ DELLA CALABRIA

UNIVERSITA' DELLA CALABRIA

Dipartimento di Biologia, Ecologia e Scienze della Terra

Scuola di Dottorato

"ARCHIMEDE" in Scienze, Comunicazione e Tecnologie

Indirizzo

Scienze della Terra

Con il contributo di POR CALABRIA FSE 2007-2013

CICLO

XXVI

TITOLO TESI

Geochemical modeling of water-rock interaction in the ophiolitic aquifers of Northern Calabria

Settore Scientifico Disciplinare GEO/08

Direttore: Ch.mo Prof. Pietro Pantano

Supervisore: Ch.mo Dott. Carmine Apollaro

Co-tutors : Ch.mo Prof. Luigi Marini

Ch.ma Prof.ssa Rosanna De Rosa

Dottoranda: Dott.ssa Teresa Critelli

I dedicate my thesis to Luigi Marini,
an excellent and humble master
available to help
anyone who ask for it

Abstract

This study was developed in two distinct parts with the ultimate aim to investigate the weathering processes of the metabasalts and serpentinites of Northern Calabria, taking into account the dissolution kinetics of relevant mineral phases.

In the first part, a laboratory experimental work has been carried out on two suitably characterized rock samples, a metabasalt and a serpentinite, to determine the whole-rock dissolution rates and, consequently, the kinetic parameters of each constituting mineral in these specific rocks, at 25 °C and different pH values. Mixed-flow reactors were used to perform this experimental work. Incidentally, it must be recalled that: (i) although there are many laboratory studies aimed at the determination of the dissolution rates of separate (single) minerals, less is known about the dissolution rates of individual minerals in multimineralic rocks and (ii) in geochemical modeling, the dissolution rates measured on separate mineral are customarily utilized to estimate the dissolution path of the overall rock, assuming that the dissolution rate of a separate mineral is equal to that of the same mineral in a given rock. However, the experimental results of in this study contradict this hypothesis. Indeed, it turned out that: (i) dissolution rates of individual minerals obtained from the dissolution experiments of whole rocks are significantly different from those of separate minerals and (ii) the dissolution rates of individual minerals exhibit minor differences to each other and appear to be close to the whole-rock rate. This behavior is probably constrained by the sufficiently abundant mineral(s) of lowest dissolution rate, preventing the dissolution of other faster-dissolving mineral grains as long as these do not come in contact with the aqueous phase.

The second part of the study has been devoted to simulate the rock-to-water release of elements and their fate in the groundwaters interacting with metabasalts and serpentinites by means of two different reaction-path-modeling approaches. In the first approach, kinetic parameters of relevant minerals were taken from the geochemical literature and the progressive dissolution of metabasalts and serpentinites cropping out in Northern Calabria (Italy) was simulated by means of the EQ3/6 software package, version 8.0, adopting the Double Solid Reactant Method (DSRM). In the second approach, the whole-rock kinetic parameters, retrieved from the dissolution experiments on the metabasalt were used in the modeling exercise. The results of the two reaction-path-modeling approaches are in

agreement with analytical data for natural waters but the second approach appears to be more accurate than the first one.

The main lesson learned from this study is that the dissolution rates of individual minerals retrieved from the dissolution experiments of whole rocks are significantly different from those of separate minerals. This invalidate the assumption on the equality of these rates which is commonly adopted in geochemical modeling. These findings have important consequences on the understanding of the rock-to-water release of chemical elements and their fate in natural waters.

Abstract

Il presente studio è stato sviluppato in due parti distinte con il fine ultimo di investigare i processi di alterazione delle metabasiti e delle serpentiniti del settore settentrionale della Calabria, tenendo in considerazione le cinetiche di dissoluzione delle fasi minerali rilevanti.

Nella prima parte, è stato portato avanti un lavoro sperimentale di laboratorio su un campione di metabasite ed uno di serpentinite sufficientemente caratterizzati, per determinare le velocità di dissoluzione della roccia totale e, di conseguenza, i parametri cinetici di ciascun minerale costituente all'interno di tali rocce, a 25 °C e diversi valori di pH. Per realizzare questo lavoro sperimentale sono stati utilizzati i reattori a flusso continuo.

Fra l'altro, si deve ricordare che: (i) sebbene vi siano numerosi studi circa la determinazione delle velocità di dissoluzione dei singoli minerali, poco è noto circa le velocità di dissoluzione di ciascun minerale nelle rocce multi-mineraliche e (ii) nella modellizzazione geochimica, le velocità di dissoluzione misurate sul singolo minerale sono solitamente utilizzate per stimare il percorso di dissoluzione dell'intera roccia, assumendo che la velocità di dissoluzione del singolo minerale è uguale a quelli dello stesso minerale in una data roccia.

Tuttavia, i risultati sperimentali di questo studio contraddicono questa ipotesi. In effetti, è risultato che: (i) le velocità di dissoluzione dei minerali individuali ottenuti dagli esperimenti di dissoluzione su roccia totale sono significativamente diversi da quelli dei singoli minerali e (ii) le velocità di dissoluzione dei singoli minerali esibiscono differenze minori tra loro e sembrano essere più vicine alla velocità dell'intera roccia. Questo comportamento è probabilmente influenzato dal minerale (o dai minerali) sufficientemente abbondante con velocità di dissoluzione più bassa, che impedisce lo scioglimento degli altri grani minerali che si dissolvono più velocemente finché questi non entrano in contatto con la fase acquosa.

La seconda parte di questo studio è stata dedicata alla simulazione del rilascio roccia-acqua degli elementi ed al loro comportamento nelle acque che interagiscono con le metabasiti e le serpentiniti mediante due diversi approcci di modellizzazione del percorso di reazione. Nel primo approccio, sono stati utilizzati i parametri cinetici dalla letteratura geochimica

ed è stata simulata la dissoluzione progressiva delle metabasiti e delle serpentiniti affioranti nel settore settentrionale della Calabria (Italia) mediante l'uso del software EQ3/6 versione 8.0 ed adottando il Metodo del Doppio Reagente Solido (DSRM). Nel secondo approccio sono stati utilizzati i parametri cinetici della roccia totale per la modellizzazione, ottenuti dagli esperimenti di dissoluzione di una metabasite. I risultati dei due modelli del percorso di reazione sono in accordo con i dati analitici per le acque naturali ma il secondo approccio di modellizzazione si è rivelato più accurato del primo.

Il risultato principale ottenuto da questo studio è che le velocità di dissoluzione dei minerali individuali ottenuti dagli esperimenti di dissoluzione su roccia totale sono significativamente diversi da quelli dei singoli minerali. Questo annulla l'assunzione sull'uguaglianza di queste velocità che è comunemente adottata nella modellizzazione geochimica. Queste conclusioni hanno conseguenze importanti sull'interpretazione del rilascio roccia-acqua degli elementi chimici e sul loro comportamento nelle acque naturali.

Table of contents

Introduction

This doctoral thesis is aimed at investigating the weathering processes of the metabasalts and serpentinites cropping out in the study area through geochemical modeling and at determining the dissolution rate of each relevant mineral phase by means of laboratory dissolution experiments on two well characterized whole-rock samples, a metabasalt and a serpentinite.

Despite the large number of studies reporting the dissolution rates of individual minerals (see compilation of White and Brantley, 1995; Palandri and Kharaka, 2004; Marini, 2007; Bandstra *et al*., 2008 and references therein), less is known about the dissolution rates of whole rocks (e.g., Yokoyama and Banfield, 2002; Evans and Banwart, 2006; Gudbrandsson *et al*., 2011). This lack of data motivated the laboratory experiments which have been carried out to study on the dissolution kinetics of a metabasalt and a serpentinite cropping out in the area of interest in order to retrieve the rates of each constituting mineral phases and use these results to model water-rock interactions.

The first chapter of this thesis consists of a general geological-hydrogeological and climatological overview of the study area.

The second chapter is devoted to the chemical characterization of local groundwaters and the mineralogical and chemical characterization of metabasalts and serpentinites cropping out in the study area. To this purpose, chromatographic and ICP-MS analyses on groundwaters have been carried out on sixty-nine water samples and two suitably selected rock samples, a metabasalt and a serpentinite, have been investigated through optical microscopy of thin sections and different analytical techniques (XRD, XRF, SEM-EDS). In particular, most of the waters samples were classified as Ca-HCO_3 waters whereas less than 3 % of them as Mg-HCO_3 waters. The main rock-forming minerals resulted to be: (i) epidote, amphibole, albite, chlorite, phengite and calcite in the metabasalts and (ii) serpentine minerals and magnetite in the serpentinitic rocks. Furthermore, the second chapter is dedicated to describe the laboratory experiments carried out to investigate the dissolution kinetics of metabasalt and serpentinite and the calculation of the dissolution rates of each solid phases starting from the results obtained for the whole rocks. These experimentally-determined kinetic parameters highlight that: (i) the dissolution rates of individual minerals exhibit minor differences to each other and appear to be close to the whole-rock rate and (ii) the dissolution rates of albite and chlorite are in agreement with literature data measured on separate minerals, whereas those of chlorite, phengite, epidote

and antigorite are not consistent with literature data obtained on single minerals. The obvious implication is that mineral dissolution rates are affected by the presence of other minerals in multi-phase rocks. Dissolution kinetics is probably constrained by the sufficiently abundant mineral(s) of lowest dissolution rate, preventing the dissolution of other faster-dissolving mineral grains as long as these do not come in contact with the aqueous phase. Regarding the experimental work, the study of metabasalt and serpentinite dissolution kinetics was specifically investigated as part of one-year research period at the Lawrence Berkeley National Laboratory (California) and at the Géosciences Environnement Toulouse (Toulouse), respectively.

Chapter 3 presents the results of reaction path modeling of chemical weathering for the metabasalts and serpentinites from the studied area. The application of this powerful geochemical tool, introduced in the late 1960s by Helgeson and coworkers, requires the knowledge of: (i) thermodynamic and kinetic data of relevant minerals, (ii) chemical composition and abundance of each primary phase of interest, (iii) chemical composition of the initial aqueous solution, as well as the definition of boundary conditions. Here, reaction path modeling was performed using the EQ3/6 software package, version 8.0, and adopting the Double Solid Reactant Method (DSRM, Accornero and Marini, 2008; Lelli *et al*., 2008; Apollaro *et al*., 2009; 2011) to simulate the release of trace elements during the progressive dissolution of mineral phases. An updated version of the thermodynamic database data0.ymp.R5, whose characteristics are described by Wolery and Jove-Colon (2007), was used.

Finally, in chapter 4 the most interesting findings achieved through the experimental work of this study on the dissolution kinetics of relevant rocks and minerals are summarized and the results of geochemical models based on literature dissolution rates of single mineral phases are compared with those of corresponding geochemical models involving the dissolution rates retrieved from whole-rock experiments. Comparison of theoretical reaction paths and analytical data for several elements in groundwaters highlights that geochemical modeling involving the kinetic parameters retrieved in this work is more effective than geochemical modeling based on literature data.

Chapter 1 : The study area

1.1. Geological-hydrogeological and climatological background

The different zones of the study area are located in the northern sector of the Calabrian-Peloritan Arc (CPA, Fig. 1), a nappe-structured belt which was produced through the Alpine orogeny and preserves the oldest evidence of both subduction of the Ionian oceanic slab and related opening of the Tyrrhenian back-arc basin (Faccenna *et al*., 2004).

This CPA sector consists of three major structural elements derived from different paleogeographic domains:

1. the Apennine units corresponding to a continental platform made up of low-grade Paleozoic crystalline basement rocks, covered by Mesozoic carbonate deposits (Ietto and Barillaro 1993; Iannace *et al*. 1995; Perrone 1996)
2. the Liguride Complex, representing remnants of the Jurassic Tethys separating the Africa and Europe lithospheric plates (Liberi and Piluso, 2009);
3. the Calabrian Complex consisting of crystalline basement rocks with Hercynian metamorphic and structural imprint intruded by late-Hercynian magmas, on which a Mesozoic sedimentary cover was deposited. The Calabride nappe comprises several tectono-metamorphic units (Amodio Morelli *et al*., 1976).

The study area extends on the central and northern Catena Costiera (zones of Fuscaldo and Malvito), where ophiolitic sequences constitute a thick nappe (Rizzo and Bozzo, 1998) as well as on the Sila Piccola (zones of Gimigliano, Amantea Lake and Monte Reventino).

The Calabrian Catena Costiera is a 70-km-long mountain chain, running in a N-S direction located in the north-western part of Calabria between the Tyrrhenian sea to the west and the Crati valley to the est. It is bounded to the north by the Pollino massif and to the south by the Savuto valley that separates it from the Sila Piccola (Piluso *et al*., 2000).

The Sila Piccola is located in the southern part of the northern sector of CPA and it is bounded to the north by the geographic parallel running across the Arvo Lake and to the south by the Catanzaro trough (Piluso *et al*., 2000).

The Catena Costiera and the Sila Piccola are a nappe system which consists of the three main Complexes described above: (Panormide) Apennine Units, Liguride and

Calabride (Ogniben, 1973). These nappe systems are covered by Neogene-Quaternary sedimentary deposits.

The different zones of the study area are characterized by outcroppings of meta-ophiolitic rocks, mainly metabasalts and subordinate serpentinites. In particular, metabasalts show a complex internal structure because of the deformations into a pattern of tight folds. Both serpentinites and especially metabasalts have a relatively high secondary permeability and host shallow aquifers of limited extension.

The climate of the study areas is upland Mediterranean-type (Csb, sensu Koppen, 1936), with hot, dry summers and precipitation concentrated in mild winters.

In the Sila Piccola, mean yearly rainfall is 1224 mm, with peaks exceeding 2400 mm. Almost 50 % of precipitation falls between November and January, December being the rainiest month with 205 mm. The mean monthly temperature ranges between 7.3 °C, in February, and 23 °C, in August. In the Catena Costiera, mean annual precipitation is 1293 mm, with peaks exceeding 2000 mm. Almost half rains fall between November and January, with a maximum of 204 mm in December. The average monthly temperature varies between a minimum of 8.9 °C, in February, and a maximum of 24.6 °C, in August.

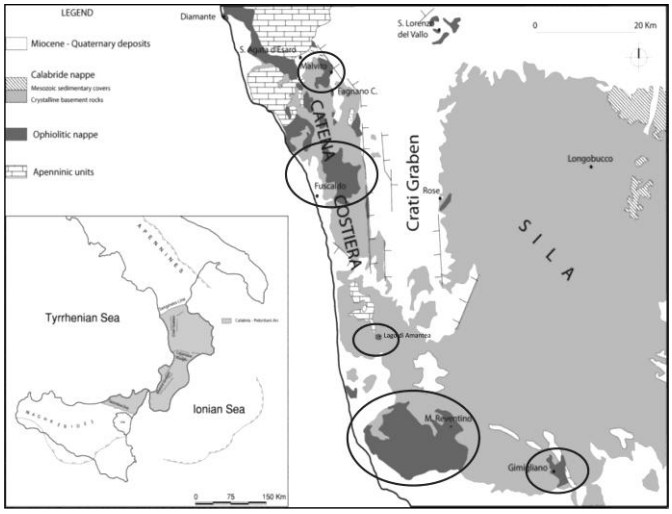

Fig. 1. Geological sketch map of the northern Calabrian Arc and location of the different zones of the study area (black circles; modified after Apollaro *et al*., 2011).

Chapter 2: Experimental work

In this study, sixty-nine spring samples were collected in November 2011 and July 2012.

At each site, temperature, pH, Eh and electrical conductivity (EC) were measured in the field by use of portable instruments. The pH calibration was carried out using buffer solutions HI 7004 and HI 7007, with nominal pH of 4.01 and 7.01 at 25 °C. Measured Eh values were corrected using the ZoBell's solution as reference (Nordstrom, 1977). Total alkalinity was determined by acidimetric titration with HCl 0.01 N using methylorange as indicator. A specially designed microdosimeter was employed to minimize the amount of reactants, facilitating the analysis under field conditions. Dissolved SiO_2 was determined spectrophotometrically by the heteropoly blue-method (Boltz and Mellon, 1947).

Waters were filtered *in situ* through 0.45 µm pore-size polycarbonate membrane filters (Nucleopore), although this method has some limitations because colloidal particles may pass through the filters (e.g., Kennedy and Zellweger, 1974; Laxen and Chandler, 1982).

Samples used for the determination of cations and trace elements were collected in polyethylene bottles, after filtration, and acidification by addition of supra-pure acid (1% HNO_3). Samples for the analyses of anions were stored in polyethylene bottles, without further treatment. New polyethylene bottles were used for all the samples; they were left overnight in dilute HNO_3 and rinsed with Milli-Q demineralised water in the laboratory; in the field they were rinsed three times with small amounts of the aqueous solution being sampled. Blank solutions were prepared in the field using demineralized water and following the same procedure as for water samples.

Chemical analyses were performed in the laboratory of the diBEST of the University of Calabria to determine the abundance of major, minor and trace elements in these groundwaters (Table 1). Major anions and cations were determined by ion-chromatography, using a HPLC DIONEX DX 120, whereas trace elements were determined by a quadrupole Inductively Coupled Plasma-Mass Spectrometer (ICP-MS, Perkin Elmer/SCIEX, Elan DRCe) with a collision reaction cell capable of reducing or avoiding the formation of polyatomic spectral interferences. The analytical accuracy for minor and trace elements was checked by running the NIST1643e standard reference material. The relative error was less than 10% for all analyzed trace elements.

Data quality for major elements was evaluated by charge balance and the deviation from the electroneutrality condition was always less than ±5 %. No contamination was detected from analysis of blank field solutions.

Table. 1 Concentrations of major, minor, and traces elements in groundwater samples from the study areas. Alkalinity (Alk) is in mg HCO_3/L.

Code	pH	T (°C)	Eh (V)	Cond (µS/cm)	SiO_2 (mg/L)	Ca (mg/l)	Mg (mg/L)	K (mg/L)	Na (mg/L)	Cl (mg/L)	SO_4 (mg/L)	Alk (mg/L)	NO_3 (mg/L)	F (mg/L)
S1	7.3	13.4	0.22	342.1	16.0	36.35	18.12	0.73	6.25	9.47	9.56	181.53	5.60	0.08
S2	7.3	10.8	0.39	183.3	8.3	4.04	1.39	1.01	7.99	10.05	2.94	21.00	8.13	<d.l.
S3	7.3	12.4	0.42	589.2	6.0	45.47	7.10	0.22	7.89	10.73	44.27	117.76	1.93	0.07
S4	7.3	11.5	0.41	210.3	5.5	7.24	1.57	0.93	7.62	9.18	6.41	27.00	8.46	0.06
S5	6.1	12.1	0.42	183.9	9.3	2.08	1.56	1.06	8.10	11.23	3.19	13.00	9.99	0.06
S6	8.3	13.5	0.41	354.1	21.5	51.77	15.66	0.55	6.29	9.14	12.50	195.25	5.66	0.05
S7	8.2	13.5	0.41	300.3	14.8	37.39	15.48	0.64	7.23	9.17	7.74	180.00	2.69	0.07
S8	7.7	12.7	0.39	572.2	13.5	34.43	9.05	0.66	8.03	8.38	5.63	135.76	1.80	0.05
S9	7.1	10.9	0.42	517.3	12.3	31.99	5.63	0.48	7.40	8.23	5.92	111.36	2.23	0.05
S10	7.2	10.1	0.42	562.2	11.5	34.96	8.71	1.33	8.04	8.44	5.79	149.49	1.57	0.06
S11	7.4	12.5	0.42	361.4	15.8	47.80	18.89	0.31	8.64	12.03	5.12	225.76	1.39	0.05
S12	7.4	13.5	0.37	293.3	13.0	7.41	10.66	1.69	7.88	7.83	3.97	74.75	0.91	0.06
S13	6.9	9.9	0.23	666.2	13.8	40.83	12.74	0.73	7.17	9.71	5.73	183.05	5.38	0.05
S14	7.8	10.3	0.42	228.1	10.5	30.93	8.23	0.92	7.16	8.16	5.00	122.03	3.67	0.05
S15	7.2	8.7	0.42	216.3	6.0	32.23	6.42	0.70	7.04	8.66	7.61	115.93	5.29	0.04
S16	7.2	8.9	0.42	428.1	13.5	26.42	11.4	0.69	6.63	7.40	4.88	125.08	6.94	0.05
S17	8.0	13.3	0.41	319.4	12.0	60.12	9.08	0.86	9.10	10.59	19.51	161.70	3.75	0.06
S18	6.8	12.2	0.40	246.4	5.0	49.09	4.95	0.64	7.26	8.31	6.24	152.54	<d.l.	0.04
S19	7.9	11.9	0.42	402.2	20.5	53.71	28.57	0.44	8.18	9.99	11.49	277.63	0.37	0.05
S20	7.2	10.9	0.43	344.3	14.0	65.41	14.08	0.45	8.35	8.57	14.58	216.61	1.46	0.04
S21	7.2	12.8	0.42	369.1	10.5	73.37	14.55	0.72	8.41	9.26	17.68	228.81	0.92	0.05
S22	7.4	11.2	0.41	190.2	8.4	3.05	1.50	0.35	8.05	11.06	3.36	24.23	8.25	<d.l.
S23	8.1	13.8	0.4	323.2	19.8	42.90	13.97	0.51	6.01	10.27	13.86	183.05	5.54	0.05
S24	7.1	9.2	0.39	401.3	11.2	21.88	11.28	0.53	5.75	7.99	5.29	111.36	7.02	0.05
S25	7.8	13.6	0.41	310.2	11.5	45.85	8.43	0.77	7.70	11.43	21.42	144.92	3.35	0.06
S26	6.7	12.5	0.37	240.0	4.5	34.52	4.61	0.50	5.99	8.95	6.77	134.24	<d.l.	0.04
S27	7.7	12.2	0.39	389.3	19.5	44.42	23.75	0.40	7.12	10.70	12.63	242.54	0.39	0.05
S28	7.1	11.2	0.42	310.3	12.3	45.94	12.79	0.32	6.80	9.20	16.01	187.63	1.67	0.04
S29	7.1	13.1	0.4	340.2	10.2	53.59	13.30	0.63	7.03	10.00	19.48	199.83	0.85	0.05
SP 8	6.9	10.1	0.41	74.3	4.0	4.18	0.90	0.34	5.98	8.15	4.05	17.08	1.13	0.03
SP 10	6.6	13.1	0.40	59.8	6.8	1.59	0.56	0.28	6.52	8.43	3.15	7.58	1.84	0.03
SP 11	6.2	11.4	0.42	78.0	9.0	3.00	1.61	0.58	7.66	9.85	3.11	15.86	4.51	0.02
SP 12	7.1	10.9	0.42	133.1	7.8	16.76	2.58	0.46	7.41	9.53	5.25	50.95	1.85	0.03
SP 13	6.6	9.6	0.44	81.8	5.8	7.31	1.52	0.40	6.13	7.31	3.69	28.37	0.90	0.03
SP 46	6.2	9.2	0.44	66.4	6.0	3.55	1.43	0.39	7.78	8.73	4.08	14.63	0.75	0.02

Table 1, continued

Code	Li (µg/L)	B (µg/L)	Al (µg/L)	V (µg/L)	Mn (µg/L)	Fe (µg/L)	Cr (µg/L)	Co (µg/L)	Ni (µg/L)	Cu (µg/L)	Zn (µg/L)	As (µg/L)	Sr (µg/L)	Mo (µg/L)	Cd (µg/L)
S1	<d.l.	9.13	1.66	<d.l.	0.30	3.83	3.08	0.36	7.75	0.07	14.84	0.25	46.68	<d.l.	0.11
S2	<d.l.	5.17	0.54	<d.l.	0.58	0.84	<d.l.	<d.l.	0.28	<d.l.	37.21	0.07	23.29	<d.l.	<d.l.
S3	<d.l.	<d.l.	<d.l.	<d.l.	<d.l.	0.90	<d.l.	0.23	0.64	<d.l.	2.59	2.60	109.23	<d.l.	<d.l.
S4	<d.l.	5.78	0.92	<d.l.	0.15	4.13	<d.l.	0.22	0.29	0.03	10.17	0.13	44.21	1.96	<d.l.
S5	<d.l.	<d.l.	18.72	<d.l.	2.52	0.26	<d.l.	<d.l.	1.06	0.28	13.42	0.19	13.51	0.35	<d.l.
S6	<d.l.	5.79	1.92	<d.l.	0.11	3.29	3.55	<d.l.	2.48	<d.l.	39.72	0.14	67.66	0.68	<d.l.
S7	<d.l.	5.97	<d.l.	<d.l.	0.26	4.49	2.28	<d.l.	4.38	0.16	<d.l.	0.18	27.42	1.22	<d.l.
S8	0.73	6.33	3.22	<d.l.	<d.l.	2.20	2.03	<d.l.	0.88	0.07	39.37	0.04	22.27	<d.l.	<d.l.
S9	0.70	5.47	0.65	<d.l.	<d.l.	3.77	1.05	<d.l.	0.76	0.03	51.26	0.03	13.30	1.16	<d.l.
S10	0.92	5.64	<d.l.	<d.l.	<d.l.	10.02	2.82	<d.l.	1.13	0.28	6.07	0.01	16.95	0.70	<d.l.
S11	0.87	6.37	1.97	<d.l.	<d.l.	4.13	6.34	<d.l.	9.05	0.37	14.69	0.02	44.40	5.34	<d.l.
S12	<d.l.	5.10	<d.l.	<d.l.	<d.l.	0.93	0.16	<d.l.	1.54	0.30	3.23	<d.l.	21.61	<d.l.	<d.l.
S13	0.54	8.46	<d.l.	<d.l.	<d.l.	<d.l.	9.28	<d.l.	1.40	0.81	<d.l.	<d.l.	22.35	<d.l.	<d.l.
S14	<d.l.	7.38	6.26	<d.l.	0.15	2.81	3.23	<d.l.	2.95	0.66	21.79	0.40	20.49	6.88	<d.l.
S15	<d.l.	7.67	0.15	<d.l.	<d.l.	1.31	5.38	<d.l.	1.38	<d.l.	10.08	<d.l.	19.17	0.35	<d.l.
S16	<d.l.	7.53	1.67	<d.l.	<d.l.	<d.l.	5.89	<d.l.	7.22	0.08	12.31	<d.l.	16.56	0.55	<d.l.
S17	0.75	9.21	5.74	<d.l.	0.16	0.98	0.62	<d.l.	1.78	0.39	<d.l.	1.02	180.66	2.15	<d.l.
S18	0.84	4.57	2.98	<d.l.	0.11	4.15	<d.l.	<d.l.	0.89	0.70	47.45	<d.l.	52.90	<d.l.	<d.l.
S19	<d.l.	8.74	2.08	<d.l.	2.29	3.23	2.02	<d.l.	12.74	0.20	<d.l.	0.44	42.86	<d.l.	<d.l.
S20	0.61	6.93	1.42	1.07	<d.l.	16.90	4.62	<d.l.	1.90	0.68	<d.l.	0.28	40.75	<d.l.	<d.l.
S21	0.71	6.91	1.95	0.76	<d.l.	1.51	4.18	<d.l.	2.23	0.52	<d.l.	0.28	66.17	<d.l.	<d.l.
S22	<d.l.	2.58	9.63	<d.l.	1.55	0.55	<d.l.	<d.l.	0.67	0.14	25.31	0.13	18.40	0.17	0.00
S23	0.38	7.50	3.83	<d.l.	0.76	2.13	2.09	<d.l.	2.13	0.19	19.86	0.58	180.66	1.42	<d.l.
S24	<d.l.	7.60	0.91	<d.l.	<d.l.	0.66	5.63	<d.l.	4.30	0.04	11.19	0.00	17.87	0.45	<d.l.
S25	0.38	7.50	3.83	<d.l.	0.14	2.13	2.09	0.00	2.13	0.19	19.86	0.58	124.16	1.42	<d.l.
S26	0.88	5.10	1.49	<d.l.	0.35	7.08	1.41	0.00	1.01	0.89	26.76	0.33	45.90	0.35	<d.l.
S27	0.36	7.82	2.01	0.38	2.50	2.37	3.10	<d.l.	7.49	0.36	<d.l.	0.36	54.51	0.00	<d.l.
S28	0.74	6.65	1.70	0.53	<d.l.	10.51	5.48	<d.l.	5.47	0.53	7.35	0.15	42.58	2.67	<d.l.
S29	0.66	6.92	1.68	0.91	<d.l.	9.21	4.40	<d.l.	2.06	1.30	<d.l.	0.28	80.40	<d.l.	<d.l.
SP 8	0.07	8.42	5.60	0.43	0.49	5.01	0.11	0.01	0.43	0.85	<d.l.	0.09	14.42	1.01	0.01
SP 10	0.06	8.19	10.12	0.25	0.40	15.40	0.10	0.01	0.23	0.38	2.67	0.08	14.11	<d.l.	<d.l.
SP 11	0.17	8.20	<d.l.	0.59	0.01	6.29	0.26	0.01	0.29	0.51	0.92	0.12	17.73	0.81	0.01
SP 12	0.21	10.55	<d.l.	3.01	<d.l.	3.82	0.34	0.02	0.36	0.43	<d.l.	0.45	21.83	0.26	<d.l.
SP 13	0.10	8.94	3.44	0.67	0.09	9.83	0.29	0.03	0.30	0.38	2.05	0.08	21.95	0.40	<d.l.
SP 46	0.08	8.34	<d.l.	0.45	<d.l.	4.64	0.20	0.01	0.14	0.36	<d.l.	0.08	12.20	0.09	0.001

Table 1, continued

Code	pH	T (°C)	Eh (V)	Cond (µS/cm)	SiO_2 (mg/L)	Ca (mg/l)	Mg (mg/L)	K (mg/L)	Na (mg/L)	Cl (mg/L)	SO_4 (mg/L)	Alk (mg/L)	NO_3 (mg/L)	F (mg/L)
TC 1	6.9	7.3	0.28	54.2	4.0	1.35	0.63	0.26	6.20	5.65	4.08	7.02	0.73	0.02
TC 2	6.7	8.9	0.38	240.0	2.0	2.50	1.52	0.41	5.26	5.41	5.27	8.54	5.80	0.02
TC 3	7.7	9.2	0.41	218.0	4.5	27.30	1.49	0.26	5.94	6.70	10.59	77.49	4.07	0.02
TC 4	6.7	8.5	0.42	101.1	7.0	8.33	0.97	0.33	5.62	4.66	2.21	33.86	3.54	0.01
TC 6	6.7	18.0	0.54	150.3	26.3	7.24	6.91	1.51	11.66	16.09	4.47	57.36	<d.l.	0.08
TC 7	7.7	17.3	0.45	360.0	9.8	72.13	2.10	0.89	7.24	12.27	8.74	212.95	0.42	0.05
TC 8	7.8	18.3	0.42	502.0	8.0	113.01	2.95	1.32	11.38	22.28	12.29	299.93	<d.l.	0.06
TC 9	7.4	16.9	0.49	463.0	9.3	102.87	4.25	0.86	10.24	17.67	11.42	286.64	<d.l.	0.09
GIM 2	8.2	18.6	0.32	567.0	10.5	72.40	23.36	2.99	16.72	25.53	55.49	256.27	4.85	0.33
GIM 3	7.7	16.9	0.38	647.0	9.2	20.38	29.34	3.54	76.02	32.20	58.24	289.83	14.45	0.20
GIM 10	8.0	15.1	0.45	527.0	19.6	42.35	12.59	24.67	35.58	30.23	21.09	183.05	47.03	0.18
GIM 11	8.0	17.8	0.37	272.0	n.d.	35.27	2.59	8.05	15.61	26.09	30.30	73.22	11.78	0.21
VB 5	6.6	13.0	0.39	233.0	18.5	14.77	13.54	0.89	12.40	19.29	6.91	102.20	<d.l.	0.05
VB 8	7.4	11.2	0.44	350.0	4.0	60.66	1.34	0.45	7.44	9.44	13.72	175.42	4.86	0.02
VB 9	7.3	12.2	0.40	306.0	8.5	49.93	2.17	0.64	8.27	8.01	7.68	147.97	7.98	0.02
VB 32	7.4	13.0	0.44	409.0	8.5	64.46	9.94	0.27	5.90	10.54	8.57	210.51	1.82	0.04
VB 33	7.4	12.8	0.42	902.0	9.0	151.94	66.77	1.29	7.35	13.96	314.30	398.14	1.92	0.12
VB 34	7.1	12.0	0.38	227.0	15.3	33.14	3.09	0.97	9.29	10.10	3.56	122.03	1.81	0.11
VB 35	7.0	13.8	0.39	211.0	8.8	25.96	1.46	0.20	7.94	10.23	6.74	74.75	0.92	0.04
VB 36	8.2	17.8	0.43	337.0	8.8	53.29	2.70	0.15	7.83	10.42	10.63	155.59	2.11	0.15
VB 37	7.3	15.3	0.45	343.0	8.5	59.02	1.43	0.33	8.14	11.72	6.07	166.27	9.63	0.07
VB 38	7.5	14.7	0.39	360.0	9.5	66.62	2.34	0.61	7.76	9.64	4.19	195.25	4.70	0.12
LAGO 1	7.2	12.0	n.d.	171.4	7.5	20.15	3.97	0.89	10.55	13.09	13.30	79.32	<d.l.	<d.l.
LAGO 3	7.6	14.6	n.d.	247.0	25.5	14.59	23.95	0.78	9.47	11.39	12.80	152.54	<d.l.	<d.l.
LAGO 4	7.5	12.7	n.d.	212.0	15.8	20.00	13.77	0.95	10.19	12.01	9.68	134.24	<d.l.	<d.l.
LAGO 5	8.1	13.6	n.d.	275.0	15.5	20.60	26.37	0.59	8.10	11.45	18.55	170.85	<d.l.	<d.l.
LAGO 6	8.1	12.6	n.d.	270.0	16.3	30.16	14.41	1.06	9.54	11.58	11.47	152.54	<d.l.	<d.l.
LAGO 7	7.6	13.3	n.d.	349.0	28.5	20.27	36.33	0.56	9.53	12.07	9.54	225.76	<d.l.	<d.l.
LAGO 8	8.2	13.3	n.d.	356.0	32.8	32.21	31.82	0.89	10.34	14.09	12.17	219.66	<d.l.	<d.l.
LAGO9	7.3	17.2	0.06	493.0	16.3	59.83	15.43	1.26	14.27	16.57	32.12	232.27	<d.l.	0.43
LAGO15	7.5	13.8	0.42	458.0	7.3	61.22	16.36	0.71	12.84	13.52	11.55	236.50	1.09	0.16
LAGO14	7.3	14.8	0.31	322.0	10.5	36.14	10.09	0.99	9.64	11.66	15.85	145.95	5.69	0.14
LAGO16	7.1	15.0	0.29	260.0	6.0	27.56	4.63	1.98	13.19	15.06	17.75	83.18	8.63	0.15
LAGO17	6.6	19.0	0.27	163.3	8.0	10.68	3.70	0.94	11.64	13.47	10.09	42.37	5.41	0.63

Table 1, continued

Code	Li (µg/L)	B (µg/L)	Al (µg/L)	V (µg/L)	Mn (µg/L)	Fe (µg/L)	Cr (µg/L)	Co (µg/L)	Ni (µg/L)	Cu (µg/L)	Zn (µg/L)	As (µg/L)	Sr (µg/L)	Mo (µg/L)	Cd (µg/L)
TC 1	0.12	9.05	8.35	0.10	0.003	4.52	<d.l.	0.02	0.21	0.39	1.87	0.10	11.53	<d.l.	<d.l.
TC 2	0.08	8.23	7.34	0.05	0.01	6.35	<d.l.	0.03	0.27	0.24	3.94	<d.l.	14.33	2.93	<d.l.
TC 3	0.52	7.92	<d.l.	0.12	<d.l.	12.77	0.17	0.04	0.81	0.11	6.26	0.11	101.02	0.01	<d.l.
TC 4	0.14	6.99	3.57	0.62	<d.l.	5.55	0.14	0.02	0.17	1.61	1.36	0.12	20.35	<d.l.	<d.l.
TC 6	0.50	8.65	11.29	0.30	0.59	11.30	0.32	0.03	2.30	0.35	2.64	<d.l.	65.26	2.82	<d.l.
TC 7	1.23	10.48	<d.l.	0.14	0.02	4.46	0.20	0.08	1.21	0.39	2.06	0.15	129.53	0.65	<d.l.
TC 8	1.05	7.50	<d.l.	0.14	10.84	11.46	0.02	0.11	1.89	0.44	2.29	0.11	172.71	0.31	<d.l.
TC 9	0.45	9.31	<d.l.	0.79	0.62	15.92	0.34	0.10	1.97	1.05	3.07	0.16	208.67	0.36	<d.l.
GIM 2	3.41	25.72	5.91	<d.l.	0.36	13.62	6.36	0.10	2.07	0.55	2.07	0.29	282.33	0.64	4.35
GIM 3	5.45	52.86	4.66	1.99	0.08	13.37	4.28	0.30	5.26	2.41	2.15	1.53	350.96	0.91	0.61
GIM 10	0.94	96.19	<d.l.	10.64	0.14	3.35	22.60	0.11	2.27	1.74	1.24	2.27	70.67	3.38	0.25
GIM 11	1.79	18.49	22.26	0.60	4.30	7.68	0.39	0.15	2.02	1.73	1.77	4.43	1508.47	6.67	0.07
VB 5	0.26	12.42	<d.l.	0.38	4.87	44.49	0.24	0.06	0.78	0.52	3.40	0.09	52.85	0.48	<d.l.
VB 8	0.10	9.03	4.62	0.41	0.11	9.48	0.33	0.05	0.98	0.43	0.57	0.08	153.86	2.14	0.01
VB 9	0.93	9.85	<d.l.	0.04	0.02	6.13	0.08	0.06	1.15	0.22	0.76	<d.l.	216.27	0.20	<d.l.
VB 32	1.40	13.51	<d.l.	0.65	0.89	11.69	1.48	0.07	1.11	<d.l.	<d.l.	0.09	130.76	1.18	<d.l.
VB 33	2.80	11.58	<d.l.	0.01	<d.l.	6.40	<d.l.	0.11	1.80	<d.l.	0.75	0.09	1322.16	0.52	<d.l.
VB 34	0.52	11.43	<d.l.	1.59	<d.l.	8.89	0.36	0.03	0.18	<d.l.	1.30	0.26	79.12	<d.l.	<d.l.
VB 35	0.05	13.04	<d.l.	1.02	0.71	14.76	0.33	0.04	0.32	<d.l.	4.23	<d.l.	54.54	0.04	<d.l.
VB 36	0.19	10.44	9.78	0.55	0.58	15.15	0.44	0.08	1.17	0.13	3.06	0.10	186.99	0.31	0.004
VB 37	0.20	8.90	9.58	0.84	0.72	12.81	0.26	0.08	1.46	0.79	4.16	0.11	109.05	0.08	0.01
VB 38	0.16	9.08	3.80	0.94	0.48	7.11	0.38	0.08	1.45	0.90	3.70	0.15	101.77	0.07	0.01
LAGO 1	1.75	10.21	11.33	0.36	<d.l.	11.64	<d.l.	<d.l.	1.03	1.23	3.55	0.19	111.15	0.59	0.09
LAGO 3	0.45	19.08	5.63	3.64	<d.l.	8.32	2.29	<d.l.	10.63	0.88	1.46	0.36	71.76	0.42	0.06
LAGO 4	0.48	11.58	9.09	0.99	<d.l.	9.35	15.78	<d.l.	1.08	1.79	3.03	<d.l.	64.69	0.72	0.07
LAGO 5	3.18	27.20	6.73	0.38	148.89	182.39	<d.l.	0.36	1.30	0.50	1.67	0.90	122.06	1.00	0.06
LAGO 6	1.70	12.26	4.98	0.34	<d.l.	21.86	2.43	<d.l.	0.64	1.19	4.86	0.59	62.19	0.37	0.06
LAGO 7	0.43	13.40	12.45	1.28	<d.l.	17.35	5.65	<d.l.	29.22	1.44	2.82	0.23	60.34	0.49	0.10
LAGO 8	1.02	17.00	9.51	2.90	5.97	22.00	19.87	<d.l.	9.31	0.57	205.98	0.51	76.33	0.30	0.08
LAGO 9	12.58	26.12	<d.l.	0.03	110.74	4331.55	<d.l.	<d.l.	0.22	0.03	4.96	0.23	244.72	<d.l.	<d.l.
LAGO 15	1.39	20.09	4.91	1.04	0.82	9.86	<d.l.	<d.l.	<d.l.	0.19	10.71	0.27	191.14	<d.l.	<d.l.
LAGO 14	0.89	11.01	<d.l.	1.19	<d.l.	2.49	2.43	<d.l.	<d.l.	1.21	14.72	<d.l.	154.55	<d.l.	<d.l.
LAGO 16	0.26	12.90	<d.l.	0.10	<d.l.	3.53	<d.l.	<d.l.	<d.l.	0.30	37.74	<d.l.	137.55	<d.l.	<d.l.
LAGO 17	0.59	8.82	<d.l.	0.10	<d.l.	3.36	<d.l.	<d.l.	<d.l.	0.55	28.27	0.20	46.71	<d.l.	<d.l.

2.1 Chemical characteristics of groundwaters circulating in metabasalts and serpentinites

The average water temperature is 13.5 ± 2.7 °C (1σ), pH values range from 6 to 8.3, and Eh from 61 to 539 mV (Table 1), which indicates oxidizing conditions.

The chemical composition of waters was inspected in terms of Cl, SO_4 and HCO_3 contents (Fig. 2a) and Na+K, Ca and Mg contents (Fig. 2b), based on concentrations in equivalent units.

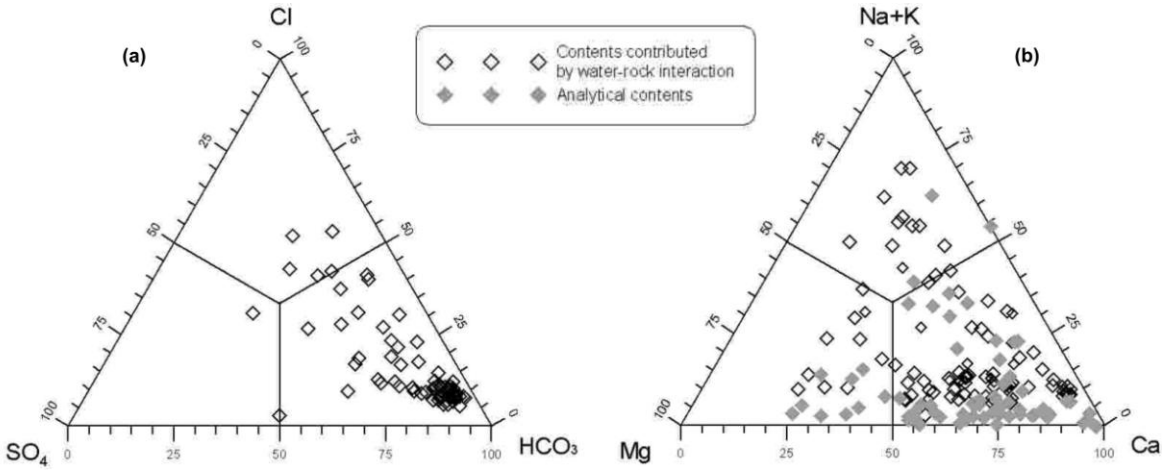

Fig. 2. Triangular plots involving (a) HCO_3^-, SO_4^{2-}, and Cl^- and (b) Ca^{2+}, Mg^{2+}, and Na^++K^+, both prepared from concentrations in equivalent units. In (b) both analytical concentrations and those contributed by water-rock interactions are shown for the spring waters from the study area.

As shown in Fig. 2a, all the samples are situated in the HCO_3 field which indicates that the chemistry of local shallow groundwater is chiefly dominated by conversion of CO_2 in HCO_3^- ion through water-rock interaction (Garrels, 1968).

As suggested in Apollaro *et al.* (2011) the atmospheric-marine component (subscript SW) entrained in local groundwaters (subscript G) was subtracted from the analytical (total) concentration of the *i*th dissolved component, by means of the simple equation (all $C_{i,SW}$ concentrations C in mg/L):

$$C_{i,WR,G} = C_{i,G} - \frac{C_{i,SW}}{C_{Cl,SW}} \cdot C_{Cl,G} \qquad (1)$$

In equation (1) chloride is used as reference component and the average seawater composition is taken from Nordstrom *et al.* (1979). This correction is based on the fact that the atmospheric-marine component dominates the chemistry of rain waters in coastal areas (Appelo and Postma, 1999), as is the case of the study area. Furthermore, Arnórsson and Andrésdóttir (1995) who worked on a large set of Icelandic natural waters, showed that seawater spray and aerosols are the main source of Cl and B in surface waters and in cold groundwaters. Stefánsson and Gislason (2001) computed seawater contributions of Cl from 86% to 100% of total dissolved Cl, by means of Cl and B mass balances, in surface waters and groundwaters from a basaltic catchment of southern Iceland. Eq. (1) is consistent with

these observations and it assumes that Cl is completely contributed by the atmospheric-marine component while the Cl supplied by water-rock interaction is nil.

The concentrations of dissolved constituents ascribable to water-rock interaction (subscript WR) are obtained by means of Eq. (1).

The cationic plot of Fig. 2b, also reporting data corrected from the atmospheric-marine component, enlightens the prevalence of calcium-rich waters affected by the dissolution of Ca-rich phases present in metabasalts. In particular, calcite seems to be the main Ca-supplier because of its presence in local metabasalts (see section 2.2) and its very high far-from-equilibrium dissolution rate compared to that of Ca-bearing silicates and Al-silicates (see rate data compilations, e.g. Palandri and Kharaka, 2004; Marini, 2007; Bandstra *et al*., 2008 and references therein). A small group of HCO_3 groundwaters are enriched in Mg owing to the interaction of meteoric water with ultramafic rocks, variably affected by serpentinization (e.g., Bruni *et al*., 2002; Fantoni *et al*., 2002; Cipolli *et al*., 2004).

The small number of groundwaters characterized by high relative Cl^- contents, is also enriched in relative Na and K and can be interpreted as immature waters which are scarcely modified by water-rock interaction and are still representative of local meteoric precipitation.

The Langelier Ludwig (LL) diagram of HCO_3 vs. Mg+Na+K (Fig. 3a) shows that two different trends depart from the immature Na-Cl waters of low salinity, pointing towards Ca-HCO_3 and Mg(Na+K)-HCO_3 compositions, that is towards the lower-right and higher-right vertices, respectively, in this square LL diagram.

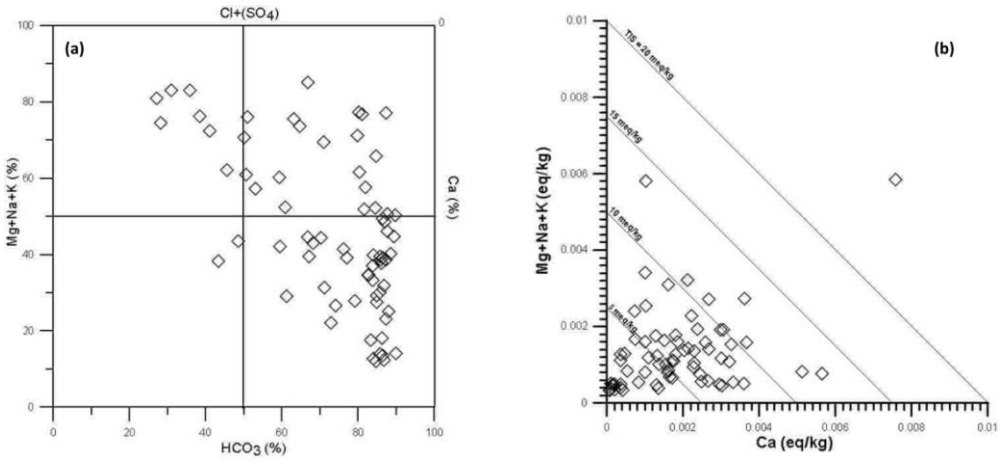

Fig. 3. (a) Square diagram of Langelier-Ludwig with alkalinity vs. Mg+Na+K and (b) salinity plot.

The salinity diagram of Fig. 3b, which refers to the triangular section passing through the edges of Mg+Na+K concentrations and Ca concentration of the compositional pyramid of LL, shows that sample VB33 has salinity higher than 35 meq/kg, Mg(Na+K)-HCO_3 waters have low salinity (< 5 meq/kg) and Ca-HCO_3 waters have intermediate salinity (5-15 meq/kg).

2.2 Chemical characteristics of rocks and minerals

The compositional features of groundwaters depend on the extent of water-rock interaction and the mineralogy of local rocks. Therefore, the mineralogical and chemical characterization of metabasalts and serpentinites cropping out in the study area represents a mandatory step to better understand the chemical evolution of groundwaters. As such, five representative samples from metabasalts and seven from serpentinites were selected, on the basis of macroscopic characteristics, for mineralogical and chemical analyses.

Primary mineral phases of the studied rocks were identified through both optical microscopy of thin sections and X-ray Diffraction (XRD) analysis using a Bruker D8 Advance XRD Diffractometer.

Point analyses on single primary minerals were carried out on polished carbon-coated thin sections through an Environmental Scanning Electron Microscope FEI QUANTA 200 equipped with a X-ray EDS suite comprising a Si/Li crystal detector model EDAX-GENESIS-4000. This technique allowed us to determine the stoichiometry of the main primary phases, whereas trace element contents were measured by Laser Ablation ICP-MS (LA-ICP-MS).

Whole-rock analyses were performed by X-ray fluorescence spectroscopy (XRF) using a Philips PW 1480 XRF spectrometer. X-ray counts were converted into concentrations by a computer program based on the matrix correction method described by Franzini *et al.* (1975). The certified international reference materials AGV-1, BCR-1, BR, DR-N, GA, GSP-1 and NIM-G were used as monitors of data quality.

XRD analysis and optical microscopy of thin sections revealed that metabasalts are made up of chlorite, epidote, actinolite and albite, with small quantities of phengite and calcite. According to Liberi *et al.* (2006), Na-amphibole, prehnite and titanite are also present in this rock, as accessory phases. However, their effect on water chemistry is expected to be minor to negligible owing to their very small amounts and high durability, at least for titanite. The paragenesis of serpentinites is composed of antigorite with subordinate

magnetite. The weight percentages of primary minerals in the two bulk rocks were evaluated by Apollaro *et al*. (2011) based on the median concentrations of major oxides in the two lithotypes of interest (given by XRF analysis; Table 2) and in each solid phases (obtained by SEM-EDS analysis; Table 3).

Table 2. Concentrations of major oxides in bulk rock samples of metabasalts and serpentinites from the study area. Data obtained from XRF analysis. Median concentrations in primary minerals and calculated weight percentages of primary minerals in the two bulk rocks are also reported.

Sample	Computed % of minerals in the bulk rock (wt.%)	SiO_2 (wt%)	Al_2O_3 (wt%)	Fe_2O_3 (wt%)	MgO (wt%)	CaO (wt%)	Na_2O (wt%)	K_2O (wt%)
Serpentinite- A8		41.64	1.65	13.22	43.25	0.07		0.00
Serpentinite-A10		44.16	0.65	10.61	44.48			
Serpentinite-A11		43.79	0.99	10.92	44.11	0.07		0.00
Serpentinite-A16		39.84	6.70	10.72	42.01	0.06		0.01
Serpentinite-A18		42.22	2.07	12.50	42.56	0.49		
Median serpentinite		42.22	1.65	10.92	43.25	0.07		
Antigorite, median	94.6							
Magnetite, median	5.4							
Computed serpentinite		44.97	0.65	9.10	36.46			
Metabasite_a19		46.36	12.95	13.73	12.59	8.36	3.32	0.02
Metabasite_a26		45.49	14.61	11.98	13.59	8.3	3.74	0.05
Metabasite_a28		38.97	16.25	12.87	9.62	19.26	0.08	0.01
Metabasite_a20		42.44	14.49	13.71	11.17	12.63	1.79	0.83
Metabasite_a5		40.88	23.72	10.52	3.3	18.2	2.1	0.25
Median metabasalt		42.44	14.61	12.87	11.17	12.63	2.1	0.05
Epidote, median	26.2	41.03	23.44	13.53		21.6		
Albite, median	13.7	69.35	19.35				11.2	
Phengite, median	2.8	50.72	35.15	1.69	2.63	0	1.15	8.66
Actinolite, median	23.4	51.51	4.91	9.39	13.73	17.27	1.5	
Chlorite, median	30.3	34.23	20.97	20.55	22.6		1.26	
Calcite, median	3.6					56.03		
Computed metabasalt		44.12	17.28	12.02	10.14	11.69	2.3	0.24

Table 3. Concentrations of major oxides in primary minerals of metabasalt and serpentinite samples from the study area. Data obtained through SEM–EDS analysis.

Rock	Mineral	Code	SiO_2 (wt%)	TiO_2 (wt%)	Al_2O_3 (wt%)	Fe_2O_3 (wt%)	MgO (wt%)	CaO (wt%)	Na_2O (wt%)	K_2O (wt%)
Metabasalt	Amphibole	a 20_001	51.59	1.51	4.60	9.26	14.34	17.27	1.44	
Metabasalt	Amphibole	a 20_004	51.43	1.32	5.22	7.90	16.00	16.63	1.50	
Metabasalt	Amphibole	a 26_001	51.13	2.12	5.31	9.52	13.11	18.80		
Metabasalt	Albite	a 19_001	69.07		19.35				11.58	
Metabasalt	Albite	a 19_007	70.33		19.44				10.22	
Metabasalt	Albite	a 19_015	70.07		19.32				10.61	
Metabasalt	Albite	a 20_009	69.03		19.37				11.60	
Metabasalt	Albite	a 20_013	68.13		19.35				12.52	
Metabasalt	Albite	a 26_005	69.35		19.45				11.20	
Metabasalt	Albite	a 26_006	69.24		19.33				11.43	
Metabasalt	Albite	a 26_010	69.77		19.54				10.69	
Metabasalt	Albite	a 26_012	70.13		19.24				10.63	
Metabasalt	Epidote	a 5_002	40.62		24.06	13.37		21.96		
Metabasalt	Epidote	a 5_007	41.07		26.10	10.45		22.38		
Metabasalt	Epidote	a 20_003	41.6		23.6	13.5		21.3		
Metabasalt	Epidote	a 20_007	40.99		22.82	15.00		21.20		
Metabasalt	Epidote	a 20_008	40.89		22.89	14.32		21.90		
Metabasalt	Epidote	a 20_010	41.99		23.31	13.53		21.17		
Metabasalt	Epidote	a 28_001	40.56		23.16	14.11		22.17		
Metabasalt	Epidote	a 28_006	42.51		24.38	12.65		20.46		
Metabasalt	Chlorite	a 5_003	35.21		20.33	15.02	29.44			
Metabasalt	Chlorite	a 5_006	34.89		20.13	17.52	27.46			
Metabasalt	Chlorite	a 5_009	34.23		21.20	17.32	27.25			
Metabasalt	Chlorite	a 19_003	32.47		20.97	24.29	22.26			
Metabasalt	Chlorite	a 19_008	33.16		20.39	25.19	21.26			
Metabasalt	Chlorite	a 19_010	38.46		20.83	20.48	18.17		2.07	
Metabasalt	Chlorite	a 19_013	32.24		20.57	25.25	21.48		0.45	
Metabasalt	Chlorite	a 20_011	36.07		20.79	20.55	22.60			
Metabasalt	Chlorite	a 26_ 002	35.31		21.25	16.89	26.56			
Metabasalt	Chlorite	a 26_ 004	34.39		21.48	17.74	26.39			
Metabasalt	Chlorite	a 26_ 007	34.48		21.52	17.05	26.96			
Metabasalt	Chlorite	a 26_ 008	33.5		21.3	20.6	24.7			
Metabasalt	Chlorite	a 28_008	32.36		19.31	31.35	16.98			
Metabasalt	Chlorite	a 28_009	33.00		21.45	25.43	20.12			
Metabasalt	Chlorite	a 28_010	32.22		21.33	28.90	17.55			
Metabasalt	Phengite	a 28_007	50.72		35.15	1.69	2.63		1.15	8.66
Serpentinite	Antigorite	a 18_003	49.66		1.20	2.24	46.91			
Serpentinite	Antigorite	a 17_001	48.95		1.96	4.55	44.54			
Serpentinite	Antigorite	a 10_005	45.72			3.64	38.14			
Serpentinite	Antigorite	a 10_006	44.88		1.06	4.10	37.47			
Serpentinite	Antigorite	a 10_007	45.05		0.95	4.81	36.70			
Serpentinite	Antigorite	a 10_011	43.94			3.98	39.23			
Serpentinite	Antigorite	a 10_012	44.65			4.14	38.71			
Serpentinite	Antigorite	a 10_013	44.06			3.98	39.46			
Serpentinite	Antigorite	a 10_017	43.54		1.45	3.55	38.24			
Serpentinite	Antigorite	a 10_018	44.42		1.19	3.63	38.26			
Serpentinite	Antigorite	a 10_021	43.23		0.95	2.93	40.39			
Serpentinite	Antigorite	a 10_022	43.14		1.23	4.35	38.78			
Serpentinite	Magnetite	a 10_007	1.92			96.82	1.26			
Serpentinite	Magnetite	a 17_002	1.21		0.50	97.19	1.10			
Serpentinite	Magnetite	a 17_004	1.39		0.53	96.64	1.43			

The analysis of primary minerals have been performed on both metabasalts and serpentinites and showed that the computed oxide contents is in satisfactory agreement with the corresponding XRF analytical data (Table 2). Therefore, it can be concluded that the estimated weight percentages of primary minerals (also given in Table 2) have acceptable precision for the purposes of this investigation. SEM-EDS data on constituting

minerals of metabasalts (Table 3) indicate that chlorites have a number of Si atoms per formula units from 5.95 to 7.02 with an average of 6.21 and a number of Fe^{2+} + Fe^{3+} atoms per formula units from 1.98 to 4.54 with a mean of 2.97. According to the classification of Hey (1954), these chlorites plot in the fields of pycnochlorite and diabantite but, even if the number of Si atoms is somewhat too high, they can be considered, to a first approximation, as solid solutions of 14 Å-clinochlore and 14 Å-daphnite, with average molar fractions of 0.68 and 0.32, respectively. These are the only chlorite components for which thermodynamic data are available, from Helgeson *et al*. (1978) and Wolery (1978), respectively. The thermodynamic data of these authors were slightly revised by Wolery and Jove-Colon (2007).

Actinolitic amphibole is a solid solution of tremolite (74% on average) and ferro-actinolite (26% on average) but the lack of thermodynamic data for ferro-actinolite[1] prompted us to consider it as a solid solution of tremolite (83% on average) and grunerite (17% on average), for which thermodynamic data are available (Helgeson *et al*.,1978; Robie and Hemingway, 1995). A simplification has been assumed because grunerite strictly is expected to mix with cummingtonite but it is monoclinic and belongs to space group C 2/m as tremolite and ferro-actinolite. The average stoichiometry of epidote is $Ca_{1.79}Fe_{0.79}Al_{2.13}Si_{3.17}O_{12}(OH)$ which compares with the idealized chemical formula of the epidote adopted by Helgeson *et al*. (1978), $Ca_2FeAl_2Si_3O_{12}(OH)$, for computing its thermodynamic properties.

Plagioclase is pure albite, within analytical uncertainties. Thermodynamic data of albite are from Helgeson *et al.* (1978).

Calcium carbonate is virtually pure calcite, whose thermodynamic properties are from Helgeson *et al.* (1978).

Finally, phengite has an average stoichiometry $K_{0.69}Na_{0.14}Fe_{0.08}Mg_{0.25}\ Al_{2.60}Si_{3.18}O_{10}(OH)_2$, which is relatively similar to the phengite defined by Apollaro *et al.* (2009), whose chemical formula is $K_{0.81}Fe_{0.15}Mg_{0.22}Al_{2.31}Si_{3.32}O_{10}(OH)_2$. Due to the considerable

[1] Thermodynamic data for ferro-actinolite are actually reported by Holland and Powell (1998), but the standard Gibbs free of formation of tremolite at 25 °C given by these authors, -2,768.026 kcal/mol differs by 2.659 kcal/mol (which is an extremely high figure) from the corresponding value reported by Wolery and Jove-Colon (2007), -2,770.685 kcal/mol. This discrepancy suggests that data from these two compilations are not mutually consistent and cannot be mixed together.

analytical uncertainties and the small amounts of this mineral, the thermodynamic data of the phengite of Apollaro *et al.* (2009) were adopted also in this work.

Results of SEM–EDS analyses on solid phases of serpentinites (Table 3) indicate that antigorite has an average chemical formula of $Mg_{2.75}Fe_{0.07}Al_{0.07}Si_{1.93}O_5(OH)_{3.65}$, which is relatively close to the stoichiometry of idealized serpentine minerals, $Mg_3Si_2O_5(OH)_4$, as well as to the chemical formula of antigorite adopted by Helgeson *et al*. (1978) and rewritten on the basis of five oxygen atoms for comparison, $Mg_{2.82}Si_{1.41}O_5(OH)_{3.65}$. Therefore, the thermodynamic data of Helgeson *et al*. (1978) were adopted in this study. Neglecting the significant SiO_2 contents, magnetite is closely represented by the chemical formula $(Fe^{2+}_{0.97}Mg_{0.08})$ $(Fe_{1.94}{}^{3+}Al_{0.02})O_4$, which does not depart significantly from the idealized stoichiometry $Fe^{2+}Fe_2{}^{3+}O_4$, whose thermodynamic data were adopted, following Helgeson *et al*. (1978).

The concentrations of trace elements in relevant minerals were acquired through LA-ICP-MS for metabasalts only (Table 4), as hydrochemical data indicate that local groundwaters interact chiefly with these rocks and less commonly with serpentinites. The main results are: (i) chlorite is rich in Mn (1000-1500 ppm), Zn (550-650 ppm) and V (200-300 ppm), relatively rich in Pb (70-90 ppm), Ba (55-70 ppm), Cr (55-70 ppm), Co (35-50 ppm), Ni (20-40 ppm), Rb (15-25 ppm) and Sr (10-15 ppm), whereas the concentrations of other relevant traces are below 10 ppm; (ii) actinolitic amphibole is rich in Cr (700-750 ppm), Mn (580-680 ppm) and V (250-290 ppm); it exhibits lower concentrations of Ni (23-26 ppm), Zn (17-22 ppm) and Co (17–18.5 ppm), whereas the contents of other analyzed traces are below 10 ppm; (iii) epidote is rich in Mn (1900-2200 ppm), Sr (550-600 ppm) and V (145-160 ppm); concentrations of Ni (55-70 ppm), Zn (50-55 ppm), Cr (25-40 ppm) and Co (12-18 ppm) are much lower, whereas the contents of other trace elements are < 10 ppm; (iv) albite is rich in Sr (850-1000 ppm), Fe (650-900 ppm) and Ba (230-320 ppm); it exhibits Rb contents of 15-30 ppm, while the other considered trace elements have concentrations lower than 10 ppm; (v) calcite is rich in Sr (1250-1450 ppm) and Fe (120-175 ppm) and has Mn contents of 25-35 ppm. Other relevant trace elements have concentrations lower than 10 ppm, apart from Cr, whose contents are below detection limit; (vi) phengite is rich in Ba (1200-1700 ppm), Mn (400-510 ppm), V (190-250 ppm), and Rb (170-205 ppm), relatively rich in Cr (45-65 ppm), Sr (35-50 ppm), and Zn (17-25 ppm), whereas the other analyzed trace elements have concentrations lower than 10 ppm.

Table 4. Concentrations of trace elements in primary minerals of metabasalt samples from the study area; data obtained through Laser Ablation ICP–MS analysis.

Mineral	V (mg/kg)	Cr (mg/kg)	Mn (mg/kg)	Co (mg/kg)	Cu (mg/kg)	Ni (mg/kg)	Zn (mg/kg)	As (mg/kg)	Sr (mg/kg)	Mo (mg/kg)	Cd (mg/kg)	Ba (mg/kg)	Pb (mg/kg)	U (mg/kg)
Calcite	< d.l.	< d.l.	33.1	< d.l.	20.1	< d.l.	13.8	< d.l.	1426	< d.l.	4.57	1.97	1.66	0.14
Calcite	< d.l.	< d.l.	27.3	0.37	5.87	< d.l.	< d.l.	< d.l.	1288	0.54	1.84	3.91	1.03	< d.l.
Amphibole	288	701	678	18.1	< d.l.	23.6	21.9	< d.l.	6.26	0.107	< d.l.	< d.l.	< d.l.	< d.l.
Amphibole	259	746	587	17.2	3	25.9	17.8	< d.l.	6.61	< d.l.	1.10	1.08	< d.l.	< d.l.
Epidote	157	26.2	2198	12.4	7.23	68.3	55	< d.l.	563	0.67	3.31	5.76	1.27	0.21
Epidote	145	38.2	1958	17.2	11.2	55.2	50.4	< d.l.	602	0.49	2.47	3.42	1.57	0.74
Albite	1.58	2.7	8.2	0.23	< d.l.	< d.l.	7.1	< d.l.	871	< d.l.	< d.l.	301	0.73	< d.l.
Albite	2.76	3.85	7.28	0.095	< d.l.	< d.l.	5.55	< d.l.	970	< d.l.	< d.l.	238	1.44	< d.l.
Phengite	199	48.7	502	1.13	< d.l.	0.66	17	< d.l.	48.2	< d.l.	< d.l.	1193	1.75	< d.l.
Phengite	235	61.8	428	2.1	< d.l.	1.56	24.3	< d.l.	39.5	< d.l.	< d.l.	1650	3.90	< d.l.
Chlorite	206	59.3	1163	38.7	< d.l.	35.9	573	< d.l.	11.2	< d.l.	< d.l.	56	87.3	1.32
Chlorite	268	69.8	1469	45.6	< d.l.	22.7	628	< d.l.	10.2	< d.l.	< d.l.	69	73.6	1.42

The chemical and mineralogical characteristics of samples coded A19 (metabasalt) and A10 (serpentinite) were evaluated in detail, as these two samples were selected and utilized to determine the kinetic parameters of metabasalt and serpentinite through dissolution experiments (see §2.3).

The same approach mentioned above was used to estimate the weight percentages of primary minerals and to determine their stoichiometry in both samples A19 and A10. Again, the computed oxide contents resulted to be in satisfactory agreement with the corresponding XRF analytical data (Table 5), suggesting that estimated weight percentages of primary minerals (also given in Table 5) have adequate precision for the aims of this study.

Table 5. Concentrations of major oxides in bulk rock samples of metabasalt (A19) and serpentinite (A10) from the study area. Data obtained from XRF analysis. Median concentrations in primary minerals and calculated weight percentages of primary minerals in the two bulk rocks are also reported.

Sample	Computed % of minerals in the bulk rock (wt.%)	SiO_2 (wt%)	Al_2O_3 (wt%)	Fe_2O_3 (wt%)	MgO (wt%)	CaO (wt%)	Na_2O (wt%)	K_2O (wt%)
Serpentinite-A10		38.12	0.67	8.95	38.75			
Antigorite, median	97.2	44.26	0.68	3.91	38.54			
Magnetite, median	2.8			100				
Computed serpentinite		41.87	0.65	9.10	36.46			
Metabasite_a19		44.27	12.31	13.75	11.24	8.21	3.43	
Epidote, median	9.0	41.28	23.79	13.37		21.57		
Albite, median	7.0	69.46	19.38				11.16	
Phengite, median	1.0	50.72	35.15	1.69	2.63	0	1.15	8.66
Actinolite, median	50.0	51.38	5.04	8.89	14.48	17.57	1.47	
Chlorite, median	32.0	32.62	20.64	24.91	21.67		0.15	
Calcite, median	1.0					56.03		
Computed metabasalt		44.85	13.17	13.89	14.21	11.37	1.46	0.08

The stoichiometries of epidote, calcite, and actinolite from all the analyzed metabasalt samples is in good agreement with the chemical formulae of these minerals from sample A1. Thus, these values have been adopted in calculations. In contrast, SEM–EDS data for chlorites from sample A19 (Table 5) suggest that its average stoichiometry is $Na_{0.05}Mg_{2.95}Fe_{1.71}Al_{2.22}Si_{2.97}O_{10.81}(OH)_8$.

SEM–EDS data for the solid phases of sample A10 (Table 5) indicate that the average chemical formula antigorite is $Mg_{2.72}Fe_{0.14}Al_{0.04}Si_{2.09}O_5(OH)_{4.34}$, whereas magnetite is well represented by the idealized stoichiometry $Fe^{2+}Fe_2^{3+}O_4$.

Measured rock compositions are also reported in Table 5 and are consistent with the chemical formulae $Si_1Ti_{0.037}Al_{0.329}Mg_{0.405}Fe_{0.223}Ca_{0.193}Na_{0.139}K_{0.0005}Mn_{0.003}O_{3.573}$ for the metabasalt sample A19 and $Mg_{1.298}Fe_{0.164}Ni_{0.01}Cr_{0.02}Si_1Al_{0.018}O_{2.669}(OH)_{1.884}$ for the serpentinite sample A10, both written on the basis of 1 Si atom.

2.3 Apparatus and analytical procedures of laboratory experiments for the determination of dissolution rates

The dissolution rates of the primary minerals of metabasalts and serpentinites have been investigated by means of laboratory experiments at the Lawrence Berkeley National Laboratory (LBNL) and at the Géosciences Environnement Toulouse (GET).

Experiments on the metabasalt sample A19 and the serpentinite sample A10 have been performed under known conditions of temperature, pH, and composition of inlet solutions by means of mixed flow reactor systems. A continuously-stirred mixed flow reactor (or flow-through reactor; Chou and Wollast, 1984) consists of a plastic reaction vessel of known volume, which is continuously stirred with a floating Teflon-coated magnetic stirrer (Pokrovsky *et al*., 2000). Stirring is controlled by a stirplate located directly beneath the bath (Fig. 4).

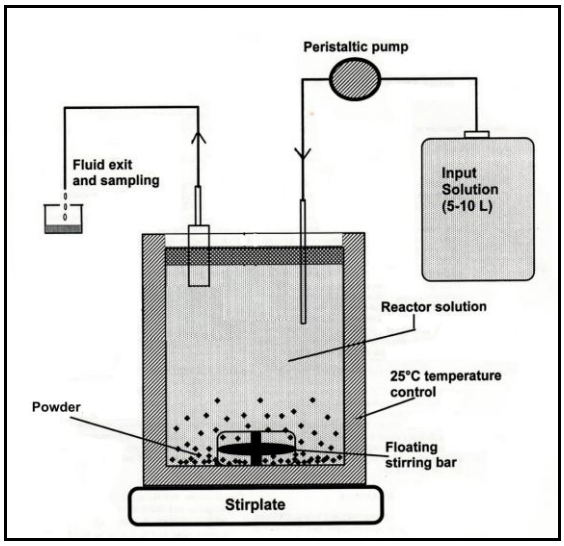

Fig. 4. Schematic setup of the mixed-flow reactor system (Pokrovsky *et al*., 2000; partially modified)

As described by Marini (2007), the input solution is continuously pumped through the reaction vessel at a constant flow rate, *Q*. The molal concentrations of some relevant solutes, produced by dissolution of the mineral phase, are monitored both in the inlet solution, m_{in}, and in the outlet solution, m_{out}. The dissolution experiment is run until m_{out} attains a constant value, or steady-state value, which is used to compute the steady-state dissolution rate through the equation:

$$r_{+} = \frac{Q \cdot (m_{out} - m_{in})}{\nu \cdot A_s \cdot M_s} \qquad (2)$$

where r_+ corresponds to the dissolution rate (mol/m^{2}s), A_s and M_s are the specific surface area (m^2/g) and the mass (g) of the dissolving solid phase and ν is the stoichiometric coefficient of the considered chemical element in the mineral.

If the inlet pH is significantly different from the outlet pH, the latter is considered to be representative of the system. Also in this case, variations of A_s and M_s during the dissolution run may determine significant uncertainties on the dissolution rates, which are usually computed with respect to the initial A_s and M_s due to unavailability of the final values of these parameters.

The continuous renewal of the aqueous phase in the reactor helps in maintaining the far-from-equilibrium conditions with the dissolving solid and avoiding precipitation of secondary solid phases.

The experiments were performed on the cleaned 80-150 µm size fraction. In detail, samples were initially ground using a jaw crusher and then an agate mortar and pestel. The finely grained materials were dry sieved to obtain the 80-150 µm size fraction. As suggest by Daval *et al*. (2010), the powders were ultrasonically cleaned in absolute ethanol for 10 minutes to remove fine particles. The cloudy supernatants were removed and replaced with fresh alcohol. This process was repeated at least five times or until the supernatants became clear. The powders were then rinsed with ultrapure water (resistivity ≥ 18.2 MΩ cm) for 5 minutes and oven-dried at 60 °C for several days. The efficacy of this procedure was monitored by scanning electron microscopy (SEM) which revealed that only a few fine particles were still adhering on the surface (Fig. 5).

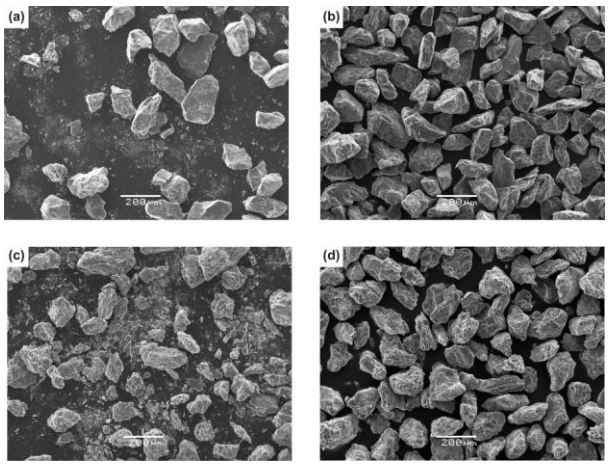

Fig. 5. SEM photomicrographs of the serpentinite sample A10 and the metabasalt sample A19. (a) The serpentinite and (c) the metabasalt before cleaning and (b) and (d) after they were ultrasonically cleaned in absolute ethanol. No fine particles are observed in (b) and (d).

The Brunauer-Emmett-Teller (BET) specific surface areas of the cleaned and dried 80-150 µm size fractions were determined to be 0.461 m^2g^{-1} for the metabasalt sample A19 and 17.04 m^2g^{-1} for the serpentinite sample A10, based on a 11 point krypton and nitrogen adsorption, respectively, using a Quantachrome Gas Sorption System located at the Géosciences Environnement Toulouse.

Steady-state dissolution experiments were performed at distinct solution pH values using a mixed-flow reaction vessel (see the above description) immersed in a water bath held at a constant temperature of 25 °C. Input fluids of ionic strength 0.01 mol/kg were prepared using deionized water and Merck reagent grade HCl, NaOH, $NaHCO_3$ and NaCl. They were stored in compressible polyethylene containers during the experiments and were injected into the reaction vessel using a Gilson peristaltic pump at constant flow rate, which was suitably selected from 0.017 to 0.44 mL/min. As described in Gudbrandsson *et al.* (2011), the reactors were cleaned thoroughly, assembled, and run for at least 24 h with deionized waters and then for other 24 h with the inlet solutions to rinse the tubing and to clean the reactors prior to each experiment. At the end of these cleaning cycles an outlet fluid sample was taken for chemical analyses.

In each dissolution experiment, an amount of rock powder weighted on an analytical balance (1.0 - 1.5 g of metabasalt and 0.5 - 1.5 g of serpentinite) was allowed to react in the stirred vessel with the fluid of fixed input composition.

The exit solutions were collected at regular intervals of time to ascertain the achievement of constant concentrations (i.e., steady state conditions). Outlet solutions were acidified with concentrated supra-pure HNO_3 prior to their analysis for Al, Ca, Fe, Cr and Mn by ICP-MS, Mg by AAS and Si by colorimetry. All chemical analyses were carried out in the laboratory of the GET.

2.4 Experimental determination of the release rates for the metabasalt

Four metabasalt dissolution experiments were carried out in this study at 25 °C and pH 2.0, 3.2, 7.2, and 12.0. The reactive fluid concentrations of Si, Mg, Ca, Al, Fe, K, Sr, Cr and Mn were regularly measured. These concentrations were used to calculate the rate of release of each element ($r_{i,BET}$) using the equation:

$$r_{i,BET} = \frac{Q \cdot m_{out}}{A_s \cdot M_s} \qquad (3)$$

where m_{out} represents the molal concentration of the *i*th element in the outlet fluid, Q designates the fluid flow rate, A_s and M_s refer to the specific surface area[2] and mass of the

[2] The surface area used in this study was obtained from BET analyses as described above (see §2.3).

solid in the reactor, respectively. It must be noted that the only differences between equation (3) and equation (2) are the absence, in equation (3) of both the stoichiometric coefficient of the *i*th element in the mineral phase of interest and the molal concentration of the *i*th element in the inlet fluid, which is zero in the experiments performed in this study.

Each dissolution experiment was run for a relatively long time, until attainment of steady-state conditions, as indicated by the temporal evolution of Si and Mg concentrations (Fig. 6).

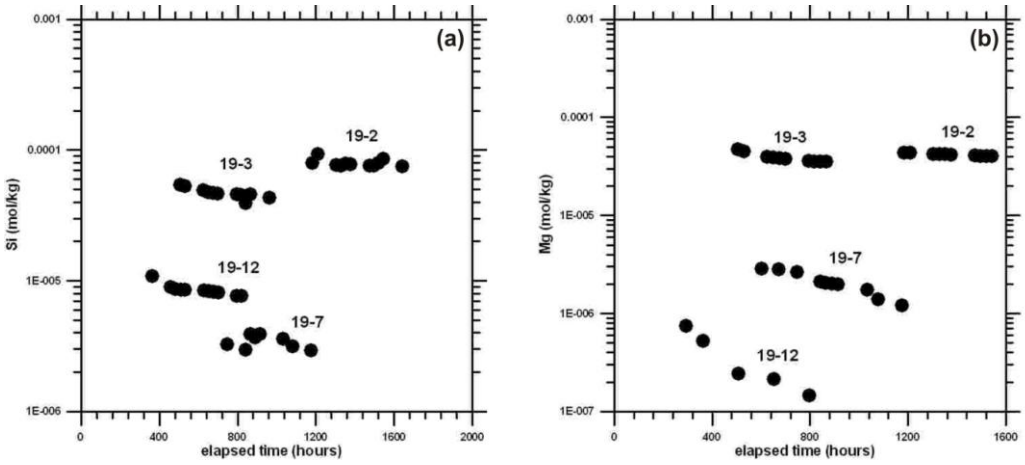

Fig. 6. (a) Si and (b) Mg concentration vs. elapsed time during each experiment of metabasalt dissolution.

All measured logarithms of the steady-state release rate of Si and Mg, log $r_{Si,\mathrm{BET}}$ and log $r_{Mg,\mathrm{BET}}$, are summarized in Table 6 and are shown as a function of pH in Fig. 7.

Table. 6 Results of metabasalt dissolution experiments.

Experiment	No.	pH[a]	Flow rate[a] (g/min)	Run time (h)	log $r_{Si,BET}$ (mol/cm^2/s)	log $r_{Mg,BET}$ (mol/cm^2/s)
A19-2		2.01	0.02	1709	-15.74	-16.01
A19-3		3.16	0.02	1130	-16.16	-16.25
A19-7		7.17	0.03	1175	-17.02	-17.25
A19-12		12.03	0.03	820	-16.63	-17.97

[a]Average value for all measured samples

Figure 7a shows that the logarithm of the steady-state release rate of Si exhibits a U-shaped variation with pH as it decreases with increasing pH at acidic condition but it increases

slightly with increasing pH at alkaline conditions. These results have been observed also in Gudbrandsson *et al.* (2011) on crystalline basalt and are in agreement with the characteristic dissolution behaviour exhibited by most aluminosilicates minerals. The dependence of logarithm of the steady-state release rate of Mg (Fig. 7b) on pH is not characterized by the typical U-shaped variation as the logarithm of the release rate decreases with increasing pH also under alkaline conditions, probably due to the precipitation of brucite. The possible occurrence of this process is suggested by speciation-saturation calculations carried out using PHREEQC and is in agreement with what has been observed by Pokrowsky and Schott (2004).

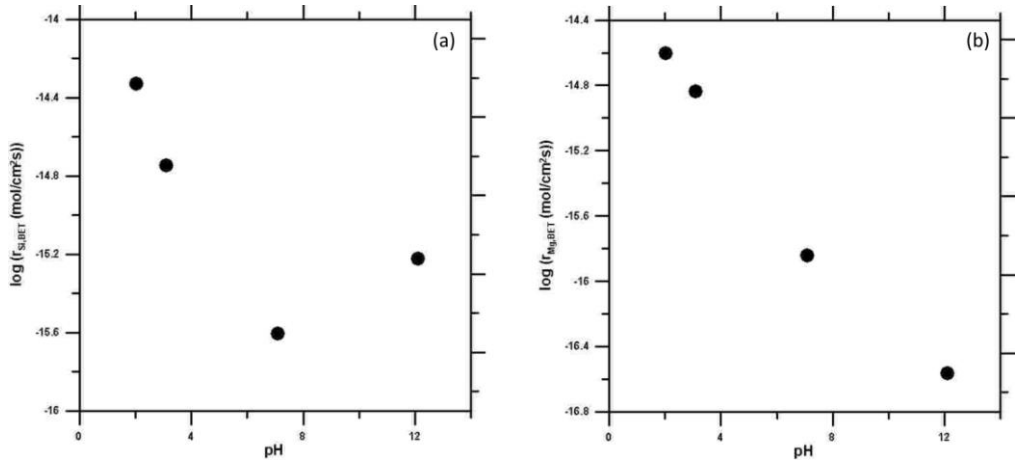

Fig. 7. Logarithms of the steady-state release rate of (a) Si and (b) Mg vs. pH for metabasalt at 25 °C.

2.5 Experimental determination of release rates for the serpentinite

Five serpentinite dissolution experiments were also performed in this study at 25 °C and pH 2.0, 3.1, 5.8, 7.3, and 8.9. Again, the reactive fluid concentrations of Si, Mg, Ca, Al, Fe, K, Sr, Cr and Mn were regularly measured in order to calculate the rate of release of each element by means of equation (3). As for metabasalt dissolution experiments, attainment of steady-state conditions required a comparatively long time, as shown in Fig. 8.

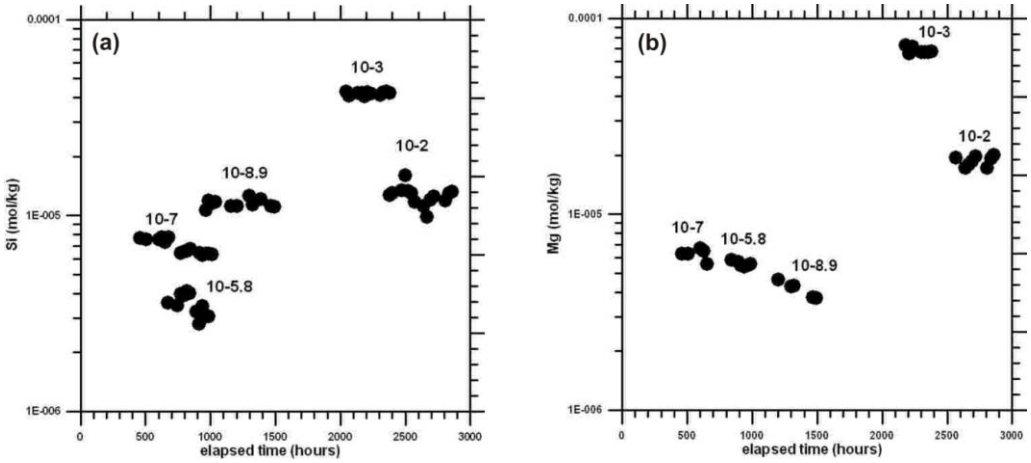

Fig. 8. (a) Si and (b) Mg concentration vs. elapsed time during each experiment of serpentinite dissolution.

All obtained logarithms of the steady-state release rate of Si and Mg, $r_{Si,BET}$ and $r_{Mg,BET}$, are given in Table 7.

Table. 7 Results of serpentinite dissolution experiments.

Experiment	No.	pH[a]	Flow rate[a] (g/min)	Run time (h)	log $r_{Si,BET}$ (mol/cm^2/s)	log $r_{Mg,BET}$ (mol/cm^2/s)
A10-2		2.02	0.44	2856	-15.27	-15.25
A10-3		3.06	0.18	2565	-15.38	-15.35
A10-6		5.76	0.19	984	-16.47	-16.44
A10-7		7.28	0.03	1010	-17.17	-17.46
A10-8.9		8.89	0.03	1466	-16.90	-17.27

[a]Average value for all measured samples

The logarithms of the release rates (Fig. 9), generated from Si and Mg outlet concentrations, are characterized by a significant decrease from acidic conditions to pH 7 and by a subsequent increase in weakly alkaline solutions.

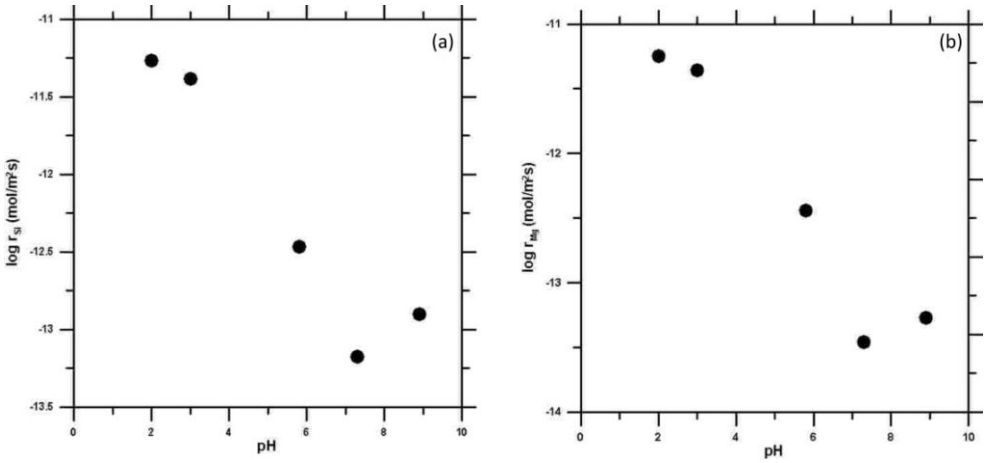

Fig. 9. Logarithms of the steady-state release rate of (a) Si and (b) Mg vs. pH for antigorite at 25 °C.

Incidentally, taking into account that both Mg and Si released by this lithotype come only from antigorite destruction (see Tab. 5 in §2.2), the release rates of Mg and Si and the dissolution rates of antigorite differ by the stoichiometric coefficient of Mg and Si in antigorite. In principle, the calculation of the dissolution rate of antigorite is a very simple matter. In practice, things might be complicated by occurrence of non-stoichiometric dissolution.

Therefore, the Mg/Si ratio in the outlet solution has been monitored. It has been observed that at pH values of 2 and 3 antigorite dissolution is stoichiometric and the measured Mg/Si molal ratio in the aqueous solution is close to antigorite stoichiometry (ν_{Mg}/ν_{Si} is 1.5 in idealized serpentine minerals and 1.42 in antigorite from the study area) but it increases at pH 5.8 and it significantly decreases at pH 7.3 and 8.9, indicating occurrence of nonstoichiometric dissolution. In particular, at pH 8.9 it was observed a preferential release of Si with respect to that of Mg (Fig. 10a) which leads to the formation of a Mg-rich surface layer. The formation of this layer was confirmed by decreasing the pH of the inlet solution from 8.9 to 2, which resulted in a sharp increase in the Mg/Si ratio of the outlet solution, owing to dissolution of the Mg-rich surface layer. This interpretation is in agreement with the pH dependence of the dissolution rates and surface speciation of brucite and quartz, as discussed by Schott *et al.* (2009) and shown in Fig. 10b.

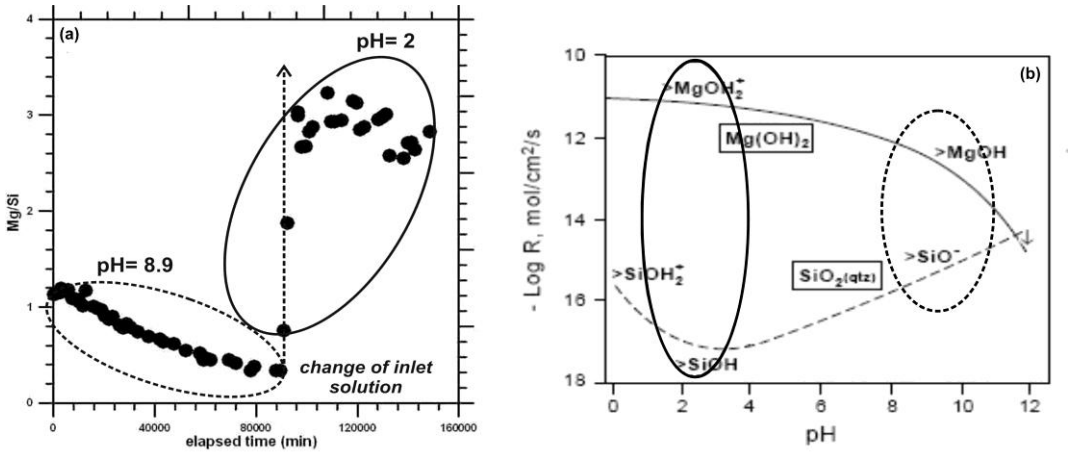

Fig. 10. (a) Mg/Si ratio vs. elapsed time (min) during dissolution of serpentinite at pH 8.9 and 2; (b) pH dependence of the dissolution rates and surface speciation of brucite and quartz (Schott *et al.*, 2009; partially modified).

2.6 Calculation of the dissolution rates and kinetic parameters of individual minerals

To calculate the dissolution rates and kinetic parameters of individual minerals, first individual mineral surface areas were estimated by distributing the total crushed-rock BET surface area among the different minerals present in the metabasalt (chlorite, amphibole, epidote, albite, and phengite) and in the serpentinite (antigorite and magnetite) as a function of their mass fraction.

To help data interpretation, the experimental molar concentration of each element of interest was compared with the corresponding theoretical counterpart. The needed equation to compute the expected concentration in the reactor was obtained from the following mass balance which applies to the continuously-stirred reaction vessel (from Leib *et al.*, 2008, modified) :

$$C_{i,t+dt} \cdot V = C_{i,t} \cdot V + C_{i,in} \cdot Q_{in} \cdot dt - C_{i,out} \cdot Q_{out} \cdot dt + \sum_j \nu_{i,j} \cdot r_{+,j} \cdot A_{S,j} \cdot M_{S,j} \cdot dt \qquad (4)$$

where t is time (s), dt is the time variation (s), $C_{i,t+dt}$ is the molar concentration of the i-th element in the reactor at time $t+dt$ (mol/L), $C_{i,t}$ is the molar concentration of the i-th element in the reactor at time t (mol/L), V is the reactor volume (L), $C_{i,in}$ is the molar concentration of the i-th element in the inlet solution (mol/L), which is zero in our case, C_{out} is the molar concentration of the i-th element in the outlet solution (mol/L), Q_{in} and

Q_{out} are the inlet and outlet flow rate (L/s), respectively, which are equal in our case, $\nu_{i,j}$ is the stoichiometric coefficient (adimensional) of the *i*-th element in the *j*-th dissolving solid phase, $r_{+,j}$ is its dissolution rate (mol m^{-2} s^{-1}), $A_{S,j}$ and $M_{S,j}$ are the specific surface area (m^2/g) and the mass of the *j*-th dissolving solid phase (g), respectively.

Dividing both sides of equation (4) by the reactor volume, *V*, it can be rewritten as:

$$C_{i,t+dt} = C_{i,t} + \frac{Q \cdot (C_{i,in} - C_{i,out}) + \sum_j \nu_{i,j} \cdot r_{+,j} \cdot A_{S,j} \cdot M_{S,j}}{V} \cdot dt \qquad (5)$$

which is the relation we are looking for. It allows, in fact, the calculation of the concentration of the element of interest in the reactor as a function of time.

Incidentally, considering that $C_{i,t+dt} - C_{i,t} = dC_i$, equation (5) can be rearranged as follows:

$$\frac{dC_i}{dt} = \frac{Q \cdot (C_{i,in} - C_{i,out}) + \sum_j \nu_{i,j} \cdot r_{+,j} \cdot A_{S,j} \cdot M_{S,j}}{V} \qquad (6)$$

It must be noted that at steady-state, dC_i/dt=0 and equation (6) can be solved with respect to $r_{+,j}$ obtaining an expression corresponding to equation (2), apart from a small difference in the concentration unit and the involvement of several dissolving solid phases instead of a single phase.

Two different approaches were used to retrieve the dissolution rates of each distinct mineral, based on the dissolution experiments discussed in §2.4 and §2.5 for the metabasalt and the serpentinite, respectively.

In the first approach, rates were taken from the geochemical literature (Table 8) referring to the compilations and critical reviews (e.g., White and Brantley, 1995; Palandri and Kharaka, 2004; Marini, 2007) of several laboratory dissolution experiments, including those of: (i) Hellmann (1994), Chou and Wollast (1984), Knauss and Wolery (1986), Knauss and Kopenhaver (1995), Stillings and Brantley (1995) and Chen and Brantley (1997) for Na-rich plagioclases; (ii) Ross (1967), Kodama and Schnitzer (1973), Malmström *et al*. (1996), Hamer *et al*. (2003) and Lowson *et al*. (2005, 2007) for chlorite; (iii) Nickel (1973), Lin and Clemency (1981), Knauss and Wolery (1989), Kalinowski and Schweda (1996) and Oelkers *et al.* (2008) for white micas; (iv) Nickel (1973), Rose (1991)

and Kalinowski *et al.* (1998) for epidote; (v) Schott *et al.* (1981), Mast and Drever (1987), Chen and Brantley (1998) for amphibole and (vi) Luce *et al.* (1972), Lin and Clemency (1981), Bales and Morgan (1985), Cipolli *et al*., (2004), Orlando *et al.* (2011) for serpentine minerals. It must be underscored that all these rates were obtained on single (separate) minerals.

Table 8. Kinetic parameters for the solid phases of interest from the geochemical literature.

Mineral	$\log k_{+,H+}$ ($\log(\text{mole m}^{-2}\text{s}^{-1})$)	$-N_{+,H+}$	$\log k_{+,H2O}$ ($\log(\text{mole m}^{-2}\text{s}^{-1})$)	$\log k_{+,OH-}$ or $\log k_{+,CO2}$ ($\log(\text{mole m}^{-2}\text{s}^{-1})$)	$-N_{+,OH-}$	$E_{+,H+}$ (kJ mol^{-1})	$E_{+,H2O}$ (kJ mol^{-1})	E_{+,OH^-} or $E_{+,CO2}$ (kJ mol^{-1})
Amphibole	-8.40	0.700	-10.60			18.9	94.4	
Epidote	-10.60	0.338	-11.99	-17.33	-0.556	71.7	70.7	79.1
Albite	-9.87	0.457	-12.04	-16.98	-0.572	65.0	69.8	71.0
Phengite	-11.85	0.370	-13.55	-14.55	0.220	22.0	22.0	22.0
Chlorite	-9.79	0.490	-13.00	-16.79	-0.430	88.0	88.0	88.0
Calcite	-0.30	1.000	-5.81	-3.48	1.000	14.4	23.5	35.4
Antigorite	-5.70	0.800	-12.40			75.5	56.6	
Magnetite	-8.59	0.279	-10.78			18.6	18.6	

The temporal evolution of the concentration of solutes of interest in the reaction vessel was then computed as a function of time using equation (5) and adopting the dissolution rates of each mineral phase from the literature (Table 8). Calculated and experimental Si concentrations during metabasalt dissolution at pH 2 and 7 are shown in Fig. 11. Computed and experimental concentrations of Si, Al, Mg, and Fe at steady-state during metabasalt dissolution at pH 2 and 7 are reported in Table 9.

Due to the differences between calculated and analytical concentrations observed both in Fig. 11 and Table 9, it is evident that adoption of literature rates does not allow to reproduce the experimental data measured in this study.

Table 9. Average solute concentrations measured (at steady-state conditions) and calculated for the experiments on metabasalt at pH 2 and 7.

pH	Si mes	Si calc	Al mes	Al calc	Mg mes	Mg calc	Fe mes	Fe calc
	ppm	ppm	ppm	ppm	ppm	ppm	ppm	ppm
2	2.180	1.043	0.968	0.683	0.990	0.763	1.146	0.463
7	0.096	0.019	0.006	0.011	0.043	0.004	n.d	n.d

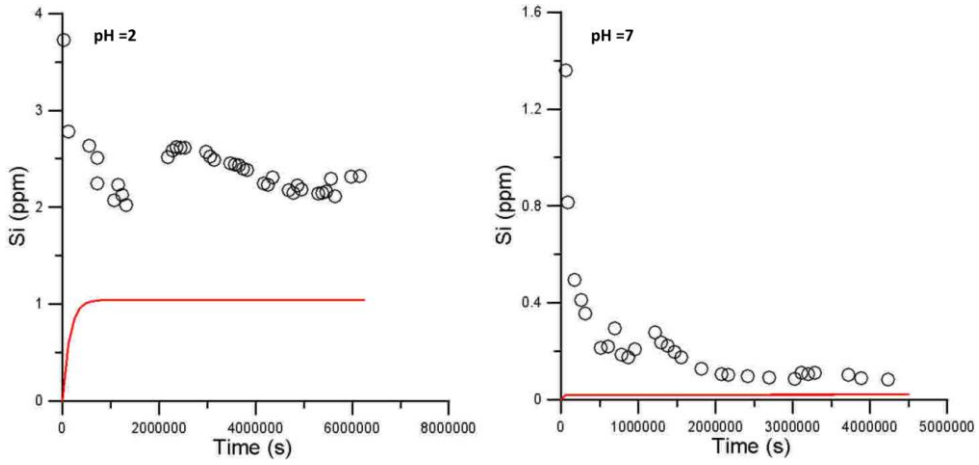

Fig. 11. Time evolution of Si concentration for the experiments on metabasalt at pH 2 and 7. The solid line represents the Si concentrations calculated adopting the literature rates.

In the second approach, first the dissolution rate of the rock ($r_{+,rock}$) was calculated inserting the experimental data in equation (2). Afterwards, the dissolution rate of each mineral ($r_{+,min}$) was computed referring to the stoichiometry of the rock (see §3.2) and of the minerals (see §3.2) through the equation:

$$r_{+,min} = \frac{\nu_{i,rock}}{\nu_{i,min}} \cdot r_{+,rock} \qquad (7)$$

where $\nu_{i,rock}$ and $\nu_{i,min}$ are the stoichiometric coefficients of the *i*-th element in the rock and in the mineral, respectively. Then, equation (5) was used to calculate the concentration of the element of interest in the reactor as a function of time, inserting the dissolution rates obtained using equation (7).

It turned out that the second (stoichiometric) approach allows to reproduce satisfactorily the analytical data at steady state. In particular, analytical silicon and aluminium at steady-state (at pH 2, 3, 7 and 12) for metabasalt experiments, are nicely fitted (Fig. 12) and the deviations of calculated data from analytical data is better than 3% (Tab. 10).

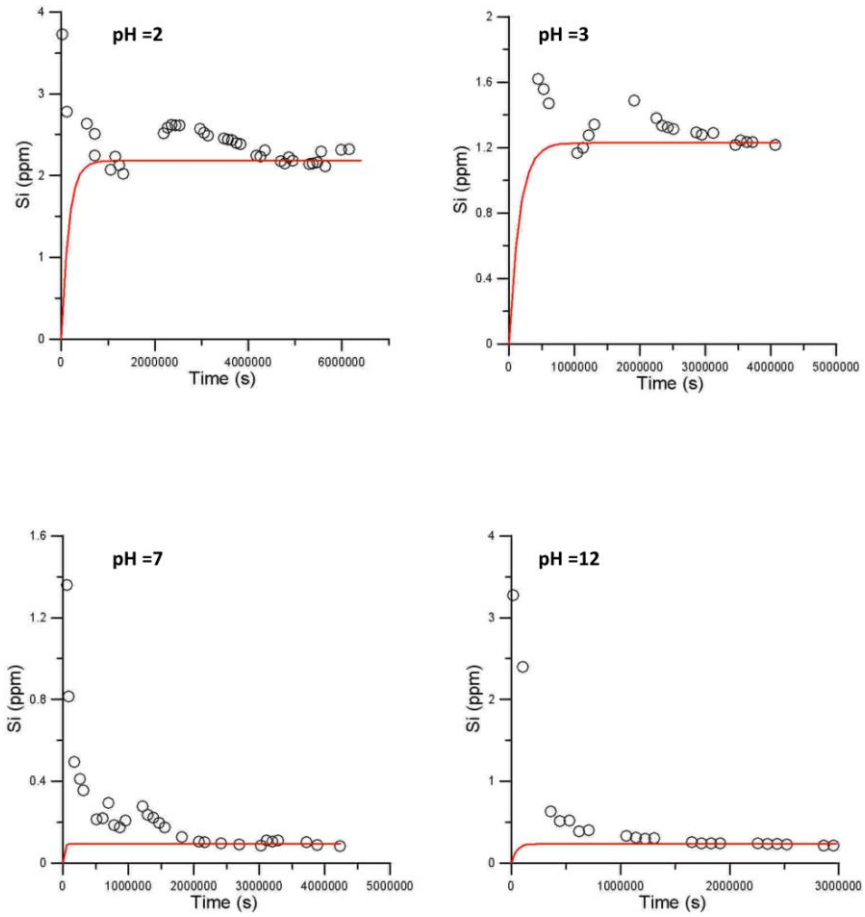

Fig. 12. Time evolution of Si concentration for the experiments on metabasalt at pHs 2, 3, 7 and 12. The solid line represents the Si concentrations calculated by adopting the second (stoichiometric) approach.

Table 10. Average solute concentrations measured (at steady-state conditions) and calculated for the experiments on metabasalt at pH 2, 3, 7 and 12.

pH	Si mes ppm	Si calc ppm	Al mes ppm	Al calc ppm	Mg mes ppm	Mg calc ppm	Fe mes ppm	Fe calc ppm
2	2.180	1.043	0.968	0.683	0.990	0.763	1.146	0.463
3								
7	0.096	0.019	0.006	0.011	0.043	0.004	n.d	n.d
12								

The same approach has been applied to the serpentinite experiments and again, it was possible to reproduce adequately the analytical data as shown in Table 11 and Figure 13.

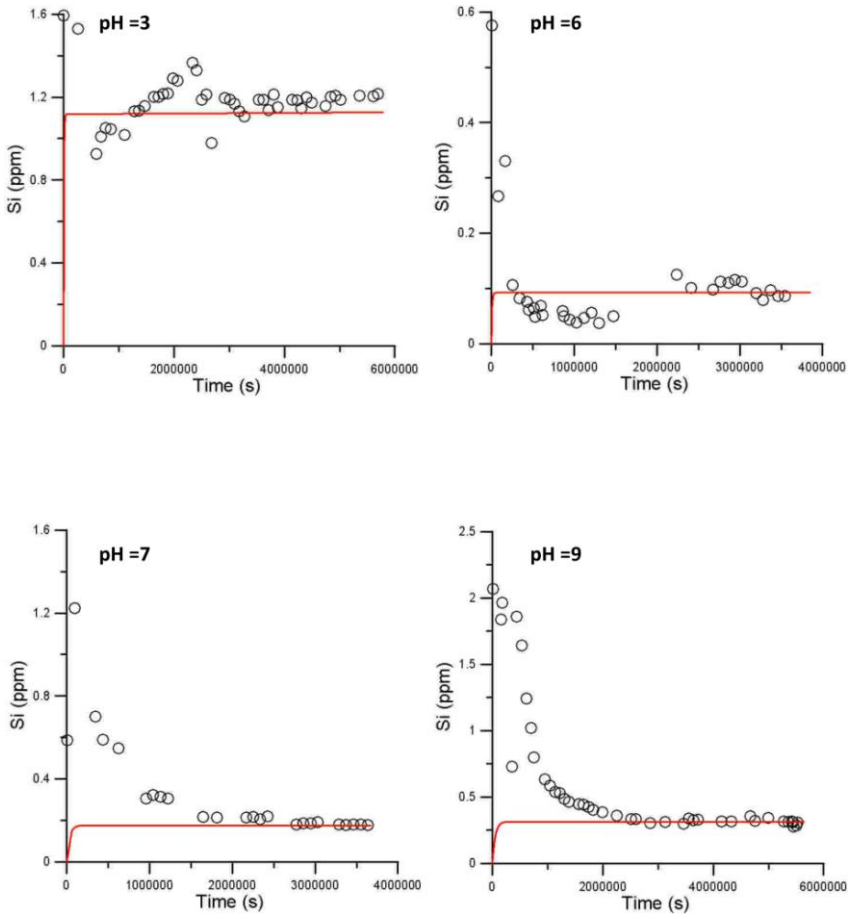

Fig. 13. Time evolution of Si concentration for the experiments on serpentinites at pH 2, 3, 7 and 9. The solid line represents the Si concentrations calculated by adopting the second (stoichiometric) approach.

Table 11. Average solute concentrations measured (at steady-state conditions) and calculated for the experiments on serpentinites at pH 2, 3, 7 and 9.

pH	Si mes	Si calc	Mg mes	Mg calc	Fe mes	Fe calc
	ppm	ppm	ppm	ppm	ppm	ppm
2.0	0.336	0.314	0.456	0.427	0.062	0.061
3.1	1.183	1.118	1.646	1.557	0.116	0.131
5.8	0.092	0.099	0.136	0.127	n.d	n.d
7.3	0.183	0.174	0.126	0.121	n.d	n.d
8.9	0.328	0.313	0.180	0.182	n.d	n.d

It is instructive to compare the dissolution rates of each mineral (at pH 2) retrieved, by means of the stoichiometric approach, from the whole-rocks dissolution experiments carried out in this study with those obtained through previous dissolution experiments on

single (separate) minerals as reported in the geochemical literature (Tables 12 and 13 for metabasalt and serpentinite, respectively).

Table 12. Comparison between the literature dissolution rates of each mineral (pH 2) and those retrieved by means of the stoichiometric approach applied on the results of the dissolution experiments of metabasalt.

	pH	Amphibole	Epidote	Albite	Phengite	Chlorite
		log R_{Si} (mol/m^2s)	log R_{Si} (mol/m^2s)	log R_{Si} (mol/m^2s)	log R_{Si} (mol/m^2s)	log R_{Si} (mol/m^2s)
Experimental results	2	6.628E-12	1.494E-11	1.604E-11	1.499E-11	1.618E-11
Literature data	2	1.836E-10	6.320E-12	1.736E-11	2.852E-13	1.708E-11

Table 13. Comparison between the literature dissolution rates of each minerals (pH 2) and those retrieved by means of the stoichiometric approach applied on the results of the dissolution experiments of serpentinite.

	pH	Antigorite	Magnetite
		log R_{Si} (mol/m^2s)	log R_{Fe} (mol/m^2s)
Experimental results	2	6.628E-12	3.143E-13
Literature data	2	1.836E-10	2.852E-13

Table 12 shows that there is a good agreement between the literature dissolution rate of albite (which is one of the most studied minerals in terms of dissolution kinetics) and chlorite and the rates for these two minerals obtained in this study based on the results of the dissolution experiments of metabasalt adopting the stoichiometric approach. On the other hand, the dissolution rates retrieved for the other solid phases (amphibole, epidote, and phengite) are in contrast with those reported in literature by 1-2 orders of magnitude, although there are also strong differences among the amphibole rates from previous studies.

A similar result has been observed for the serpentinite as antigorite has a dissolution rate which is two orders of magnitude lower than that of previous investigations.

The logarithm of the rates of each mineral obtained from whole-rock dissolution experiments are now reported as a function of pH to retrieve the rate and the order of reaction for the acidic, neutral and basic dissolution mechanisms, to be used at a later stage for the geochemical modeling of water-rock interaction (§3.7). A trial-and-error procedure was adopted until an acceptable fit of the experimental data was achieved.

In particular, the data for the metabasalt minerals are shown in Fig. 14, where:

(i) the black line refers to the starting point, that is a third-order polynomial, fitting all the rates at pH 2, 3, 7 and 12, and extrapolated to compute the rate at pH 14;

(ii) the red and light blue lines represent the computed acidic and basic dissolution mechanisms;

(iii) the purple line represents the final result, that is the sum of the contributions of the acidic, neutral and basic dissolution mechanisms.

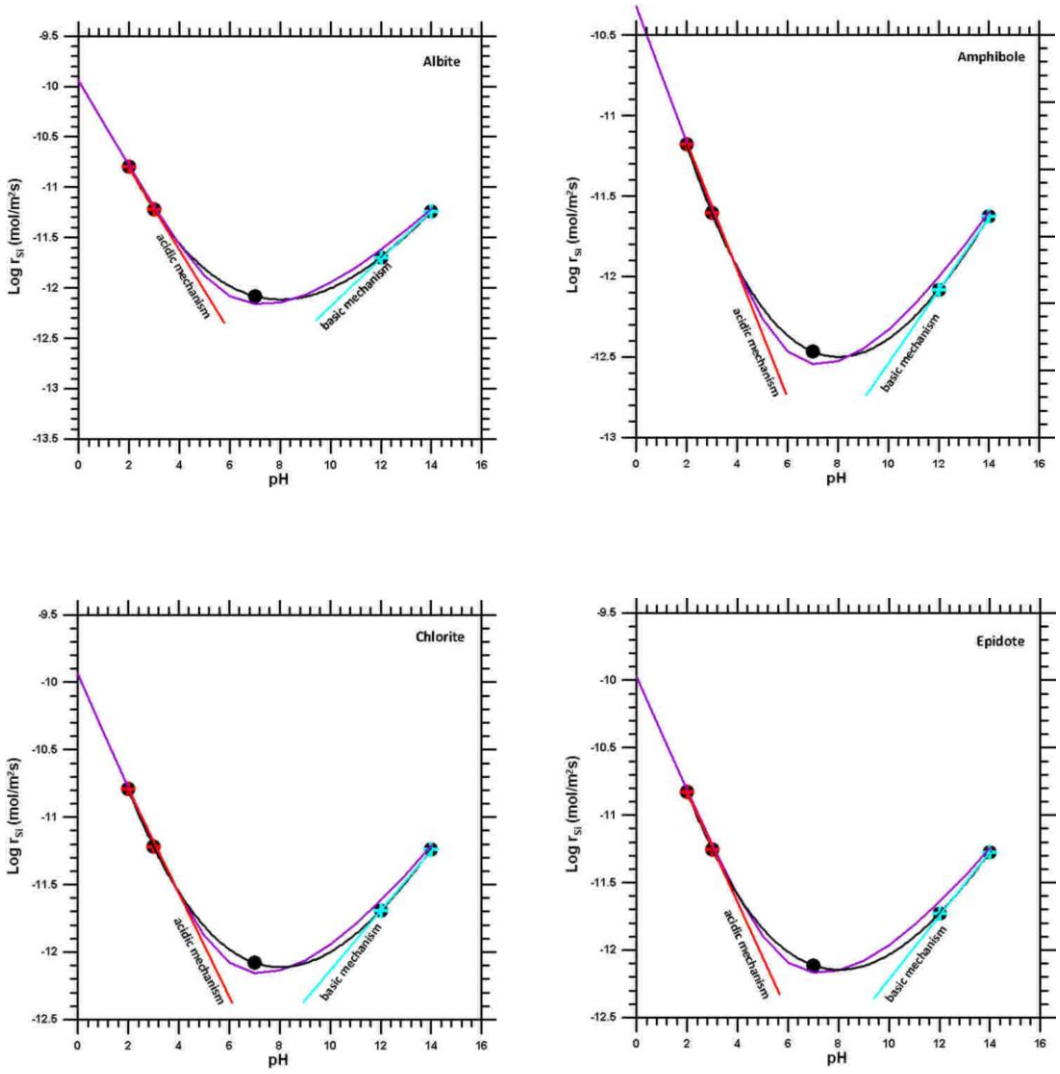

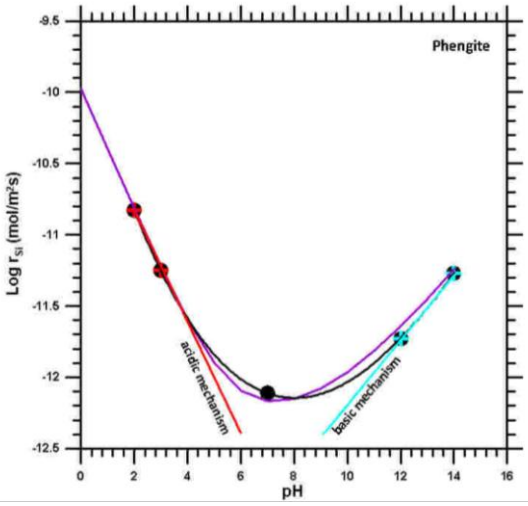

Fig. 14. Initial fitting of the available log-rates (black circles) by means of a third-order polynomial (black line, extrapolated to compute the log-rate at pH 14) and obtained results for the acidic mechanism (red line), the basic mechanism (pale blue line) and the overall dissolution log-rate as a function of pH (violet line) for albite, amphibole, chlorite, epidote and phengite in the metabasalt.

For each mechanism, we got a straight-line equation whose slope is the order of reaction and whose intercept is the log-rate at pH = 0 (Table 14).

Table 14. Kinetic parameters for the solid phases of interest retrieved from the whole-rock dissolution experiments on metabasalt.

Mineral	log $k_{+,H+}$ (log(mole $m^{-2}s^{-1}$))	$-N_{+,H+}$	log $k_{+,H2O}$ (log(mole $m^{-2}s^{-1}$))	log $k_{+,OH-}$ (log(mole $m^{-2}s^{-1}$))	$-N_{+,OH-}$
Amphibole	-10.33	0.427	-12.75	-14.81	-0.227
Epidote	-9.97	0.427	-12.36	-14.46	-0.227
Albite	-9.94	0.427	-12.37	-14.43	-0.227
Phengite	-9.97	0.427	-12.36	-14.46	-0.227
Chlorite	-9.94	0.427	-12.37	-14.42	-0.227

With regard to the serpentinite, two distinct attempts have been done to constrain the neutral and basic mechanisms for antigorite. The first attempt is an exercise of best fitting of measured log-rates which results in the virtual absence of the neutral mechanism and in a basic mechanism characterized by a very high slope and a high log-rate at pH 14 (see purple line in Fig. 15a). This is in contrast with what was observed by Bales and Morgan (1985) who found a nearly flat horizontal trend in the basic field (Fig. 15b).

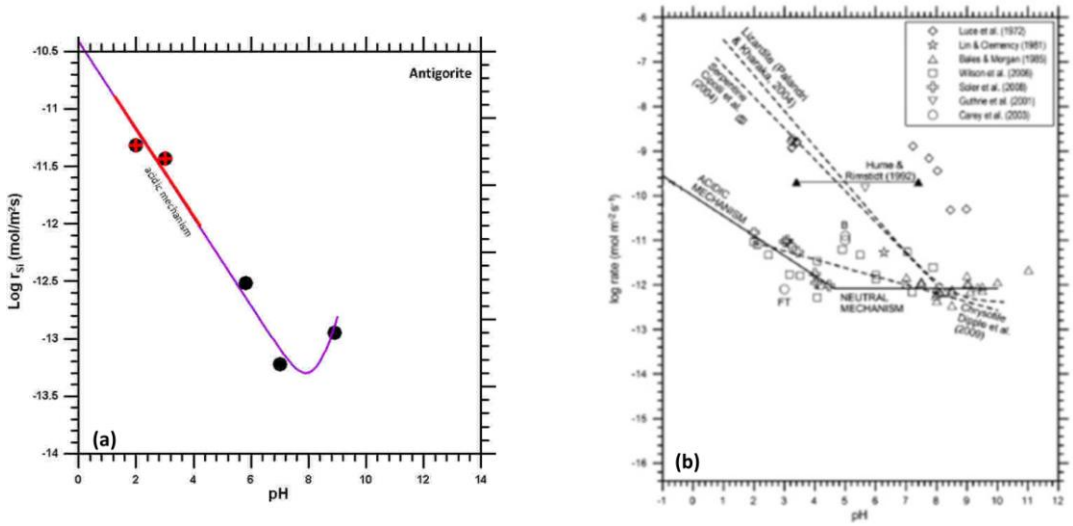

Fig. 15. (a) Best fitting of the available rates (black circles) for antigorite by means of a third-order polynomial (violet line); the acidic mechanism is also shown (red line); (b) plot of the logarithm of the dissolution rate of serpentine minerals vs. pH showing the available data at 25°C (Orlando *et al*., 2011; partially modified).

In the second attempt, the same acidic mechanism of the previous interpretation (red line in Fig. 16) was assumed together with a neutral mechanism characterized by a log-rate of -13.4 [in units of log (mol m^{-2} s^{-2})], thus obtaining an overall dissolution log-rate as a function of pH which interpolates the two values at pH 7 and 9 (purple line in Fig. 16). This outcome is in agreement with what was shown by Bales and Morgan (1985) and with the interpretation of Orlando *et al.* (2011) (Fig. 15b) and was adopted (Table 15).

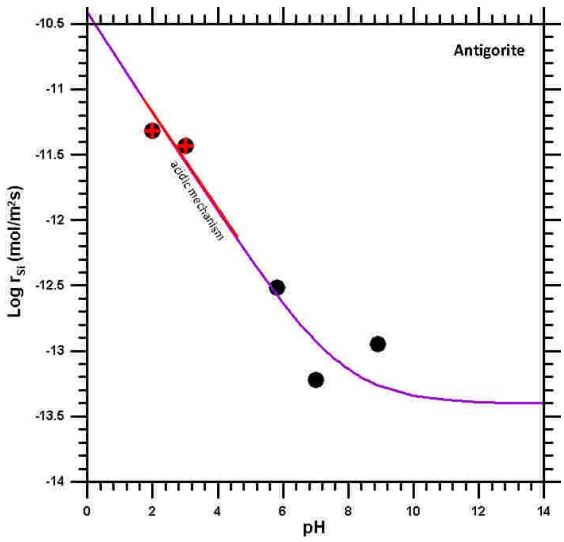

Fig. 16. Alternative fitting of the available rates (black circles) for antigorite assuming the same acidic mechanism of Fig. 16 (red line) and a neutral mechanism characterized by a log-rate of -13.4 [in units of log (mol m^{-2} s^{-2})] in agreement with Bales and Morgan (1985).

Table 15. Kinetic parameters for the solid phases of interest retrieved from the whole-rock dissolution experiments on serpentinite (second attempt).

Mineral	$\log k_{+,H+}$ ($\log(\text{mole } m^{-2} s^{-1})$)	$-N_{+,H+}$	$\log k_{+,H2O}$ ($\log(\text{mole } m^{-2} s^{-1})$)
Antigorite	-10.41	0.384	-13.40

Chapter 3: Geochemical modeling

3.1 Theoretical background

The fate of the chemical constituents during weathering is a complex topic that can be elucidated by means of the geochemical modeling, or more precisely the reaction path modeling, of water-rock interaction. This exercise provides a significant contribution to define the geochemical baselines of natural waters (e.g., Cidu *et al.*, 2008).

Reaction path modeling is a powerful geochemical tool, formulated in the late 1960s by Helgeson (1968; 1979), who developed the equations required to describe the irreversible mass exchanges between the aqueous solution, a gas phase (if any), and one or more solid phases. Helgeson and coworkers also presented several applications of reaction path modeling (e.g., Helgeson *et al.*, 1969; 1970).

Reaction path modeling can be applied to reproduce the progressive dissolution of one or more mineral phases in an aqueous solution, the mixing of two solutions and the heating or cooling of an aqueous solution.

In the last 1960s, Helgeson introduced the first computer program, called PATHI, for performing reaction path calculations in geochemical systems (Helgeson, 1968; Helgeson *et al*., 1970). Nowadays, this code has been superseded by other programs such as the EQ3/6 software package (Wolery, 1979, 1992; Wolery and Daveler, 1992; Wolery and Jarek, 2003), which can be run on a laptop and used to investigate the fate of the chemical constituents of interest during weathering. In order to constrain the modeling exercise, it is necessary to provide some input parameters, such as the composition and abundance of each mineral of interest, the initial composition of the aqueous solution (before the beginning water-rock interaction), relevant thermodynamic and kinetic data, etc.

In this study, the most recent release of the software package EQ3/6, version 8.0 (Wolery and Jarek, 2003), was used to simulate the progressive dissolution of metabasalts and serpentinites of the Northern Calabria (Italy) in meteoric waters, thus simulating the weathering processes occurring in these shallow ophiolitic aquifers. Reaction path has been modeled in kinetic (time) mode, under closed system with a defined set of secondary solid phases, which are allowed to precipitate, and open system with CO_2. An updated version of the thermodynamic database data0.ymp.R5, whose characteristics are described by Wolery and Jove-Colon (2007), was used (see also Apollaro *et al.*, 2013 a, b).

3.1.1 The boundary conditions

Simulations were carried at constant temperature of 11.4 °C, which reproduces the average temperature of local groundwaters. Fugacity of CO_2 was fixed, in different runs, at either $10^{-2.5}$ bar (mean value), $10^{-1.9}$ bar (mean value + 1σ), or $10^{-2.9}$ bar (mean value – 1σ). Fixing these f_{CO2} values corresponds to hypothesize open-system conditions with respect to CO_2. In other words, it is assumed that the considered system is connected to an external gas reservoir, which keeps f_{CO2} constant at the specified value (Wolery and Jarek, 2003). This is consistent with the continuous supply of CO_2 from the soil to the aqueous system. In contrast, no constraint was imposed on f_{O2}, which is calculated by the EQ6 code and which results from the balance of divalent and trivalent Fe which are supplied to aqueous solution through gradual dissolution of either (i) Fe(II)-bearing amphibole and chlorite, Fe(III)-containing epidote, and Fe(II)-Fe(III)-bearing phengite, in the case of metabasalt, or (ii) Fe(II)-Fe(III)-bearing magnetite in the serpentinite runs.

3.1.2 Composition of initial solution

The chemical composition of the initial aqueous solution has been taken from Apollaro *et al.* (2011). It was fixed adopting the average contents of the four immature samples, which are characterized by low alkalinity (13-27 mg HCO_3/L), low concentration of dissolved constituents and strong undersaturation with calcite. The chemical composition of the initial aqueous solution adopted in geochemical modeling is reported in Table 16.

Table 16. Chemical composition of the initial aqueous solution used in the simulations. Concentrations of chemical components are indicated by the chemical symbol of the corresponding "basis species" of EQ3/6.

Dissolved components	Total concentration (mg/L)
Ca^{2+}	3.9
Mg^{2+}	0.8
Na^{+}	2.2
K^{+}	0.6
HCO_3^{-}	21.2
SO_4^{2-}	2.5
$SiO_{2(aq)}$	7.9
Fe^{2+}	3.0E-04
Mn^{2+}	2.5E-03
Zn^{2+}	1.3E-02
Pb^{2+}	1.5E-04
Cu^{2+}	3.0E-04
Co^{2+}	2.2E-04
Ni^{2+}	2.9E-04
CrO_4^{2-}	3.6E-04
MoO_4^{2-}	5.8E-04
$H_2AsO_4^{-}$	3.6E-04
Sr^{2+}	1.4E-02
Ba^{2+}	5.6E-03
VO^{2+}	9.9E-04
Rb^{+}	2.3E-05
UO_2^{2+}	5.7E-06

3.1.3 The solid reactants

The solid reactants considered to model the dissolution of average metabasalt are (in order of decreasing importance) calcite, amphibole, epidote, albite, chlorite and phengite, whereas those considered to simulate the dissolution of mean serpentinite are antigorite and magnetite.

Both the kinetic parameters (Tables 8, 14 and 15) and the surface areas of each solid reactant were specified to carry out the reaction path modeling in time mode.

Reactive surface areas of primary minerals are one the most difficult variables to be evaluated and their estimates are considered little more than educated guesses by several authors (e.g., Appelo and Postma, 1996; Marini *et al.*, 2000). This high uncertainty on total reactive surface area causes a correspondingly large error on time (in fact, an hyperbolic relation exists between the surface area and time corresponding to an inverse linear dependence between the logarithm of the surface area and the logarithm of time; see §7.2.4 in Marini, 2007), whereas these uncertainties have no effects on the results of reaction path

modeling as a function of the reaction progress variable. In other words, a time-mode simulation was performed to obtain a reliable stoichiometric mode model.

Consequently, initial surface areas (cm^2) of primary minerals were computed starting from their weight percentages, adopting a simple geometrical model involving the shape and size of mineral grains and the effective intergranular porosity (see §7.2.4 in Marini, 2007). First, assuming a spherical geometry for the solid particles, a value of 0.05 cm for the average diameter of grains, and an effective intergranular porosity of 0.3, a total volume of 2333 cm^3 and a total surface area of 140,000 cm^2 were calculated for all the solid particles in contact with 1000 g of water, irrespective of their mineralogy. Then, total volume and total surface area were partitioned into the different minerals as a function of volume percentages. Molecular weights (g/mole) and molar volumes (cm^3/mole) were finally used to compute the mass and the weight percentage of each solid phase. Results are listed in Table 17.

Table 17. Geometrical surface areas and masses of solid phases of interest derived from modal abundances (vol.%), based on a geometric model that includes the shape and size of mineral grains and the effective intergranular porosity.

Rock	Mineral	Vol%	Initial surface area (cm^2)	Molar volume (cm^3/mole)	Mass (mole)	MW (g/mole)	Wt%
Metabasalt	Epidote	23	32200	139.20	3.86	483.223	26.18
Metabasalt	Albite	16	22400	100.25	3.72	262.223	13.72
Metabasalt	Phengite	3	4200	138.67	0.50	394.281	2.80
Metabasalt	Amphibole	24	33600	272.92	2.05	812.366	23.42
Metabasalt	Chlorite	30	42000	210.90	3.32	650.423	30.33
Metabasalt	Calcite	4	5600	36.93	2.53	100.087	3.55
Serpentinite	Antigorite	97.2	136125	145.76	15.56	378.023	94.60
Serpentinite	Magnetite	2	3875	44.52	1.45	231.539	5.40

As described in Apollaro *et al.* (2011), the rate law based on the transition state theory (TST; Wolery and Jarek, 2003):

$$v_j = f_j \cdot A_{S,j} \cdot \sum_{i=1}^{i_{T+j}} k_{+,ij} \cdot \left(\prod_{n=1}^{n_{T+,ij}} a_n^{-N_{+,ij}} \right) \cdot \left(1 - e^{-\frac{A_{+,j}}{\sigma_{+,ij} RT}} \right) \qquad (8)$$

was selected from the different types of kinetic equations available in the EQ6 code, since it has a strong theoretical foundation and it permits a convenient description of dissolution reactions (and precipitation processes as well, although they are neglected in this work), in spite of some different opinions (e.g., Gin *et al*., 2008).

Eq. (9) takes into consideration a total number $i_{T+,j}$ of mechanisms, each one including a rate constant ($k_{+,ij}$), a kinetic activity product, and a thermodynamic affinity ($A_{+,j}$) term. The kinetic activity product involves the activities of $n_{T+,ij}$ aqueous species, each one raised to a reaction order $-N_{+,ij} \neq 0$. The affinity term involves the universal gas constant, R, the absolute temperature, T, and the so-called average stoichiometric number of Temkin ($\sigma_{+,ij}$), which relates the thermodynamic affinity of the macroscopic reaction ($A_{+,j}$) to that of the corresponding elementary (microscopic) reaction ($A_{+,j}/\sigma_{+,ij}$).

The total surface area of each mineral, $A_{S,j}$ (i.e., the surface of contact between the solid phase and 1 kg of the aqueous solution) also appears in Eq. (8) together with the factor f_j, representing the fraction of reactive to total surface area, which is usually set to 1. The Arrhenius equation:

$$k_{+,ij} = k_{+,ij\,298.15} \cdot \exp\left[\frac{-E_{+,ij}}{R}\left(\frac{1}{T} - \frac{1}{298.15}\right)\right] \tag{9}$$

is used to describe the temperature dependence of rate constants. In Eq. (9), $k_{+,ij,298.15}$ and $E_{+,ij}$ are the rate constant and the activation energy, respectively, of the *i*th dissolution mechanism of the *j*th mineral, at the reference temperature of 298.15 K. To a first approximation, activation energy is assumed to be temperature independent although this assumption is not always justified.

3.1.4 Possible solid products

To model the dissolution of the metabasalt the precipitation of the following solid reactants was allowed: gibbsite, kaolinite, α-cristobalite and hausmannite as well as several solid solutions (see below). Precipitation of talc and magnesite was also permitted, and indeed it occurred, during simulation of serpentinite–water interaction. These minerals were selected based on the general understanding of chemical weathering (e.g., Berner and Berner, 1996; Langmuir, 1997; Appelo and Postma, 1999), to avoid the production of undesired minerals.

According to Apollaro *et al.* (2011), the following solid solutions were allowed to precipitate:

(a) Oxy-hydroxide, made up of ferrihydrite, and Fe(II)-, Cr(III)-, Mn(III)-, Mn(II)-, Ni(II)-, Zn(II)-, Cu(II)- and Co(II)-endmembers.

(b) Trigonal carbonate, including calcite, siderite, rhodochrosite, smithsonite, sphaerocobaltite, Ni-carbonate, Cu-carbonate, and Ca-arsenate.

(c) Orthorhombic carbonate, comprising aragonite, strontianite, witherite, and cerussite.

(d) Smectite, comprising Mg-, Ca-, Na- and K-beidellites, and Mg-, Ca-, Na- and K-montmorillonites.

(e) Saponite, constituted by the Mg-, Ca-, Na- and K endmembers.

Solid solutions were assumed to be ideal, as this is the only solid mixing model supported by the EQ3/6 software package. Further details are given by Marini *et al*. (2001).

The condition of instantaneous equilibrium was assumed for secondary solid phases. Thus, it is admitted that the rate of the whole water–rock interaction process is uniquely fixed by dissolution kinetics, which is a reasonable assumption if the dissolution processes proceed much slower than precipitation reactions (Marini, 2007).

3.1.5 The choice of alkalinity as master variable

To compare results of reaction path modeling with corresponding analytical data, suitable binary correlation plots were prepared using alkalinity as proxy for the reaction progress variable, ξ, which is unknown for groundwater samples. Alkalinity has been preferred to pH since it continuously increases during progressive dissolution of primary minerals, driven by conversion of CO_2(aq) to HCO_3^- ion (Garrels, 1968), unless precipitation of secondary carbonate minerals and/or dissolution of alkalinity-consuming solid phases (e.g., pyrite; Accornero, 2008) take place. In contrast, pH changes during water–rock interaction are quite irregular and less continuous because they are affected by the presence of different buffer systems (e.g., Christenson and Wood, 1993; Reed, 1997; Marini *et al*., 2003). In particular, close-to-linear relations between log alkalinity and log ξ are observed in Fig. 15a, with a good correspondence between the trends for different f_{CO2} values, in the metabasalt case, whereas there are limited differences between the alkalinity–ξ relationships for serpentinite dissolution, with the trends for f_{CO2} of $10^{-2.9}$ and $10^{-2.5}$ bar showing a zigzag part due to precipitation of magnesite and talc, in addition to the

secondary solid phases discussed in §3.4 (Fig. 15c). In contrast, the pH–log ξ paths have distinct starting points which reflect the different imposed f_{CO2} values, and are clearly separated at all ξ values, both in the metabasalt case (Fig. 15b) and in the serpentinite case (Fig. 15d). Again, it is observed a zigzag portion in the pH–ξ curves for f_{CO2} of $10^{-2.9}$ and $10^{-2.5}$ bar as for the alkalinity–ξ curves. Based on these considerations, alkalinity was chosen as reference variable.

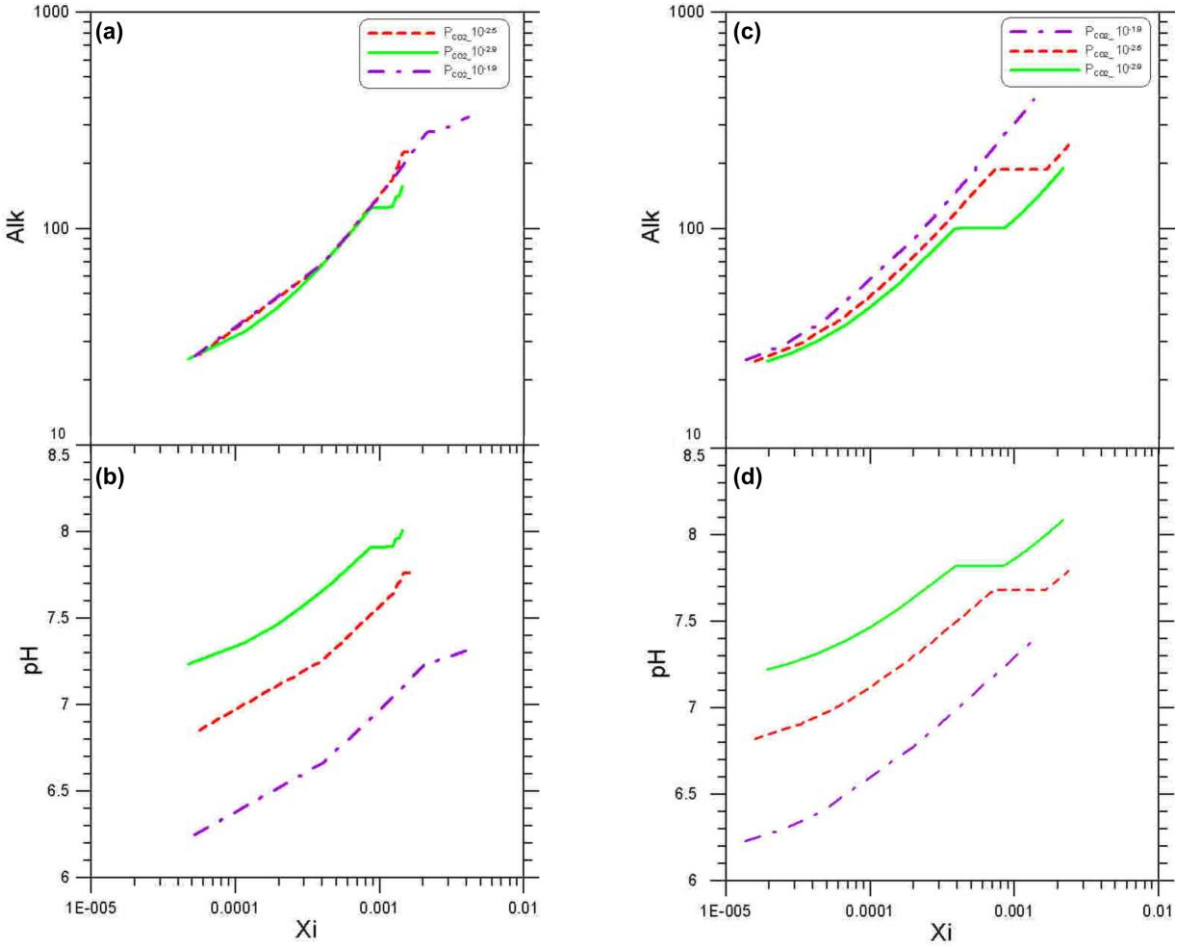

Fig. 15. Log-log plot of alkalinity vs. the reaction progress variable showing the results of reaction path modeling for the dissolution of (a) metabasalts and (c) serpentinites under different f_{CO2} valus (see legend); plot of pH vs. the reaction progress variable (on a log scale) showing the results of reaction path modeling for the dissolution of (b) metabasalts and (d) serpentinites under different f_{CO2} valus (see legend).

3.2 Results of reaction path modeling involving the kinetic parameters measured for separate solid phases (literature data)

In this section, all the runs carried out at a f_{CO2} of $10^{-1.9}$, $10^{-2.5}$ and $10^{-2.9}$ bar are described for both metabasalts and serpentinites.

3.2.1 The primary minerals in metabasalt dissolution

In the early stages of the progressive dissolution of metabasalt, for alkalinity < 165 mg/L at a constant f_{CO2} of $10^{-2.5}$ bar (Fig. 16a) and for alkalinity < 125 mg/L at a constant f_{CO2} of $10^{-2.9}$ bar (Fig. 16c), the water-rock interaction process is dominated by preferential destruction of calcite, whose dissolved mass is larger than those of other primary minerals (amphibole, epidote, albite, chlorite and phengite, in order of decreasing importance) by 4-7 orders of magnitude. The water-rock interaction process changes completely when the aqueous solution attains saturation with respect to calcite, which does not dissolve anymore and remains in the system as an unreactive material. In this late part of the water-rock interaction process, amphibole is the main primary mineral contributing solutes to the aqueous solution, followed by the other solids in the same order recognized for the first part.

The moles of solid reactants destroyed during the metabasalt dissolution at a constant f_{CO2} of $10^{-1.9}$ bar (Fig. 16b) show a different evolution, as the aqueous solution remains always undersaturated with calcite. Consequently, the whole simulation is dominated by dissolution of calcite, accompanied by minor amounts of amphibole, epidote and albite and negligible quantities of chlorite and phengite.

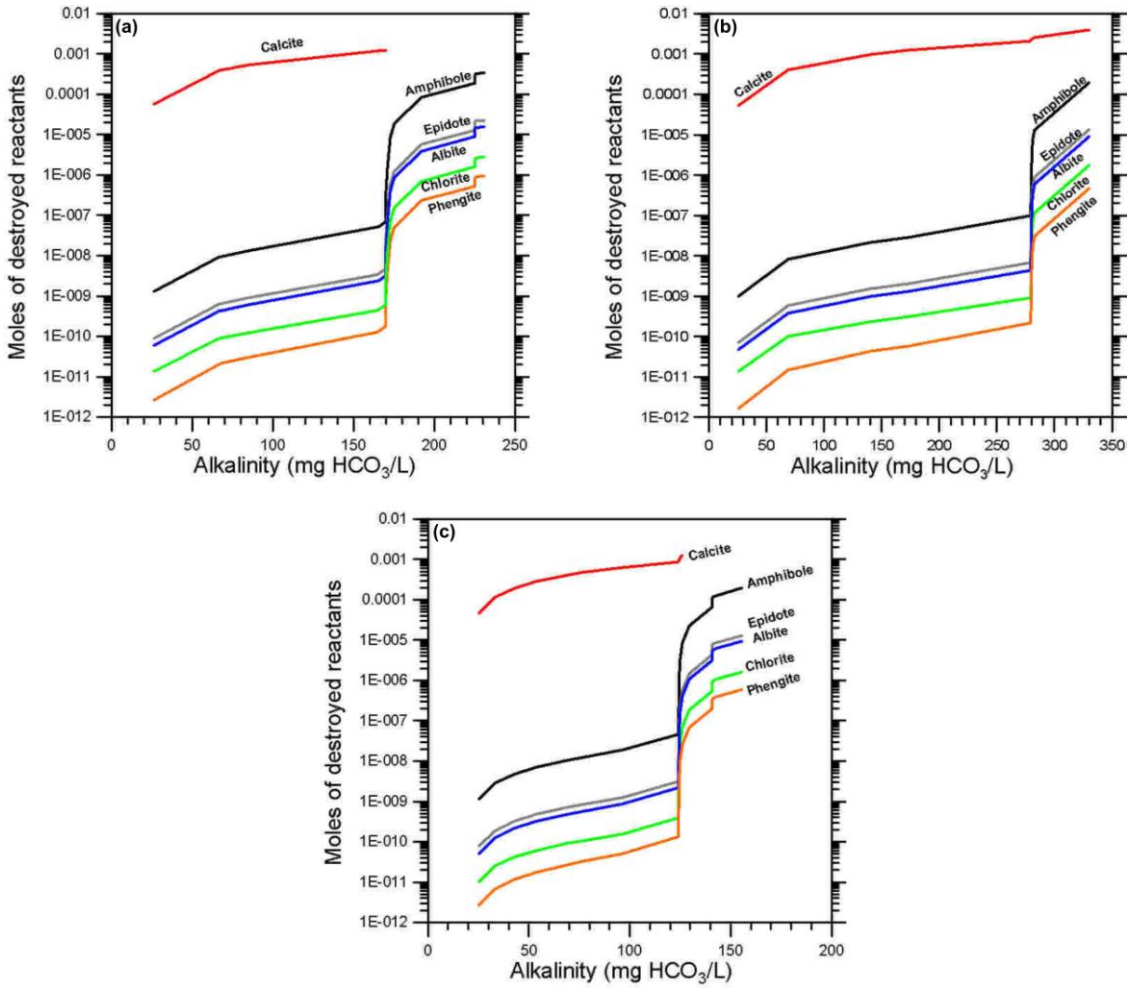

Fig. 16. Moles of destroyed solid reactants against alkalinity, showing the results of reaction path modeling for the dissolution of metabasalt under a f_{CO2} of (a) $10^{-2.5}$ bar, (b) $10^{-1.9}$ bar and (c) $10^{-2.9}$ bar.

3.2.2 The primary minerals in serpentinite dissolution

Dissolution of serpentinite is characterized by the destruction of serpentine and magnetite in nearly similar amounts during the entire simulation at a constant f_{CO2} of $10^{-2.5}$ and $10^{-2.9}$ bar (Figs. 17a-c), whereas the amount of destroyed serpentine prevails on the quantity of dissolved magnetite throughout the reaction path at a constant f_{CO2} of $10^{-1.9}$ bar (Fig. 17b).

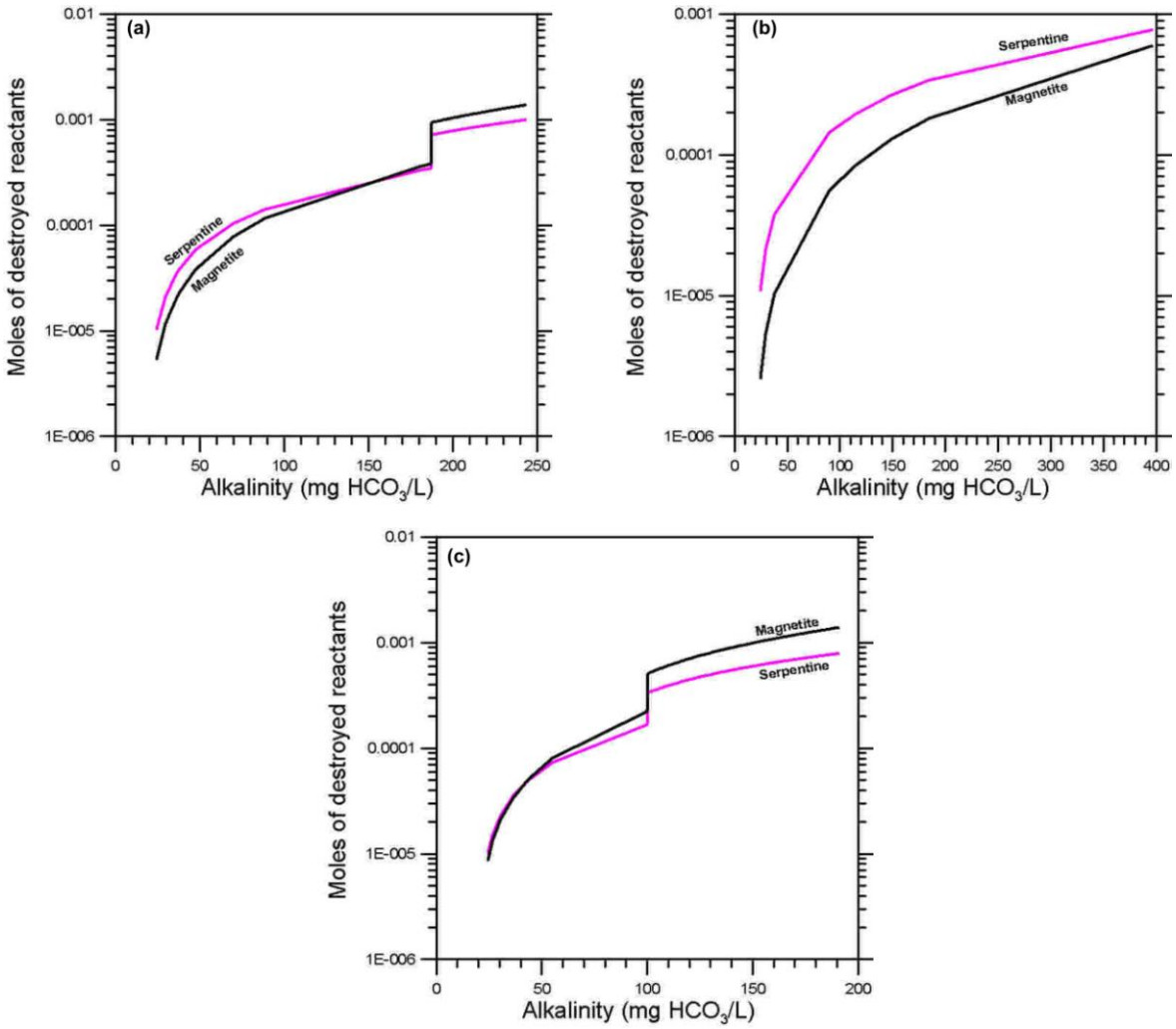

Fig. 17. Moles of destroyed solid reactants against alkalinity, showing the results of reaction path modeling for the dissolution of serpentinites under a f_{CO2} of (a) $10^{-2.5}$ bar, (b) $10^{-1.9}$ bar and (c) $10^{-2.9}$ bar.

3.2.3 The secondary minerals in metabasalt dissolution

The differences in the type, amount, appearance/disappearance along the reaction path of the secondary minerals produced under f_{CO2} of $10^{-2.5}$ bar (Fig. 18a), $10^{-1.9}$ bar (Fig. 18b) and $10^{-2.9}$ bar (Fig. 18c) mainly reflect the different contributions of chemical elements provided by: (i) dissolution of calcite accompanied by very small amounts (practically negligible) of silicate minerals, and (ii) dissolution of tremolite-rich amphibole and subordinately of other silicates when calcite dissolution is hindered by attainment of saturation at f_{CO2} of $10^{-2.5}$ and $10^{-2.9}$ bar. Fig. 18 shows that the amount of kaolinite produced is nearly independent on f_{CO2}, whereas increasing f_{CO2} values lead to increasing persistence of kaolinite. In fact, kaolinite: (i) precipitates early and it is substituted by

smectites before attainment of calcite saturation, at f_{CO2} of $10^{-2.9}$ bar, (ii) whereas it persists during the calcite-dominated dissolution stage at f_{CO2} of $10^{-2.5}$ and $10^{-1.9}$ bars. Furthermore, both kaolinite and hausmannite (which does not precipitate at f_{CO2} of $10^{-1.9}$ bar) disappear, at the beginning of the amphibole-dominated dissolution stage, since the larger availability of Al and Si and the higher pH favor the production of smectites. The amphibole-dominated dissolution stage is characterized by the appearance of several secondary minerals, including α-cristobalite and trigonal carbonates (the two most important product phases, in terms of mass), smectites, and, in the last steps of the simulation, saponites as well. Since saponites are destabilized by low pH values and high f_{CO2}, they form only at the lowest considered f_{CO2} values of $10^{-2.5}$ and $10^{-2.9}$ bar. Orthorhombic carbonates are persistent minerals, but their appearance is progressively delayed with increasing f_{CO2}. Finally, Fe(III)-rich oxy-hydroxides precipitate early and in little quantities and persist throughout the runs.

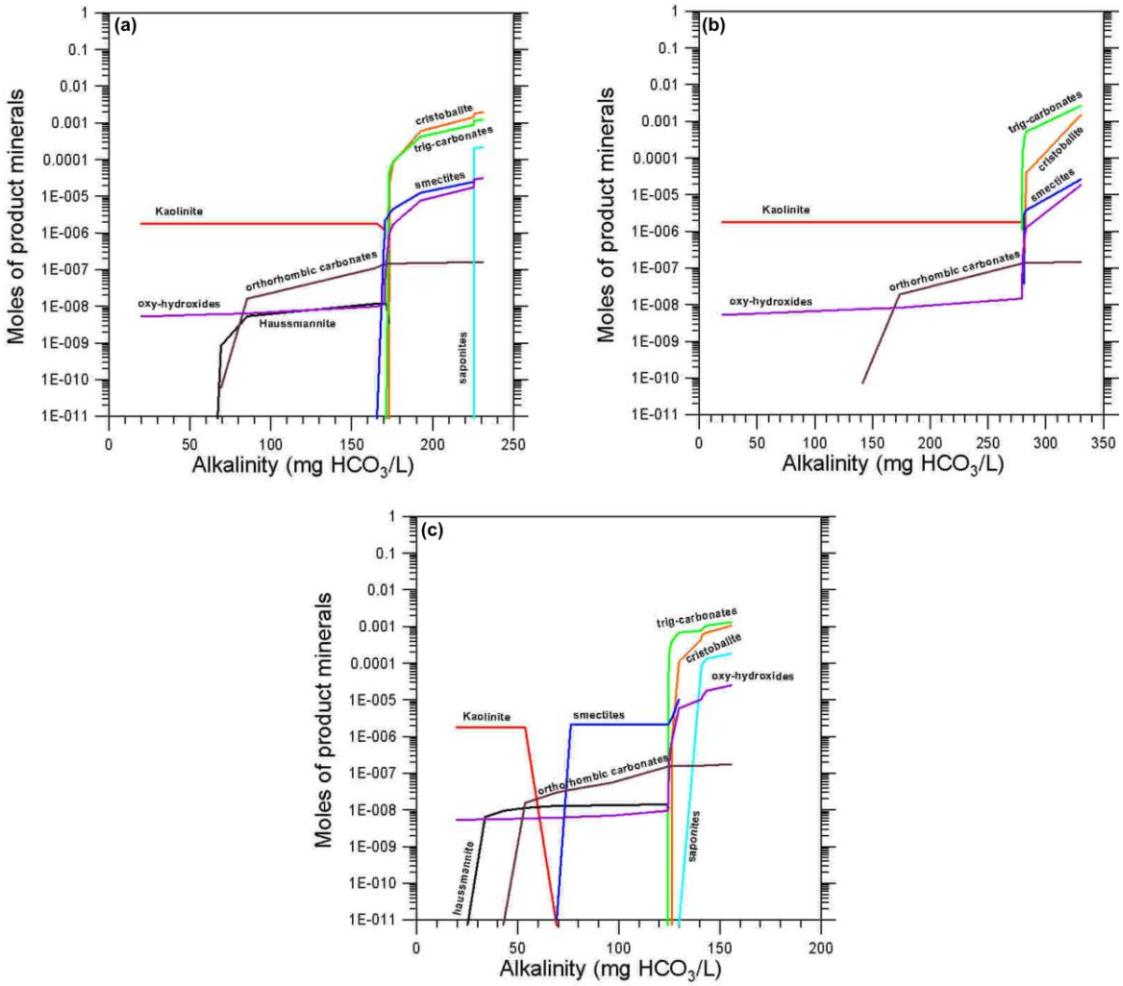

Fig. 18. Moles of solid products phases against alkalinity, showing the results of reaction path modeling for the dissolution of metabasalts under a f_{CO2} of (a) $10^{-2.5}$ bar, (b) $10^{-1.9}$ bar and (c) $10^{-2.9}$ bar.

3.2.4 The secondary minerals in serpentinite dissolution

During serpentinite dissolution the two main solid phases constituting the secondary paragenesis are α-cristobalite and goethite, acting as sinks of Si, mainly released by antigorite dissolution, and Fe, supplied by magnetite destruction, respectively (Fig. 19). Kaolinite is produced in small amounts in the first steps of the simulation and it is quickly substituted by smectites. In the last steps of the simulation, saponites and talc precipitate as well, but they form only at the lowest considered f_{CO2} values of $10^{-2.5}$ and $10^{-2.9}$ bar, as they are destabilized by low pH and high f_{CO2} values. Orthorhombic carbonates are also produced in all the runs but in subordinate amounts.

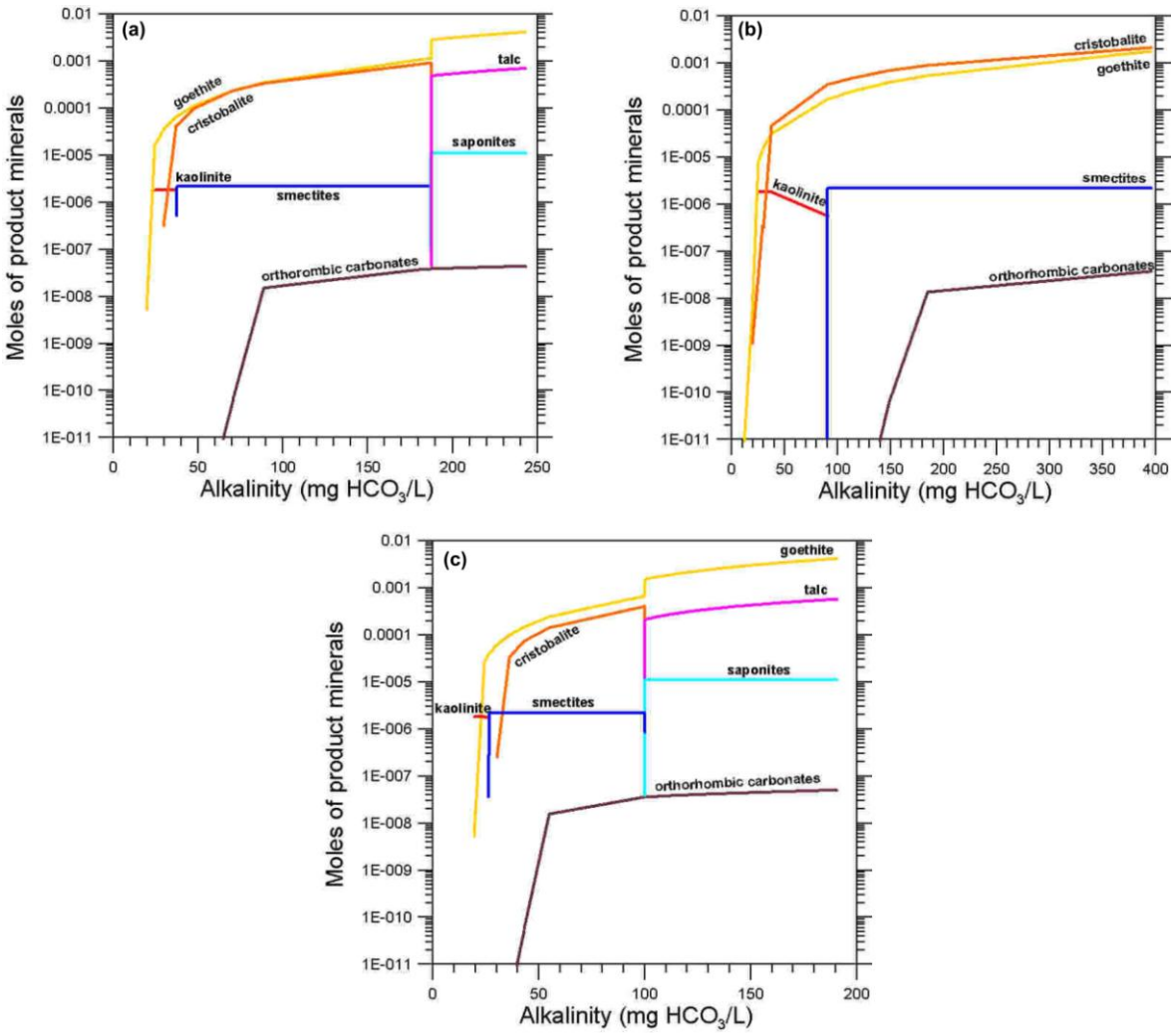

Fig. 19. Moles of solid products phases against alkalinity, showing the results of reaction path modeling for the dissolution of serpentinites under a f_{CO2} of (a) $10^{-2.5}$ bar, (b) $10^{-1.9}$ bar and (c) $10^{-2.9}$ bar.

3.2.5 The aqueous solution

In this section, the theoretical concentrations of calcium and magnesium, the two most important cations provided to the aqueous solution by progressive dissolution of metabasalts and serpentinites, are compared with their analytical counterpart, referring to local shallow groundwaters, through binary correlation diagrams (Figs 20–21), in which alkalinity is reported on the X-axis, as a proxy for the reaction progress variable (see section 3.1.5 for the reasons leading to this choice).

The theoretical paths of metabasalt dissolution, independent of the adopted f_{CO2}, indicate that the concentration of aqueous Ca increases owing to calcite dissolution, as long as the aqueous solution is undersaturated with calcite (Fig. 20a). Maximum dissolved Ca concentration depends on f_{CO2} and reaches values of 89.2, 53.5, and 38.4 mg/L at f_{CO2} of $10^{-1.9}$, $10^{-2.5}$, and $10^{-2.9}$ bar, respectively. In contrast, dissolved Ca content decreases upon attainment of calcite saturation, as the amount of Ca incorporated in precipitating trigonal carbonates is higher than that supplied to the aqueous solution by amphibole and epidote destruction. The computed trend of serpentinite dissolution (Fig. 20b), at any f_{CO2}, is characterized by nearly constant Ca concentration, due to the absence of Ca-bearing mineral in the considered serpentinite. Analytical data for all the Ca–HCO_3 groundwaters are in agreement with the theoretical paths of metabasalt dissolution, whereas the Mg–HCO_3 springs are situated close to the computed trend of serpentinite dissolution.

Dissolved Mg remains constant during the first calcite-dominated stage of metabasalt dissolution, at all f_{CO2} values, since Mg supplied by amphibole, chlorite and phengite destruction is completely insignificant (Fig. 21a). Upon attainment of calcite saturation, dissolution of these silicates, especially the tremolite-rich amphibole, becomes important causing a considerable increase in dissolved Mg, according to relatively steep trends. Dissolution of serpentinite (Fig. 21b) is described by paths of constant slope, somewhat smaller than that of the second stage of metabasalt destruction. In addition, the three paths for different f_{CO2} values are superimposed. Again, analytical data for all the Ca–HCO_3 spring waters are explained by the model results for metabasalt dissolution, whereas the Mg–HCO_3 samples are positioned on the simulated paths of serpentinite dissolution.

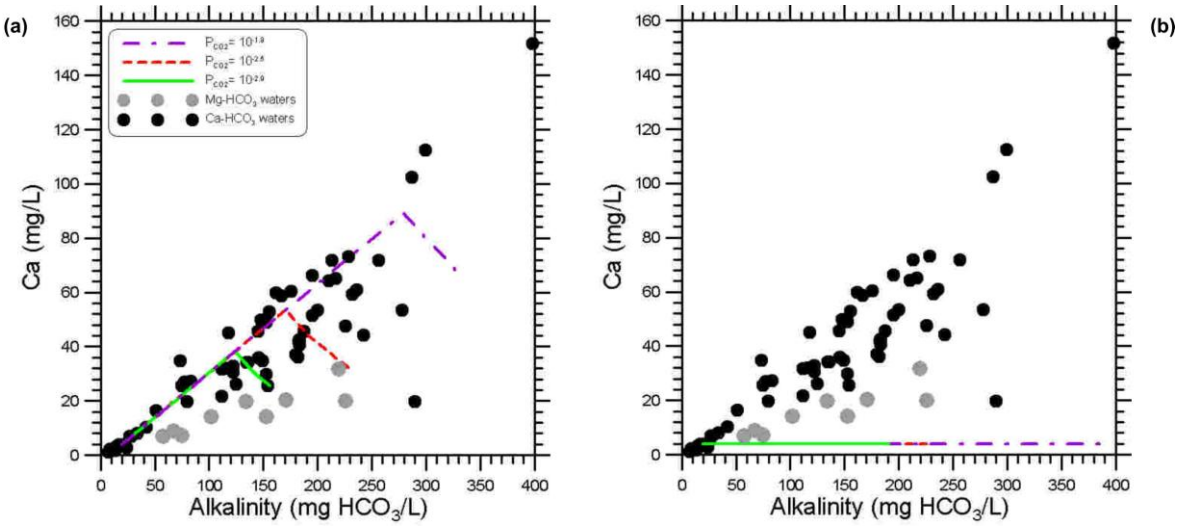

Fig. 20. Plot of Ca vs. alkalinity showing the analytical data (water–rock derived concentrations) for the waters from the study area (closed circles) as well as the results of reaction path modeling for the dissolution of (a) metabasalts and (b) serpentinites under different f_{CO2} values (see legend).

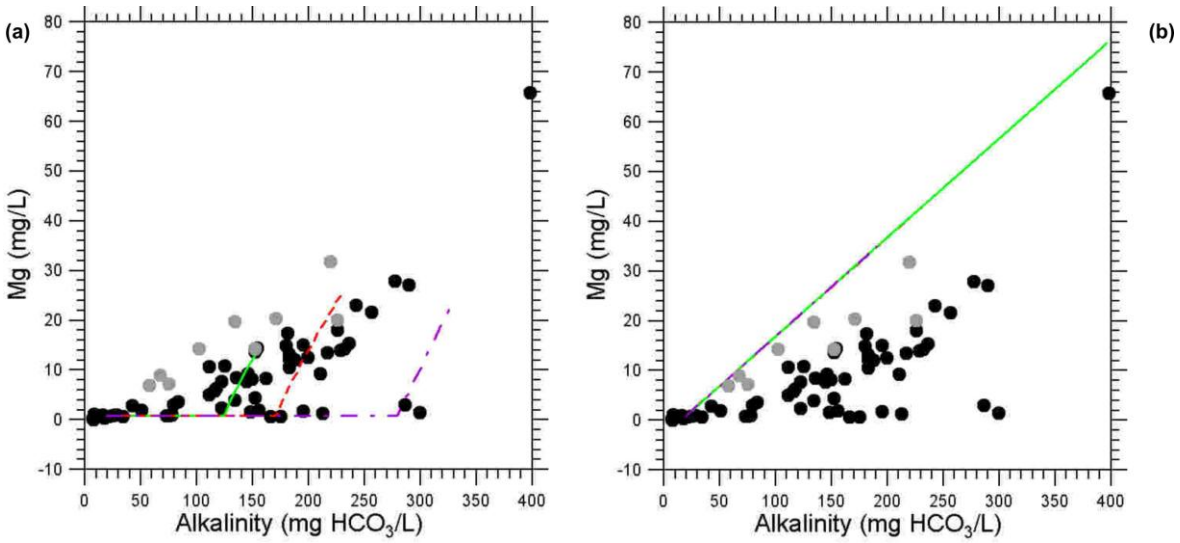

Fig. 21. Plot of Mg vs. alkalinity showing the analytical data (water–rock derived concentrations) for the waters from the study area (closed circles) as well as the results of reaction path modeling for the dissolution of (a) metabasalts and (b) serpentinites under different f_{CO2} values (same legend as for Fig. 20).

3.2.6 Double Solid Reactant Method

Minerals (and solid mixtures) stored in the reference thermodynamic database of the EQ3/6 software package and other similar geochemical codes have ideal or idealized composition, which do not consider the trace elements habitually present in natural minerals. Dissolution of minerals of ideal or idealized composition do not supply trace elements to the aqueous phase. A possible approach to circumvent this problem and to model the release of trace elements from the dissolving solid phases to the aqueous solution is to associate a *special reactant* (which is used to define the trace element content of the dissolving primary solid phase) to a given mineral (or solid mixture) of ideal or idealized composition. This approach is the so-called Double Solid Reactant Method (DSRM), suggested by Accornero and Marini (2008).

Therefore, in the DSRM, each primary solid phase comprises both: (i) an entity whose thermodynamic properties are known, either a pure mineral or a solid mixture and (ii) a *special reactant*, that is a material of known composition and unknown thermodynamic and kinetic properties. Both entities are dissolved with the same rate.

The use of the DSRM approach requires to run each simulation twice (Accornero and Marini, 2008). In the input file of the first run, only pure minerals and solid mixtures (the solid reactants) are introduced, and based on the output file of this first run, the relative rates (mol/mol) for each solid reactant are obtained throughout the reaction path modeling of interest. In the second run, the so-obtained relative rates are assigned to the special reactants associated to each pure mineral or solid mixture by choosing simulation steps small enough so that relative rates of all the solid reactants can be represented by approximately constant values.

In the Double Solid Reactant Method approach, any simulation requires a series of consecutive steps, each of them is referred to a given interval of reaction progress. The input files are based on output files of the previous step, namely the pick-up file of a given step become an input file of the successive step. Parameters, as reaction progress value, are modified in the new input files.

In order to apply this method, a large analytical effort is required to determine the content of the trace elements of interest in all the relevant primary solid phases. To this purpose, the preliminary work described in §2.2 (e.g., LA-ICP-MS analytical data) allowed to constrain the trace elements concentrations of primary solid phases which were used to

define the special reactants associated to the dissolved primary solid phases in the EQ6 input files.

In this study, the DSRM was applied to reproduce the rock-to-water release of trace elements and their fate in the aqueous solution for metabasalts only, due to their overwhelming importance compared to serpentinites as suggested by the chemistry of local groundwaters (see the (Na+K)-Ca-Mg triangular plot and related discussion in §2.1) and confirmed by reaction path modeling results for the two main cationic constituents (see §3.5). A special reactant was defined for each dissolving solid phase (calcite, amphibole, epidote, albite, chlorite and phengite, in order of decreasing importance, see §3.2.1). Although several trace elements (Al, As, Ba, Cd, Co, Cr, Cu, Fe, Mn, Mo, Ni, Pb, Sr, U, V and Zn) were considered in the modeling, only some relevant dissolved constituent are discussed here and represented by means of binary plots (Figs. 22-24).

Chromium and nickel. Concentration of dissolved Cr and Ni (Fig. 22) remain constant at the initial values during the first calcite-dominated stage of metabasalt dissolution, at all f_{CO2} values, owing to the insignificant contributions of silicate minerals as sources of both trace elements. Upon attainment of calcite saturation, dissolution of amphibole dominates, causing the release of relatively large quantities of Cr and somewhat lower amounts of Ni; this process determines significant increments in the contents of both trace elements in the aqueous phase, up to 3 and 1.5 orders of magnitude for Cr and Ni, respectively. As discussed in Apollaro *et al.* (2011), the role of amphibole as Cr-source has rarely been recognized in previous work (e.g., Quantin *et al*., 2008), that generally underscored the importance of other solid phases, comprising chromite, Cr-magnetite, a chromite–silicate mixture, enstatite, augite and chlorite contained in serpentinites (e.g., Robles-Camacho and Armienta, 2000; Becquer *et al*., 2003; Oze, 2003; Oze *et al*., 2004, 2007b). Since dissolved Cr is present in the hexavalent form, no Cr sink is active, apart from its possible reduction driven by organic substances (Böhm and Fischer, 2004), followed by incorporation/sorption of trivalent Cr in ferric oxy-hydroxides. Ni sinks (i.e., the trigonal carbonates and the Fe(III)-rich oxy-hydroxides) incorporate negligible amounts of this element according to the EQ6 simulations. The correspondence between theoretical paths and analytical data is satisfactory for both Cr and Ni, although model data are somewhat higher than the analytical counterpart for Cr (possibly due to reduction and sequestration of

trivalent Cr, which are not taken into account in EQ6 simulations) and vice versa for Ni.

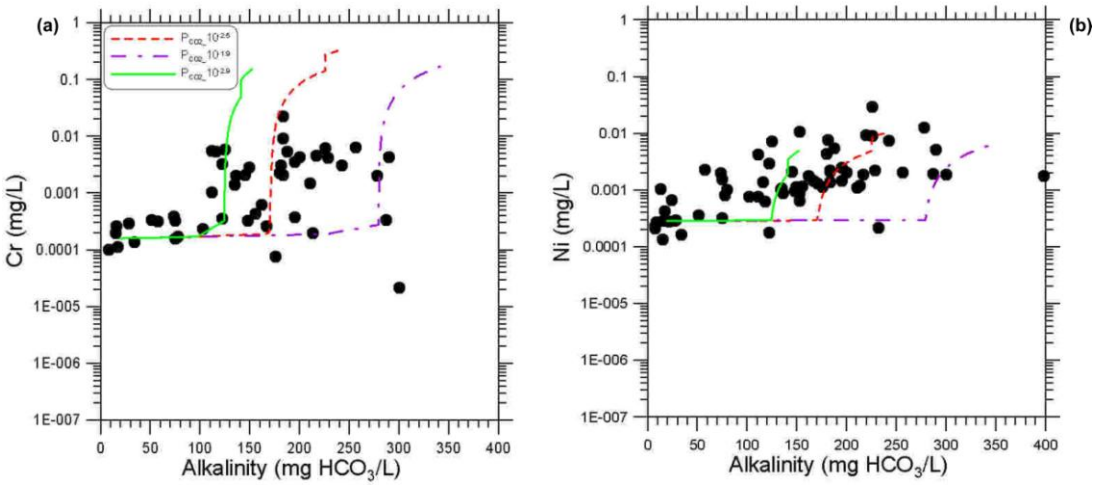

Fig. 22. Plots of (a) Cr and (b) Ni (both on a log scale) vs. alkalinity showing the analytical data (water–rock derived concentrations) for the waters from the study area (closed circles) as well as the results of reaction path modeling for the dissolution of metabasalts under different f_{CO2} values (see legend).

Strontium and lead. Although these two trace elements are incorporated in precipitating orthorhombic carbonates, their proportions are different, with the prevalence of the strontianite component ($SrCO_3$; molar fraction up to 0.27–0.28) over the cerussite component ($PbCO_3$; molar fraction less than 0.01). Also the supplies of these two trace elements by calcite dissolution are very different, as this primary mineral is much richer in Sr (1250–1450 ppm) than in Pb (1–1.7 ppm). Consequently, the modeled reaction paths for these two trace elements are different and dependent upon the balance of sources and sinks (Fig. 23). The concentration of aqueous Sr is largely controlled by dissolution of calcite. In fact, it increases as long as calcite dissolves, whereas it experiences a limited decrease upon attainment of calcite saturation (Fig. 23a). The concentration of aqueous Pb is nearly constant, owing to the limited supply provided by calcite dissolution, until orthorhombic carbonates begin to precipitate (Fig. 23b). A considerable decrease in the contents of this trace element occurs afterwards. The agreement of theoretical paths and analytical data is satisfactory.

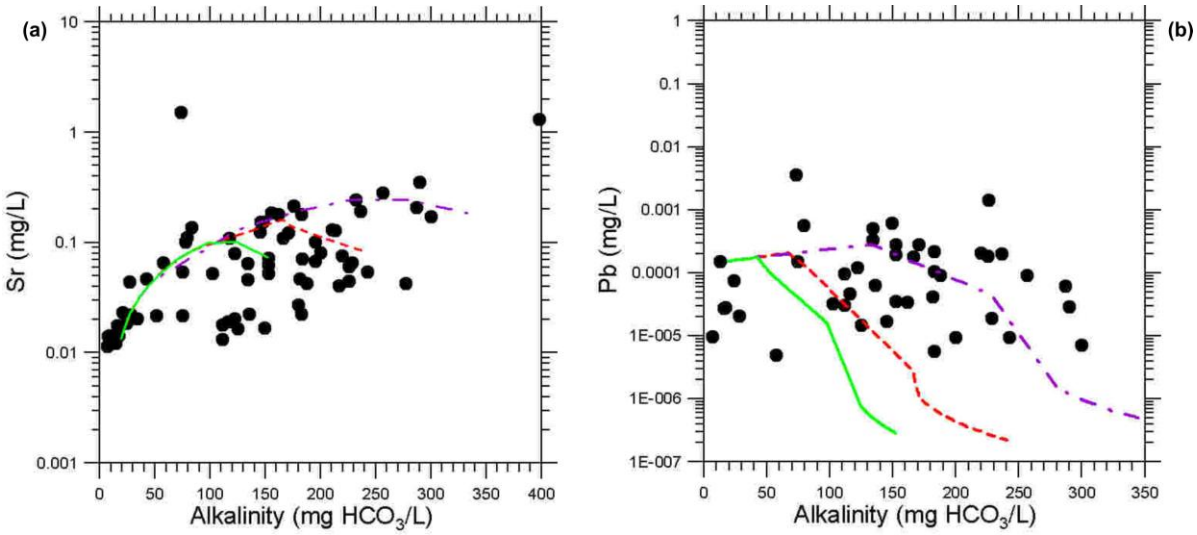

Fig. 23. Plots of (a) Sr and (b) Pb (both on a log scale) vs. alkalinity showing the analytical data (water–rock derived concentrations) for the waters from the study area (closed circles) as well as the results of reaction path modeling for the dissolution of metabasalts under different f_{CO2} values (same legend as for Fig. 22).

Copper and zinc. Again, the main source of these two transition elements is calcite, whereas trigonal carbonates act as their principal sink. The concentrations of both dissolved Cu and Zn exhibit a limited change (Cu) or no change (Zn) as long as the aqueous solution is undersaturated with calcite, whereas a marked decrease in the contents of both solutes takes place as soon as trigonal carbonates begin to precipitate (Fig. 24). The correspondence between model results and analytical data for groundwaters from the study area is very good.

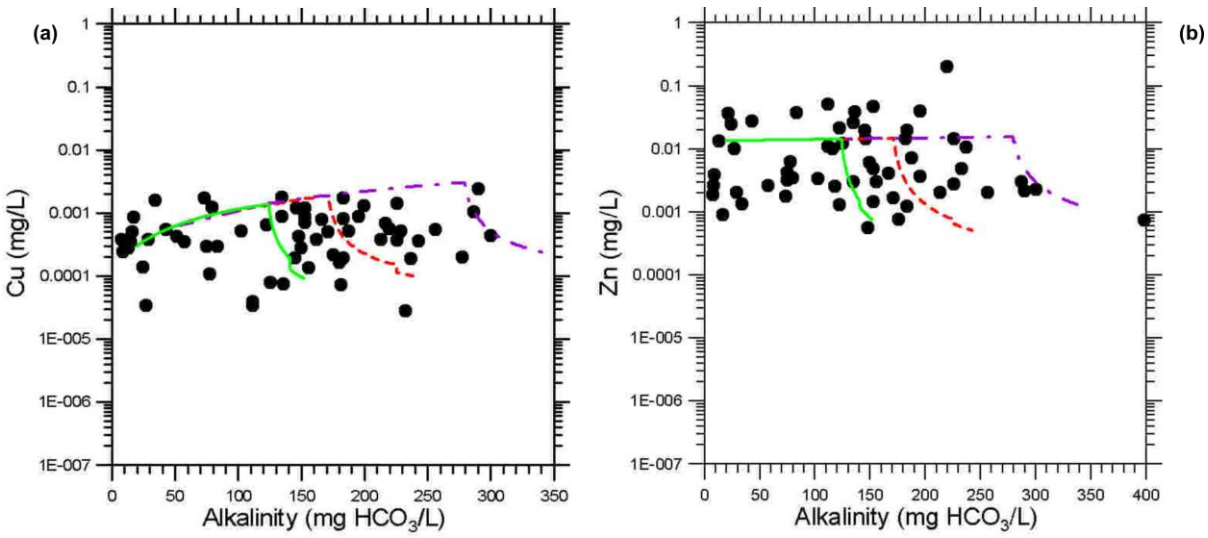

Fig. 24. Plots of (a) Cu and (b) Zn (both on a log scale) vs. alkalinity showing the analytical data (water–rock derived concentrations) for the waters from the study area (closed circles) as well as the results of reaction path modeling for the dissolution of metabasalts under different f_{CO2} values (same legend as for Fig. 22).

3.3 Results of reaction path modeling of metabasalt dissolution involving the whole-rock kinetic parameters measured in this work

The dissolution of the metabasalt sample A19 was modeled using the kinetic parameters retrieved from the results of whole-rock dissolution experiments carried out in this study (see §2.6). Again, simulations were carried out by means of the software package EQ3/6, version 8.0.

The chemical composition of the initial aqueous solution (Table 16), the solid products which are allowed to precipitate during the simulation (§3.1.4), and the boundary conditions are the same of the reaction path modeling exercise involving literature rates. In particular, three runs were performed, under different, constant f_{CO2} values the $10^{-2.9}$, $10^{-2.5}$ and $10^{-1.9}$ bar as in previous geochemical modeling of metabasalt dissolution.

However, the amounts of primary solid phases and their surface areas[3] (Table 18) are different from those of the reaction path modeling exercise involving literature rates, as they refer to the specific sample (A19) which was used in whole-rock dissolution experiments. Therefore, the two reaction path modeling exercises are not comparable. Kinetic parameters introduced in reaction path modeling are reported in Table 14.

Table 18. Geometrical surface areas and masses of solid phases of interest derived from modal abundances (vol.%), based on a geometric model that includes the shape and size of mineral grains and the effective intergranular porosity.

Rock	Mineral	Vol%	Initial surface area (cm^2)	Molar volume (cm^3/mole)	Mass (mole)	MW (g/mole)	Wt%
Metabasalt	Epidote	9	1228323	139.20	1.51	483.223	10.32
Metabasalt	Albite	7	719857	100.25	1.63	262.223	6.05
Metabasalt	Phengite	1	111789	138.67	0.17	394.281	0.94
Metabasalt	Amphibole	50	5851243	272.92	4.27	812.366	49.18
Metabasalt	Chlorite	32	3880067	210.90	3.54	650.423	32.61
Metabasalt	Calcite	1	106540	36.93	0.63	100.087	0.90
Serpentinite	Antigorite	97.2	136125	145.76	15.56	378.023	94.60
Serpentinite	Magnetite	2	3875	44.52	1.45	231.539	5.40

[3] Surface areas of primary solid phases were calculated on the basis of their modal percentages reported in Table 5, following the same approach explained in §3.1.3.

Figure 25 shows the moles of primary solid phases destroyed during the dissolution of the metabasalt sample A19. The first part of the runs carried out at the different and constant f_{CO2} of $10^{-2.5}$ (Fig. 25a) and $10^{-2.9}$ bar (Fig. 25c) is dominated by dissolution of calcite, whose dissolved mass is higher than those of all other solid reactants (chlorite, amphibole, epidote, albite and phengite, in order of decreasing importance) by over five orders of magnitude. Upon attainment of calcite saturation, chlorite becomes the main primary mineral contributing solutes to the aqueous solution, whereas the contribution of other solid phases varies as follows: amphibole > epidote > albite > phengite. In the run carried out at a f_{CO2} of $10^{-1.9}$ (Fig. 25b), the aqueous solution is always undersaturated with calcite, whose dissolution controls all the simulation. Contributions of other primary minerals is subordinate and their relative importance is the same of the other two runs.

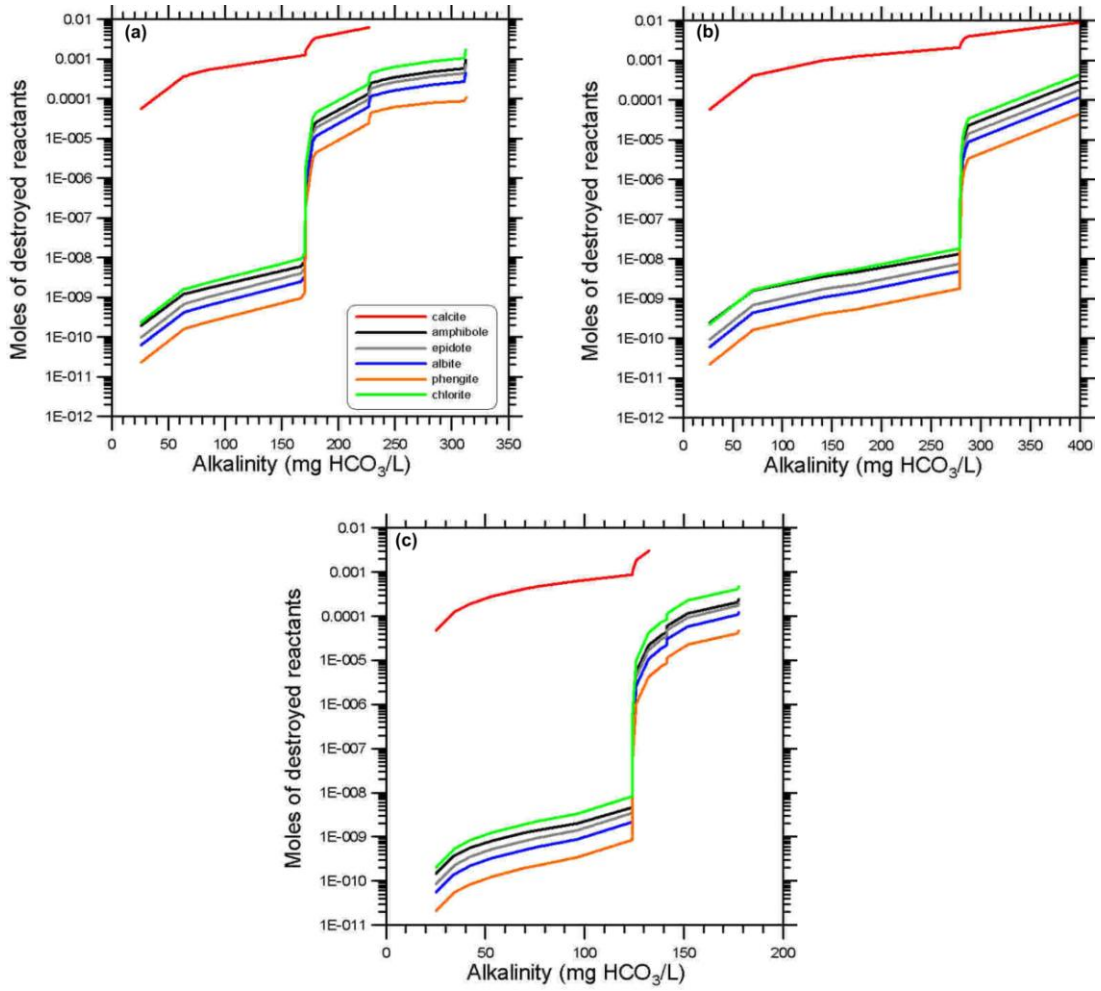

Fig. 25. Moles of destroyed solid reactants against alkalinity, showing the results of reaction path modeling for the dissolution of the metabasalt sample A19, using the whole-rock kinetic parameters specifically measured in this study, under a constant f_{CO2} of (a) $10^{-2.5}$ bar, (b) $10^{-1.9}$ bar and (c) $10^{-2.9}$ bar.

The main secondary minerals produced under f_{CO2} values of $10^{-2.5}$ (Fig. 26a) and $10^{-1.9}$ (Fig. 26b) are kaolinite, at relatively low alkalinity, and trigonal carbonates at relatively high alkalinity. In the run at f_{CO2} of $10^{-2.9}$ bar (Fig. 26c) the main product phases are kaolinite, smectites and trigonal carbonates for increasing alkalinity. Kaolinite is an early-appearing, ephemeral phase and it is substituted by smectites at all the different and constant f_{CO2} of $10^{-2.5}$, $10^{-1.9}$, and $10^{-2.9}$ bar. In particular, at f_{CO2} of $10^{-2.9}$ bar, it disappears at alkalinity of 69 mg/L and it appears again for alkalinity >177 mg/L, near the end of the simulation.

Also hausmannite (which does not precipitate at f_{CO2} of $10^{-1.9}$ bar) disappears once smectites become important. The high-alkalinity part of the runs at f_{CO2} values of $10^{-2.5}$ and $10^{-2.9}$ bar is characterized by the appearance not only of trigonal carbonates (the most important product phase, in terms of mass) and smectites, as already recalled above, but also of saponites, illite-K, and cristobalite (which is produced also at f_{CO2} of $10^{-1.9}$ bar). Orthorhombic carbonates form, in small amounts, at all the considered f_{CO2} values, but their appearance is progressively delayed with increasing f_{CO2}. Finally, Fe(III)-rich oxy-hydroxides precipitate early and persist throughout the runs. Their amounts are small in the first part of the runs but become relatively high in the last stages, due to the increasing Fe supply from amphibole, epidote, and chlorite destruction.

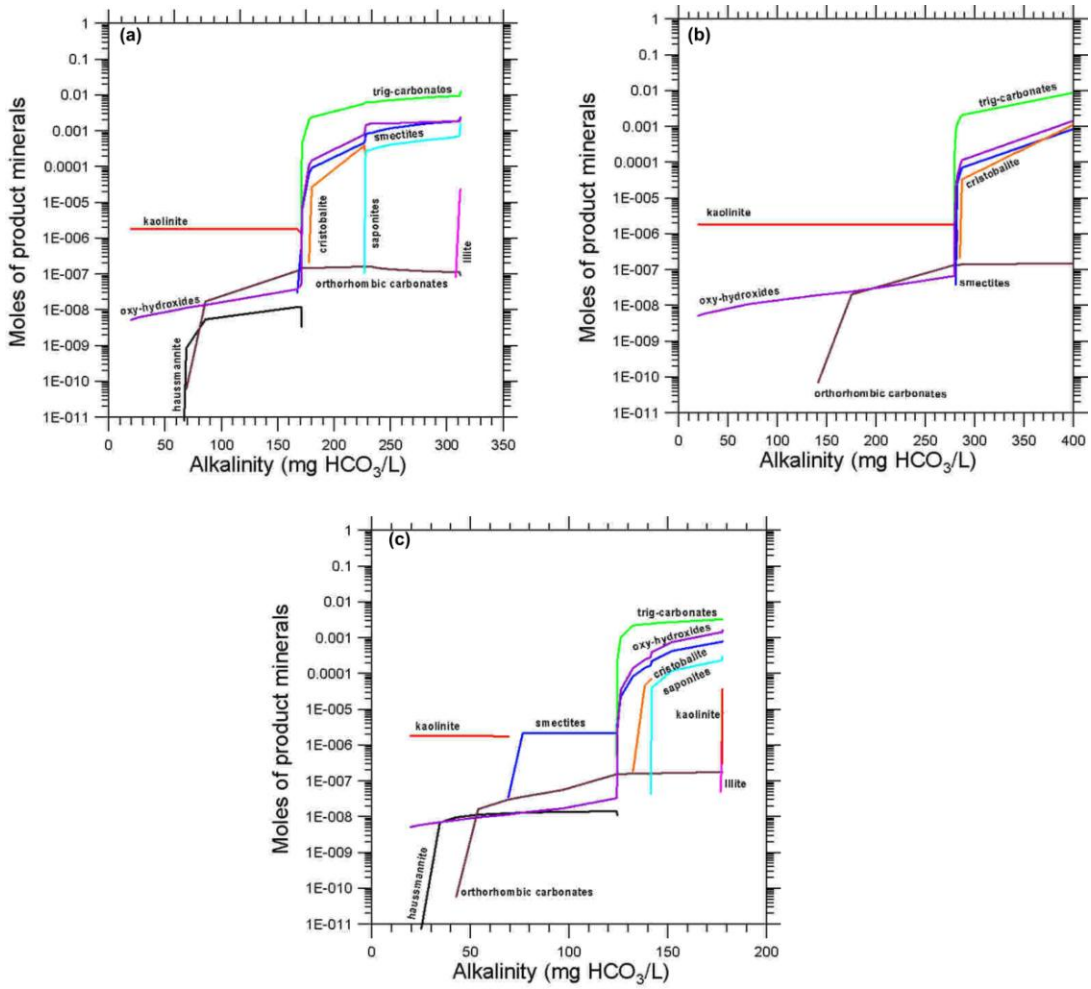

Fig. 26. Moles of solid products phases against alkalinity, showing the results of reaction path modeling for the dissolution of the metabasalt sample A19, using the whole-rock kinetic parameters specifically measured in this study, under a constant f_{CO2} of (a) $10^{-2.5}$ bar, (b) $10^{-1.9}$ bar and (c) $10^{-2.9}$ bar.

Finally, in Fig. 27 it is shown the extent to which the model calculations reproduce the abundance of Ca and Mg in the local groundwaters.

The theoretical paths of metabasalt dissolution (Fig. 27a), independent of the adopted f_{CO2}, indicate that nearly all of the dissolved Ca in the aqueous solution is the result of calcite dissolution, at least up to the maximum concentrations of 89.3, 53.7, and 38.4 mg/L at f_{CO2} of $10^{-1.9}$, $10^{-2.5}$, and $10^{-2.9}$ bar, respectively, corresponding to attainment of calcite saturation. Afterwards, dissolved Ca decreases as the amount of Ca supplied to the system by dissolution of amphibole and epidote is lower than that incorporated in secondary minerals, chiefly trigonal carbonates. Analytical data for all the Ca–HCO_3 groundwaters

are in agreement with the theoretical paths of metabasalt dissolution, whereas the Mg–HCO_3 springs are situated far from these computed trends.

The content of Mg remains constant during the first calcite-dominated stage of metabasalt dissolution, at all f_{CO2} values, since Mg supplied to the system by chlorite, amphibole and phengite destruction is completely insignificant (Fig. 27b). In contrast, in the second part of the simulation, dissolved Mg grows rather steeply with alkalinity, as a consequence of the increasingly importance of silicates dissolution, especially chlorite and amphibole. Again, the correspondence between model results obtained by means of the whole-rock kinetic parameters and analytical data for the Ca-HCO_3 springs from the study area is very good.

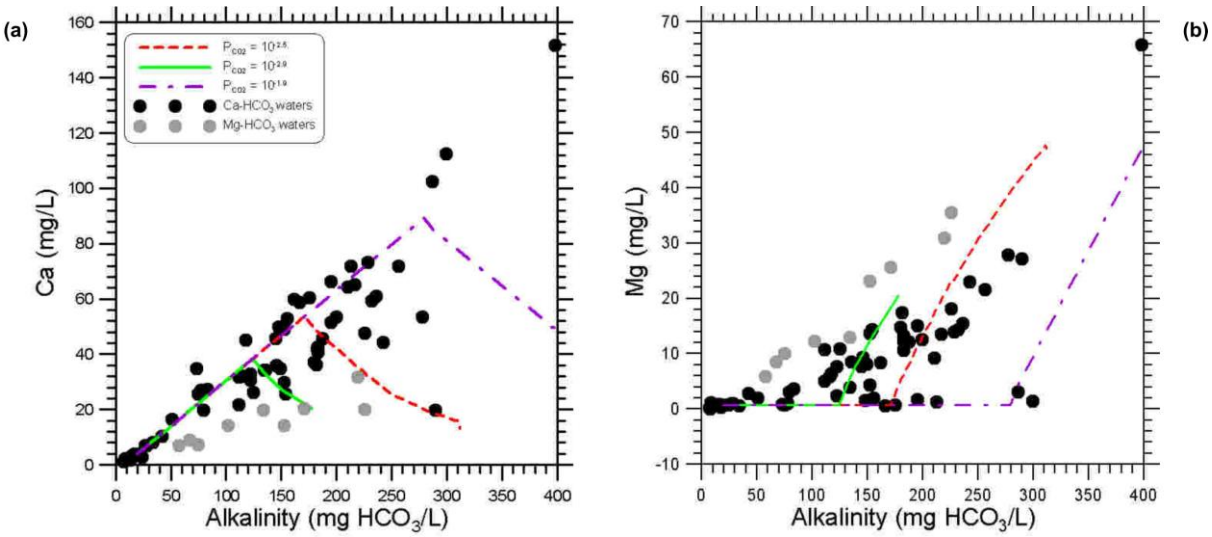

Fig. 27. Plot of (a) Ca and (b) Mg vs. alkalinity showing the analytical data (water–rock derived concentrations) for the waters from the study area (closed circles) as well as the results of reaction path modeling for the dissolution of the metabasalt sample A19, using the whole-rock kinetic parameters measured specifically in this study, under different f_{CO2} values (see legend).

Chapter 4: Conclusions and implications

The ultimate aim of this study is the investigation of the weathering processes of metabasalts and serpentinites of Northern Calabria. To achieve this objective several actions were undertaken, namely:

(i) Field work, comprising collection of rock samples representative of the lithologies of interest as well as of shallow groundwaters interacting with these rock-types.

(ii) Laboratory chemical analyses of groundwaters (IC, ICP-MS) for their classification and the qualitative appraisal of water-rock interaction processes.

(iii) Laboratory chemical and mineralogical analyses of rock samples (optical microscopy, XRD, SEM-EDS, XRF, LA-ICP-MS) for the identification and characterization of rock-forming minerals, comprising their abundance.

(iv) Laboratory experimental determination of whole-rock dissolution rates to retrieve the rates of each constituting mineral phases under these specific conditions (see below for further details).

(v) Geochemical modeling by means of the software package EQ3/6, version 8.0 and the most recent release of its thermodynamic database. In a few words, data acquired on local rocks, minerals, and shallow groundwaters were used to reconstruct the irreversible rock-to-water mass exchanges occurring during weathering of metabasalts and serpentinites of Northern Calabria, by means of reaction path modeling and taking into account the dissolution kinetics of relevant mineral phases. Groundwater analyses were also used to verify the reliability of these "computer experiments". Two different reaction-path-modeling approaches were adopted. In the first approach, kinetic parameters of relevant minerals were taken from the geochemical literature and the progressive dissolution of metabasalts and serpentinites was simulated, also using the Double Solid Reactant Method (DSRM) to investigate the rock-to-water release of trace elements and their fate in the aqueous phase. The second approach relies on kinetic parameters retrieved from whole-rock dissolution experiments of two well characterized rock samples, a metabasalt and a serpentinite.

A significant effort was devoted to determine these whole-rock dissolution rates. In fact, several laboratory experiments in mixed-flow reactors, at 25 °C and different pH values, were carried out by the candidate during the one-year research period profitably spent at both the Lawrence Berkeley National Laboratory (California, USA) and at the Géosciences Environnement Toulouse (Toulouse, France).

To appreciate the innovative nature of this experimental work and contextualize it, it must be recalled that many laboratory studies aimed at the determination of the dissolution rates of separate (single) minerals were carried out so far, especially during the last thirty years, after the pioneering work of Chou and Wollast (1984) on the dissolution rate of albite by mean of a fluidized bed reactor. In contrast, the dissolution rates of individual minerals in multi-mineralic rocks are poorly known as they were investigated in a limited number of works only (e.g., Yokoyama and Banfield, 2002; Evans and Banwart, 2006; Gudbrandsson *et al*., 2011). This lack of information motivated the laboratory experiments which were performed, as part of this thesis, to study the dissolution kinetics of a metabasalt and a serpentinite cropping out in the area of interest in order to retrieve the rates of each constituting mineral phases.

It must be added that, in geochemical modeling, the dissolution rates measured on separate mineral are habitually used to reconstruct the dissolution path of the overall rock, assuming that the dissolution rate measured on a separate mineral is equal to that of the same mineral in a given rock. However, the experimental results of in this study contradict this hypothesis. In fact, it turned out that:

(i) dissolution rates of individual minerals obtained from the dissolution experiments of whole rocks are significantly different from those of separate minerals;

(ii) the dissolution rates of individual minerals exhibit minor differences to each other and appear to be close to the whole-rock rate.

This behavior is probably constrained by the sufficiently abundant mineral(s) of lowest dissolution rate, precluding the dissolution of other faster-dissolving mineral grains as long as these do not come in direct contact with the aqueous solution. This is the main lesson learned from this study, which has remarkable consequences on the understanding of water-rock interaction processes and, in particular, of the rock-to-water release of major constituents and trace elements.

References

Accornero, M., (2008): Geochemical Modeling of Water–Rock Interaction: A Tool to Investigate the Relationships among Different Geo-Environmental Matrices (Bedrock, Soils, Stream Waters and Groundwaters). Application to the Muravera area (Sardinia, Italy).
PhD Thesis. Univ Genoa.

Accornero, M., Marini, L., (2008): The double solid reactant method for modeling the release of trace elements from dissolving solid phases: I. Outline and limitations.
Environ. Geol. **55**, 1627–1635.

Amodio Morelli, L., Bonardi, G., Colonna, V., Dietrich, D., Giunta, G., Ippolito, F., Liguori,V., Lorenzoni, S., Paglionico, A., Perrone, V., Piccaretta, G., Russo, M., Scandone, P., Zanettin-Lorenzoni, E., Zuppetta, A., (1976): L'arco calabro-peloritano nell'orogene appenninico maghrebide.
Mem. Soc. Geol. It. **17**, 1-60.

Apollaro C., Marini L., Critelli T., De Rosa R. (2013a): The standard thermodynamic properties of vermiculites and prediction of their occurrence during water-rock interaction.
Appl. Geochem., **35**, 264-278.

Apollaro C., Marini L., Critelli T., De Rosa R., Bloise A., Miriello D., Catalano M., Armano V. (2013b): Modeling of the impact of dolomite and biotite dissolution on vermiculite composition in a gneissic shallow aquifer of the Sila Massif (Calabria, Italy).
Appl. Geochem., **35**, 297-311.

Apollaro C., Marini L., Critelli T., Barca D., Bloise A., De Rosa R., Liberi F., Miriello D., (2011): Investigation of rock-to-water release and fate of major, minor, and trace elements in the metabasalt-serpentinite shallow aquifer of Mt. Reventino (CZ, Italy) by reaction path modelling.
Appl. Geochem., **26**, 1722–1740.

Apollaro, C., Accornero, M., Marini, L., Barca, D., De Rosa, R., (2009): The impact of dolomite and plagioclase weathering on the chemistry of shallow groundwaters circulating in a granodiorite-dominated catchment of the Sila Massif (Calabria, Southern Italy).
Appl. Geochem. **24**, 957–979.

Appelo, C. A. J., Postma, D., (1999): Geochemistry, Groundwater and Pollution.
A.A. Balkema, Rotterdam.

Arnórsson, S., Andrésdóttir, A., (1995): Processes controlling the distribution of boron and chlorine in natural waters in Iceland.
Geochim. Cosmochim. Acta **59**, 4125–4146.

Bales, R. C. and Morgan, J. J., (1985): Dissolution kinetics of chrysotile at pH 7 to 10.
Geochim. Cosmochim. Acta, **49**, 2281-2288.

Bandstra, J. Z., Buss, H. L., Campen, R. K., Liermann, L. J., Moore, J., Hausrath, E. M., Navarre-Sitchler, A. K., Jang, J. H., Brantley, S. L., (2008): Appendix: compilation of mineral dissolution rates.
In: Brantley, S. L., Kubicki, J. D., White, A. F. (Eds.), Kinetics of Water–Rock Interaction. Springer, pp. 737–823.

Becquer, T., Quantin, C., Sicot, M., Boudot, J. P., (2003): Chromium availability in ultramafic soils from New Caledonia.
Sci. Total Environ. **301**, 251–261.

Berner, E. K., Berner, R. A., (1996): Global Environment: Water, Air, and Geochemical Cycles.
Prentice Hall, Upper Saddle River, New Jersey.

Böhm, B., Fischer, W. R., (2004): Short communication. Kinetics of chromium(III)-oxidation in topsoils.
J. Plant Nutr. Soil Sci. **167**, 22–23.

Boltz, D. F., Mellon, M. G., (1947): Determination of phosphorus, germanium, silicon, and arsenic.

Anal. Chem. **19**, 873–877.

Bruni, J., Canepa, M., Cipolli, F., Marini, L., Ottonello, G., Vetuschi Zuccolini, M., Chiodini, G., Cioni, R., Longinelli, A., (2002): Irreversible water–rock mass transfer accompanying the generation of the neutral, Mg–HCO_3 and high-pH, Ca–OH spring waters of the Genova province, Italy.
Appl. Geochem. **17**, 455–474.

Chen, Y., and Brantley, S. L., (1998): Diopside and anthophyllite dissolution at 25 °C and 90 °C and acid pH.
Chem. Geol., **147**, 233-248.

Chen, Y. and Brantley, S.L. (1997): Temperature- and pH-dependence of albite dissolution rate at acid pH.
Chemical Geology, **135**, 275–292.

Chou, L., and Wollast, R., (1984): Study of the weathering of albite at room temperature and pressure with a fluidized bed reactor.
Geochim. Cosmochim. Acta, **48**, 2205-2217.

Christenson, B.W., Wood, C.P., (1993): Evolution of a vent-hosted hydrothermal system beneath Ruapehu Crater Lake, New Zealand.
Bull. Volcanol. **55**, 547–565.

Cidu, R., Caboi, R., Biddau R., Petrini R., Slejko, F., Flora, O., Stenni, B., Aiuppa, A., Parello, F., Valenza, M., (2008): Caratterizzazione idrogeochimica ed isotopica e valutazione della qualità delle acque superficiali e sotterranee campionate nel Foglio 549 Muravera.
In: Geobasi – (G. Ottonello Ed.), Pacini Ricerca Editore, pp. 149-183.

Cipolli, F., Gambardella, B., Marini, L., Ottonello, G., Vetuschi Zuccolini, M., (2004): Geochemistry of high-pH waters from serpentinites of the Gruppo di Voltri (Genova, Italy) and reaction path modeling of CO_2 sequestration in serpentinite aquifers.
Appl. Geochem. **19**, 787–802.

Daval, D., Hellmann, R., Corvisier, J., Tisserand, D., Martinez, I., Guyot, F., (2010): Dissolution kinetics of diopside as a function of solution saturation state: Macroscopic measurements and implications for modeling of geological storage of CO_2.
Geochim. Cosmochim. Acta **74**, 2615–2633.

Evans, K. A. and Banwart S.A., (2006): Rate controls on the chemical weathering of natural polymineralic material. I. Dissolution behaviour of polymineralic assemblages determined using batch and unsaturated column experiments.
Appl. Geochem., **21**, 352-376.

Faccenna, C., Funiciello, F., Piromallo, C., Rossetti, F., Giardini, D., Funiciello, R., (2004): Subduction and back-arc extension in the Tyrrhenian Sea.
Mem. Descr. Carta Geol. d'It. **44**, 165–184.

Fantoni, D., Brozzo, G., Canepa, M., Cipolli, F., Marini, L., Ottonello, G., Vetuschi Zuccolini, M., (2002): Natural hexavalent chromium in groundwaters interacting with ophiolitic rocks.
Environ.Geol. **42**, 871–882.

Franzini, M., Leoni, L., Saitta, M., (1975): Revisione di una metodologia analitica per la fluorescenza X basata sulla correzione completa degli effetti di matrice.
Rend. Soc. Ital. Miner. Petrol. **21**, 99–108.

Garrels, R. M., (1968): Genesis of some ground waters from igneous rocks.
In: Abelson, P.H. (Ed.), Researches in Geochemistry, vol. 2. Wiley, pp. 406–420.

Gin, S., Jégou, C., Frugier, P., Minet, Y., (2008): Theoretical consideration on the application of the Aagaard–Helgeson rate law to the dissolution of silicate minerals and glasses.
Chem. Geol. **255**, 14–24.

Gudbrandsson, S., Wolff-Boenisch, D., Gislason, S. R., Oelkers, E. H., (2011): An experimental study of crystalline basalt dissolution from $2 \leq pH \leq 11$ and temperatures from 5 to 75 °C.
Geochim. Cosmochim. Acta **75**, 5496–5509.

Hamer M., Graham R. C., Amrhein C., Bozhilov K. N., (2003): Dissolution of ripidolite (Mg, Fe-Chlorite) in organic and inorganic acid solutions.
Soil Sci. Soc. Am. J. **67**, 654–661.

Helgeson, H.C., (1979): Mass transfer among minerals and hydrothermal solutions.
In: *Geochemistry of Hydrothermal Ore Deposits*, H.L. Barnes (ed), 2nd Ed, Wiley. New York, 568-610.

Helgeson, H.C., Delany, J. M., Nesbitt, H. W., Bird, D. K., (1978): Summary and critique of the thermodynamic properties of rock-forming minerals.
Am. J. Sci. **278A**, 1–229.

Helgeson, H. C., Brown, T. H., Nigrini, A., Jones, T. A., (1970): Calculation of mass transfer in geochemical processes involving aqueous solutions.
Geochim. Cosmochim. Acta, **34**, 569-592.

Helgeson H.C., Garrels R.M., Mackenzie F.T. (1969): Evaluation of irreversible reactions in geochemical processes involving minerals and aqueous solutions: II. Applications.
Geochim. Cosmochim. Acta, **33**, 455-481.

Helgeson, H. C., (1968): Evaluation of irreversible reactions in geochemical processes involving minerals and aqueous solutions: I. Thermodynamic relations.
Geochim. Cosmochim. Acta **32**, 853–877.

Hellmann, R., (1994): The albite-water system, Part I. The kinetics of dissolution as a function of pH at 100, 200, and 300 °C.
Geochim. Cosmochim. Acta, **58**, 595-611.

Hey, M. H., (1954): A new review of the chlorites.
Miner. Mag. **30**, 277–292.

Holland T. J. B., Powell R. (1998): An internally consistent thermodynamic data set for phases of petrological interest.

J. Metamorphic Geol., **16**, 309-343.

Iannace, A., Boni, M., Zamparelli, V., (1995): The middle-Upper Triassic of the San Donato Unit Auc. (Northern Calabria): Stratigraphy, paleogeography and tectonic implications.
Rivista Italiana Paleontologia Stratigrafia **101**, 301–24.

Ietto, A., & Barillaro, A., M. (1993): L'unità di San Donato quale margine deformato cretacico-paleogenico del bacino di Lagonegro (Appennino meridionale-Arco-Calabro).
Bollettino della Società Geologica Italiana **111**, 193–215.

Kalinowski, B. E., Faith-Ell, C., Schweda, P., (1998): Dissolution kinetics and alteration of epidote in acidic solutions at 25 °C.
Chem. Geol., **151**, 181-197.

Kalinowski, B. E., Scheda P., (1996): Kinetics of muscovite, phlogopite, and biotite dissolution and alteration at pH 1- 4, room temperature.
G*eochim. Cosmochim. Acta*, **60**, 367-385.

Knauss, K. G., and Kopenhaver, S. A., (1995): The effect of malonate on the dissolution kinetics of albite, quartz, and microcline as a function of pH at 70 °C.
Appl. Geochem., **10**, 17-33.

Knauss, K. G., and Wolery, T. J., (1986): Dependence of albite dissolution kinetics on time at 25 °C and 70 °C.
Geochim. Cosmochim. Acta **50**, 2481–2497.

Knauss, K. G., and Wolery, T. J., (1989): Muscovite dissolution kinetics as a function of pH and time at 70 °C.
Geochim. Cosmochim. Acta **53**, 1493–1501.

Kennedy, V. C., Zellweger, G. W., (1974): Filter pore-size effects on the analysis of Al, Fe, Mn, and Ti in water.
Water Resour. Res. **10**, 785–790.

Kodama, H., and Schnitzer, M., (1973): Dissolution of chlorite minerals by fulvic acid.
Can. J. Soil Sci., **53**, 240-243.

Köppen, W., (1936): Das geographische System der Klimate.
In: Köppen, W., Geiger, R. (Eds.), Handbuch der Klimatologie. Band 5, Teil C. Gebrüder Bornträger, Berlin, pp. 1–46.

Langmuir, D., (1997): Aqueous Environmental Geochemistry.
Prentice Hall, Upper Saddle River, New Jersey.

Laxen, D. P. H., Chandler, I. M., (1982): Comparison of filtration techniques for size distribution in freshwater.
Anal. Chem. **54**, 1350–1355.

Leib, T. M., and Pereira, C. J., (2008): Reactin Kinetics Section 7.
In: Perry's Chemical Engineers' Handbook 8th edition.

Lelli, M., Cioni, R., Marini, L., (2008): The double solid reactant method: II. An application to the shallow groundwaters of the Porto Plain, Vulcano Island (Italy).
Environ. Geol. **56**, 139–158.

Liberi, F., Piluso, E., (2009): Tectonometamorphic evolution of the ophiolites sequences from Northen Calabrian Arc.
Ital. J. Geosci. (Boll. Soc. Geol. It.), Vol. 128, N° 2, pp. 483-493.

Liberi, F., Morten, L., Piluso, E., (2006): Geodynamic significance of ophiolite within the Calabrian Arc.
Island Arc **15**, 26–43.

Lin, F. C., and Clemency, C. V., (1981): Dissolution kinetics of phlogopite. I. Closed system.
Clays Clay Mineral. **29**, 101-106.

Lowson, R. T., Brown, P. L., Comarmond, M.-C. J., Rajaratnam, G., (2007): The kinetics of chlorite dissolution.
Geochim. Cosmochim. Acta **71**, 1431–1447.

Lowson, R. T., Brown, P. L., Comarmond, M.- C. J., Rajaratnam, G., (2005): The kinetics of the dissolution of chlorite as a function of pH and at 25 °C.
Geochim. Cosmochim. Acta **69**, 1687–1699.

Luce, R. W., Bartlett, R. W., Parks, G. A., (1972): Dissolution kinetics of magnesium silicates.
Geochim. Cosmochim. Acta, **36**, 35-50.

Malmström, M., Banwart, S., Lewenhagen, J., Duro, L., Bruno, J., (1996): The dissolution of biotite and chlorite at 25 °C in the near-neutral pH region.
J. Contam. Hydrol., **21**, 201-213.

Marini, L., (2007): Geological Sequestration of Carbon Dioxide: Thermodynamics, Kinetics, and Reaction Path Modeling.
Developments in Geochemistry, vol. 11. Elsevier.

Marini, L., Vetuschi Zuccolini, M., Saldi, G., (2003): The bimodal pH distribution of volcanic lake waters.
J. *Volcanol. Geotherm. Res*. **121**, 83–98.

Marini, L., Canepa, M., Cipolli, F., Ottonello, G., Vetuschi Zuccolini, M., (2001): Use of stream sediment chemistry to predict trace element chemistry of groundwater. A case study from the Bisagno valley (Genoa, Italy).
J. Hydrol. **241**, 194–220.

Marini, L., Ottonello, G., Canepa, M., Cipolli, F., (2000): Water–rock interaction in the Bisagno Valley (Genoa, Italy): application of an inverse approach to model spring water chemistry.
Geochim. Cosmochim. Acta **64**, 2617–2635.

Marini L., Ottonello G., (1997): Atlante degli acquiferi del Comune di Genova. Volume I: Alta Val Bisagno ed Alta Val Polcevera.
Pacini Editore, Pisa, 42 pp. (52 tav.).

Mast, M. A., and Drever, J. I., (1987): The effect of oxalate on the dissolution rates of

oligoclase and tremolite.
Geochim. Cosmochim. Acta, **51**, 2559-2568.

Nickel, E., (1973): Experimental dissolution of light and heavy minerals in comparison with weathering and intrastratal solution.
Contributions to Sedimentology,1, Stability of heavy minerals, 3–68.

Nordstrom, D. K., (1977): Thermochemical redox equilibria of ZoBell's solution.
Geochim. Cosmochim. Acta **41**, 1835–1841.

Oelkers, E. H., Schott, J., Gauthier, J.-M., Herrero-Roncal, T., (2008): An experimental study of the dissolution mechanism and rates of muscovite.
Geochim.Cosmochim. Acta **72**, 4948–4961.

Ogniben, L., (1973): Schema geologico della Calabria in base ai dati odierni.
Geologica Romana **12**, 243–585.

Orlando, A., Borrini, D., Marini, L., (2011): Dissolution and carbonation of a serpentinite: inferences from acid attack and high P-T experiments performed in aqueous solutions at variable salinity.
Appl. Geochem. **26**, 1569-1583.

Oze, C., Bird, D. K., Fendorf, S., (2007b): Genesis of hexavalent chromium from natural sources in soil and groundwater.
PNAS 104, 6544–6549.

Oze, C., Fendorf, S., Bird, D. K., Coleman, R. G., (2004): Chromium geochemistry in serpentinized ultramafic rocks and serpentine soils from the Franciscan Complex of California.
Am. J. Sci. **304**, 67–101.

Oze, C. J.- P., (2003): Chromium Geochemistry of Sepentinites and Serpentine soils.
Thesis in Geological and Environmental Sciences. Standford Univ.

Palandri, James L., Kharaka, Yousif K., (2004): A compilation of rate parameters of water- mineral interaction kinetics for application to geochemical modeling.

US Geol. Surv. Open File Rep. 2004-1068.

Perrone, V., (1996): Une nouvelle hypothése sur la position paléogéographique et l'évolution tétonique des Unités de Verbicaro et de San Donato (région Calabro-Lucanienne; Italie): implications sur le limite Alpes-Appennines en Calabre. C. R. Acad. Sci. Paris, 332, 877-884.

Piluso, E., Cirrincione, R., Morten, L., (2000): Ophiolites of the Calabrian Peloritan Arc and their relationships with the crystalline basement (Catena Costiera and Sila Piccola, Calabria, Southern Italy). *Ofioliti*, **25** (2), 117-140.

Pokrovsky, O. S., and Schott, J., (2000): Kinetics and mechanism of forsterite dissolution at 25 °C and pH 1 to 12. *Geochim. Cosmochim. Acta* **64**, 3313–3325.

Pokrovsky, O. S., and Schott, J., (2004): Experimental study of brucite dissolution and precipitation in aqueous solutions: Surface speciation and chemical affinity control. *Geochim. Cosmochim. Acta*, **68**, 31-45.

Quantin, C., Ettler, V., Garnier, J., Šebek, O., (2008): Sources and extractibility of chromium and nickel in soil profiles developed on Czech serpentinites. C. R. *Geosci. Surf. Geosci. (Pedology)* **340**, 872–882.

Reed, M. H., (1997): Hydrothermal alteration and its relationships to ore fluids composition. In: Barnes, H.L. (Ed.), Geochemistry of Hydrothermal Ore Deposits, third ed. Wiley, pp. 303–365.

Rizzo, V., & Bozzo, C., (1998): Problematiche di Geologia applicata nella realizzazione della galleria ferroviaria Paola-Cosenza. GEAM, Geoingegneria Ambientale Mineraria, Quaderni di Studi e documentazione, Anno XXXV, 1, 3-18.

Robie, R. A., Hemingway, B. S., (1995): Thermodynamic Properties of Minerals and

Related Substances at 298.15 K and 1 bar (10^5 pascals) Pressure and at Higher Temperatures.
U.S. Geol. Surv. Bull. 2131.

Robles-Camacho, J., Armienta, M. A., (2000): Natural chromium contamination of groundwater at Leon Valley, Mexico.
J. Geochem. Explor. **68**, 167–181.

Rose, N. M., (1991): Dissolution rates of prehnite, epidote, and albite.
Geochim. Cosmochim. Acta, **55**, 3273-3286

Ross, G. J., (1967): Kinetics of acid dissolution of an orthochlorite mineral.
Can. J. Chem., **45**, 3031-3034.

Schott, J., Pokrovsky, O. S., Oelkers, E. H., (2009): The link between mineral dissolution/ precipitation kinetics and solution chemistry.
Rev. Mineral. Geochem. **70**, 207-258.

Schott, J., Berner, R. A., and Sjoberg, E. L., (1981): Mechanism of pyroxene and amphibole weathering- I. Experimental studies of iron-free minerals.
Geochim. Cosmochim. Acta, **45,** 2123–2135.

Stefánsson, A., Gíslason, S. R., (2001): Chemical weathering of basalts, SW Iceland. Effect of rock crystallinity, weathering minerals and vegetative cover on chemical fluxes to the ocean.
Am. J. Sci. **301**, 513–556.

Stillings, L. L., and Brantley, S. L., (1995): Feldspar dissolution at 25°C and pH 3: Reaction stoichiometry and the effect of cations.
Geochim. Cosmochim. Acta, **59**, 1483- 1496.

White, A. F., and Brantley, S. L., Eds. (1995): Chemical weathering rates of silicate minerals, vol. 31.
Mineralogical Society of America Reviews in Mineralogy, Washington, D.C.

Wolery T.W., Jove-Colon C., (2007): Qualification of thermodynamic data for

geochemical modeling of mineral-water interactions in dilute systems.
Sandia National Laboratories Report ANL-WIS-GS-000003 REV 01.

Wolery, T. W., Jarek, R. L., (2003): Software User's Manual. EQ3/6, Version 8.0.
Sandia National Laboratories, US Dept. of Energy Report.

Wolery, T. J., Daveler, S. A., (1992): EQ6, a computer program for reaction path modeling of aqueous geochemical systems: theoretical manual, user's guide and related documentation (version 7.0).
Report UCRl-MA-110662 PT IV. Lawrence Livermore National Laboratory, Livermore, California.

Wolery, T. J., (1992): EQ3NR, A computer program for geochemical aqueous speciation-solubility calculations: Theoretical manual, user's guide and related documentation (version 7.0).
Report UCRL-MA-110662 PT III. Lawrence Livermore National Laboratory, Livermore.

Wolery, T. J., (1979): Calculation of chemical equilibrium between aqueous solutions and minerals: the EQ3/6 software package.
Report UCRL-52658, Lawrence Livermore National Laboratory, Livermore.

Wolery, T. J., (1978): Some Chemical Aspects of Hydrothermal Processes at Mid-Oceanic Ridges - A theoretical Study. I. Basalt-Sea Water Reaction and Chemical Cycling between the Oceanic Crust and the Oceans. II. Calculation of Chemical Equilibrium between Aqueous Solutions and Minerals.
Unpub. P.h.D. Diss., Northwestern Univ., Evaston, IL.

Yokoyama, T., and Banfield, J. F., (2002): Direct determinations of the rates of rhyolite dissolution and clay formation over 52,000 years and comparison with laboratory measurements.
Geochim. Cosmochim. Acta, **66**, 2665- 2681.

Acknowledgement

My doctoral thesis would not have come to a completion if I did not have the help and support of a number of people. I would like to express my sincere gratitude to all of them.

Above all, I would like to thank my parents, my sister and my brother who encouraged and help me at every stage of my personal and academic step and my boyfriend, for his great patience at all times and for supporting me in every possible way.

I am extremely grateful to Professor Luigi Marini for his valuable guidance and for his support that allowed me to grow and extend my skills in aqueous geochemistry.

I also extend my gratitude to my supervisor Carmine for his help, for accepting me as his P.h.D. student and for believing in me and Professor Rosanna De Rosa for her academic support provided to carry out this research work and for being present every time there was a problem to solve.

I thank Dr. Jacques Schott and Dr. Eric Oelkers who have been my supervisors during the six months I spent in Toulouse. It was a great opportunity for me to spend this period under their guidance and to have the privilege to learn from their research expertise.

I acknowledge the support of Thomas and Damien who have been my informal supervisor during the period I spent in Toulouse and in Berkeley who encouraged and helped me to think more independently about my experiments and results. They became two good friends who supported me during the difficult times.

I want to thank Vasileios for his immense help, his precious comments, his constructive criticism, for challenging me to become a better student and for his contagious enthusiasm and love for experimental geochemistry.

I also thank Aridane for many discussions and suggestions, Nik for his encouragement and kindness and Andrea and Olivier, for their happiness and sense of humor and for taking care of my experiments when it was necessary.

A special thank to Manuela, a colleague and a friend with whom I shared most of the enjoyable days of these three years.

I would like to thank Andrea Bloise, for the interest he showed for my research and for having a good word in the worst moment; Roberta, a colleague and my officemate for the long conversations we had during our P.h.D. and Salvatore and Giovanni for their help during the sampling and the analytical measurements.

Last, but by no means least, I thank all of those people who provided technical support and assistance and the “aqueous geochemistry”, a world to discover and a passion to follow.

La presente tesi è cofinanziata con il sostegno della Commissione Europea, Fondo Sociale Europeo e della Regione Calabria. L'autore è il solo responsabile di questa tesi e la Commissione Europea e la Regione Calabria declinano ogni responsabilità sull'uso che potrà essere fatto delle informazioni in essa contenute.